IMPROVEMENT AND USE OF RADIATIVE TRANSFER MODELS TO ASSESS LUNAR SPACE WEATHERING AND MECHANISMS FOR SWIRL FORMATION

Dawei Liu

Submitted to the faculty of the University Graduate School
in partial fulfillment of the requirements
for the degree
Doctor of Philosophy
in the Department of Earth Sciences,
Indiana University

August 2015

Accepted by the Graduate Faculty, Indiana University, in partial fulfillment of the requirements for the degree of Doctor of Philosophy.

Lin Li Ph.D., Chair

Pierre-André Jacinthe Ph.D.

Doctoral Committee

Lixin Wang Ph.D.

June 15, 2015

Ruihua Cheng Ph.D.

Daniel Johnson Ph.D.

ACKNOWLEDGEMENTS

Many people contributed to my research which led directly to this thesis. I have benefited from their support, guidance and encouragement. I would like to thank my advisor Lin Li for his unconditional support and contagious enthusiasm. It is difficult to state how grateful I am that he provided me the opportunity to be involved in the world of lunar geology research. He is the most patient and kindest people I have known, someone who always strikes the balance between guiding me and allowing me the freedom to pursue my interest. I am very lucky to have worked with him in the last five years, and I will always be proud to have been his student. I hope maybe one day I can measure up to at least his example if not his status as a scientist.

A special thank goes to all my committee members, Lixin Wang, Pierre-André Jacinthe, Ruihua Cheng, and Daniel Johnson. I am grateful for their professional guidance and suggestions on my thesis. I simply cannot request a better and sensible group of scientific evaluators.

On the particular side, I have to thank all the faculty members and fellow graduate students in the department of earth sciences for their assistance and friendship during varying stages of my academic training. Thanks also to Lisa L. McVicker, Cathy Chouinard and other staff members in our department, and Debra Barker of the graduate office for their patience, technical and administrative support.

I especially want to say thanks to Jia Du, Kaishan Song and Ying Sun, who spent countless hours with me going over early drafts of my papers, and whose constant support and encouragement have been a real source of strength over the years.

Finally, I must express my love and appreciation to my parents. I cannot thank them enough for everything they have given to me! Thank you for raising me and always standing behind me, believing in me. It is your support and encouragement that push me forward towards the “finish line”.

Dawei Liu

IMPROVEMENT AND USE OF RADIATIVE TRANSFER MODELS TO ASSESS LUNAR SPACE WEATHERING AND MECHANISMS FOR SWIRL FORMATION

This dissertation focuses on quantification of submicroscopic iron of different sizes, mineral abundance and grain size of lunar soils using Hapke's radiative transfer model. The main objective is to explore implications of these results for assessing the relative importance of solar wind implantation versus micrometeorite impacts for lunar space weathering as well as three hypotheses (solar wind deflection, comet impact and dust transport) for swirl formation on the Moon. Results from this study can help to make connections between ordinary chondritic meteorites and asteroids, and put physical and chemical constraints on heating processes in the early solar system.

Lin Li Ph.D., Chair

Table of Contents

CHAPTER 1

INTRODUCTION

1. General Overview

Space weathering is referred to as any alteration process acting on an airless planetary body that greatly changes the physical and chemical properties of its surface materials (*Pieters et al*., 1993; *Chapman*, 2004). It is mainly induced by the implantation of solar wind ions and the bombardment of meteoroids/micrometeoroids, and has been widely observed on the Moon, Mercury and asteroids (*Hapke*, 1965; *Hapke et al*., 1970; *Nobel and Pieters*, 2003; *Brunetto et al*., 2006). Space weathering also alters the optical properties of planetary surface materials and impedes our ability to remotely assess the mineralogy and composition of a planetary surface (*Pieters et al*., 1993, 2000). A deep insight into the space weathering process is central to improving the accuracy of mineral abundance estimation via remote-sensing techniques (*Chapman*, 1996; *Hapke*, 2001). Broadly, understanding the optical effect of space weathering and inherent mechanisms for space weathering allows us to establish connections between the ordinary chondritic meteorites and asteroids, which is of fundamental importance in putting constraint on heating processes in the early solar system (*Adam and McCord*, 1971; *Chapman*, 1996, 2004; *Marchi et al*., 2006). Moreover, investigation of space weathering can provide insight into the interaction of solar wind ions with surface materials of a planet, which can aid in understanding the origin and distribution of OH^-/H_2O on a planetary surface (*Garrick-Bethell et al*., 2015; *Pieters and Garrick-Bethell*, 2015).

The Moon provides us with a unique opportunity to study space weathering because it is the only airless planetary body with returned samples. Ever since the lunar surface samples returned from the Apollo missions, it was immediately apparent that the optical properties of lunar soils are quite different from those of lunar rocks pulverized in the

laboratory (*McCord and Johnson*, 1970; *McCord and Adams*, 1973; *Pieters et al*., 2000). Compared with the spectra of pulverized lunar rocks, the spectra of lunar soils show an overall reduction of reflectance, attenuated absorption band strength and red-sloped continuum (Fig. 1-1) (*Fischer and Pieters*, 1994). Subsequent studies have revealed that these spectral characteristics of lunar soils result from the formation of a layer of fine-grained submicroscopic iron (SMFe) coating on the surface of soil grains after a long time exposure of fresh lunar soils to space environment (*Keller and Mckay*, 1993, 1997; *Taylor et al*., 2001, 2010). Two mechanisms have been invoked to explain the generation of SMFe during space weathering. One is solar wind ion implantation by which iron particles are ejected from its lattice sites in soil grains via bombardment by implanted high energy solar wind ions. The sputtered iron particle leaves soil surface as a single, uncharged atom, and redeposits on the surface of adjacent soil grains (*Hapke*, 1965, 2001; *Stern*, 1999; *Crider and Vondrak*, 2002). This process can be facilitated by chemical reduction of ferrous iron to metallic iron as a result of injected H^+ into soil grains with release of OH^-/H_2O (*Zeller et al*., 1966; *Housley et al*., 1973). The other mechanism is meteoroid/micrometeoroid impacts (*Hapke et al*., 1970; *Housley*, 1979; *Hapke*, 2001). Because of continuous meteoroid/micrometeoroid bombardment, soil grains are partially vaporized so that some of the material (e.g., FeO) is dissociated into its constituent neutral atoms (*Housley*, 1979; *Kramer et al*., 2011). During this process, the more easily vaporized elements such as iron are preferentially deposited on the surface of other soil grains as a layer of amorphous rim containing high mass fractions of SMFe (*Hapke et al*., 1970; *Hapke*, 2001). In addition to the production of SMFe, space weathering can reduce the particle size (PS) of lunar soils due to the impacts of meteoroids/micrometeoroids, and a new material termed "agglutinate"

is generated which is the aggregate of mineral fragment cemented by impact induced glass (*Pieters et al*., 2000; *Lucey et al*., 2006). With long exposure time to space environment, fresh lunar soils are weathered, accumulate more SMFe and gradually change to mature ones accompanied by their PS reduction (*Lucey et al*., 2000).

[Insert Figure 1-1 here]

Space weathering significantly influences the measured reflectance spectra of the Moon. Accurately assessing the mineralogy and composition of the Moon from remote sensing data requires a viable model that is capable of describing the spectral effect of space weathering. Hapke's radiative transfer model (RTM) is the most widely used method (*Hapke*, 1981, 2001, 2005) because it can not only simulate the reflectance spectra of immature lunar soils but also model the reddening, darkening and the subdued spectral contrast effects of space weathering. Lunar soil reflectance is mainly controlled by its absorption coefficient (α) which determines the proportion of incident light that is absorbed by lunar soils. *Hapke* (2001) provided an equation to compute the absorption coefficient of space weathered lunar soils:

$$\alpha = \frac{4\pi n_h k_h}{\lambda} + \frac{36\pi z M_c \rho_h}{\lambda \rho_{Fe}}, \quad (1)$$

where M_c is the mass fraction of SMFe in lunar soils, n_h and k_h are the real part and imagery part of refractive index of host soil grains. ρ_h and ρ_{Fe} are the density of host soil grains and SMFe, λ is wavelength, and z is a parameter that can be calculated by the refractive index of host soil grains and SMFe (*Hapke*, 2001). The first term on the right side of Eq. 1 represents the absorption of host soil particles. The second term on the right side of Eq. 1 represents the amount of light absorbed by SMFe coating on the surface of host soil grains. SMFe is the main product by space weathering and the spectral variation

of lunar soils strongly depends on the variation of the mass fraction of SMFe which is included in the second term on the right side of Eq. 1. Therefore, it is based on Eq. 1 that the space weathering effects are accommodated by Hapke's model. Combine Eq. 1 with lunar soil PS, the abundance of different minerals making up lunar soils and other equations in Hapke's model (*Hapke*, 1981, 2005), lunar soil spectra can be reproduced.

2. Literature Review and Limitations in Previous Studies

A number of studies have been carried out to investigate the spectral effect of space weathering. *Moroz et al*. (1996) simulated micrometeoroid impacts of space weathering by laser irradiation on olivine and clinopyroxene mixtures, and found that the magnitude of reflectance decreased as much as 30% after laser irradiation. Similar result was obtained by *Yamada et al*. (1999), whose work showed that the magnitude of reflectance of olivine decreased from 0.88 to 0.47 after laser irradiation in addition to a remarkable reddening tendency. On the basis of multi-spectral imagery and near-infrared spectrometer observations of Psyche crater on 433 Ero asteroid, *Clark et al*. (2001) reported that a 32% albedo contrast between bright and dark materials of Psyche crater could be best explained by space weathering. These studies focused on analyzing how significantly space weathering can alter spectral reflectance, but the spectral effect of other influential factors such as mineral abundance and PS of soil grains has not been fully investigated yet (*Adams*, 1974, 1975; *McCord et al*., 1981; *Clouts et al*., 1986; *Burns*, 1993; *Serventi et al*., 2012, 2013), this determination is required to explore the relative contribution of these factors and space weathering to the reflectance spectra of lunar soils, and to investigate how space weathering interferes with spectral estimation of lunar mineral abundance.

Hapke's RTM has been widely applied to derive mineral abundances for space weathered lunar soils and asteroid surfaces because of its capacity in describing space weathering process (*Clark et al*., 2001; *Lucey*, 2004; *Cahill and Lucey*, 2007; *Lawrence and Lucey*, 2007; *Denevi et al*., 2008; *Cahill et al*., 2010). *Cahill et al*. (2010) evaluated the mineralogy and composition of 19 lunar mare and highland samples based on Hapke's RTM. Although the modeled reflectance spectra of these samples agreed well with measured data, there was a relative large deviation between measured and predicted mineral abundances. A global determination of mineral abundances on the surface of the Moon using Hapke's RTM indicated that the predicted mineral abundance was only accurate for fresh lunar soils (*Lucey*, 2004). Considering all the major components on the lunar surface, *Li and Li* (2011) estimated mineral abundances of 57 lunar mare and highland soil samples via Hapke's RTM. Similar to the results of *Lucey* (2004), mineral abundances can be accurately determined for fresh lunar soils although the modeled reflectance matched the measured data well. *Li and Li* (2011) suggested that the poor performance of Hapke's RTM in estimating mineral abundance for mature lunar soils may result from inaccurate description of the space weathering effects using Eq. 1. Hapke's RTM only considered the effects of smaller size SMFe (<50 nm) coating on the surface of lunar soil grains, while ignored the larger size SMFe (>50 nm) inside agglutinitic glass which is built up via coalescence of smaller SMFe within soil grains during impact melting (*James et al*., 2002, 2003). Experimental work has demonstrated the strong dependence of the SMFe spectral effect on its grains size (*Nobel et al*., 2007). Smaller size SMFe increases the spectral slope over the visible to near-infrared wavelength region (reddening and darkening), whereas larger SMFe tends to reduce the overall reflectance with little effect

on continuum slope (only darkening). Therefore, it is necessary to take into account both smaller and larger size SMFe in order to improve the accuracy of mineral abundance estimation in mature lunar soils. This is also central for deciphering some mysterious features on the lunar surface such as bright swirls, through which we can gain insight into the major mechanism of space weathering.

The relative role of solar wind implantation versus meteoroid/micrometeoroid impacts in space weathering process has been a controversy for several decades (*Pieters et al*., 2000; *Hapke*, 2001; *Marchi et al*., 2006; *Hiroi et al*., 2006; *Willman et al*., 2008). Based on a long period observation of Mercury surface, *Hapke* (1977) found a lack of polar darkening and a decreased density of ray craters in spite of the presence of a magnetic field in the Polar Regions. This result implies that the dominant soil darkening process on Mercury, and by extension, on the Moon is not dependent on the solar wind as opposed to meteoroid/micrometeoroid impacts, which is the primary mechanism of space weathering. However, recent work has identified an inverse correlation between the degree of reddening of asteroid with their distance from the sun, and demonstrated that the solar wind implantation is likely the dominant mechanism (*Marchi et al*., 2006). In addition to remote observations, many laboratory experiments have been performed to understand the relative efficiency and time-scale of these two mechanisms of space weathering (*Yamada et al*., 1999; *Sasaki et al*., 2001). *Yamada et al*. (1999) used a nanosecond pulsed laser on the pellet of silicate minerals to simulate meteoroid/micrometeoroid impacts of space weathering. Results indicated that a time-scale of 10^8 years could result in evident darkening and reddening of silicate spectra after exposed to micrometeoroid bombardment. They also modeled the solar wind implantation by irradiating silicate samples with protons;

however, no remarkable spectral change was observed. *Sasaki et al*. (2001) repeated this experiment and confirmed that, in addition to the apparent spectral change of silicate samples after laser irradiation, an amorphous rim containing SMFe was formed on the surface of silicate minerals, similar to those SMFe observed in the rims of space weathered lunar soils. These two laser irradiation experiments strongly support micrometeoroid impacts as the primary mechanism of space weathering. On the other hand, a recent ion irradiation experiment simulating solar wind ion implantation has led to the conclusion that solar wind implantation should be the dominant mechanism of space weathering (*Brunetto and Strazzulla*, 2005; *Strazzulla et al*., 2005; *Brunetto et al*., 2006; *Loeffler et al*., 2009). *Brunetto and Strazzulla* (2005) irradiated several silicate minerals using different ions (H^+, He^+, Ar^+, Ar^+) to simulate the effects of space weathering induced on asteroid by solar wind, and found that solar wind ions can redden the surface spectra of asteroid on a time-scale lower than 10^6 years (100 times faster than micrometeoroid impacts). *Loeffler et al*. (2009) studied the effect of 4 KeV He^+ ion irradiation on olivine, reported that at 1 AU the spectral reddening caused by the solar wind is approximately 2 orders of magnitude faster than that caused by micrometeoroid impacts, supported the contention that the solar wind implantation as the dominant mechanism of space weathering. According to the derived correlation between spectral slope and the age of young asteroid families, *Vernazza et al*. (2009) suggested a very rapid space weathering process – the final color of a silicate-rich asteroid is acquired within 10^6 years after its birth, and hence favored solar wind ion implantation as the primary mechanism of space weathering.

3. Objectives

On the basis of aforementioned work and their limitations, the main objectives of this thesis are:

(1) To compare the relative contribution of space weathering and mineral abundance on the reflectance spectral of lunar soils and to investigate how space weathering interferes with spectral estimation of mineral abundance of lunar soils;

(2) To develop an improved Hapke's RTM that can effectively accommodate SMFe effects and enhance the estimation accuracy of mineral abundance from remote sensing data;

(3) To analyze the relative role of solar wind ions implantation and micrometeoroid bombardment in space weathering on the basis of testing three major hypotheses for the formation of lunar swirls using Hapke's RTM.

4. Structure of the Thesis

Based on the description in sections 2 and 3 of this chapter, space weathering not only results in the formation of SMFe but also alters the PS distribution of lunar soils. Both SMFe and PS have strong impacts on lunar soil reflectance, which is expected to interfere with the estimation of mineral abundance using Hapke's RTM. This creates a great challenge to accurately estimate mineral abundance on the lunar surface from measured reflectance using Hapke's RTM. Therefore, it is necessary to determine the relative contribution of space weathering and mineral abundance to the reflectance spectra of lunar soils, and assess how SMFe, PS and mineral abundance control spectral variation of lunar soils. To reach this goal, a variance based sensitivity analysis-Extended Fourier Amplitude Sensitivity Test (EFAST)-was conducted with the simulated reflectance spectra of Hapke's RTM in Chapter 2, and the main contribution of each factor (SMFe, PS, and mineral

abundance) to the reflectance spectra was determined in addition to the interaction among factors (e.g., interaction between different minerals). Results indicated that SMFe and PS of lunar soil grains have the strongest impacts across the whole wavelength regions of interest as compared to that of mineral abundance.

Sensitivity analysis for Hapke's RTM in Chapter 2 has shown a significant impact of SMFe on the performance of Hapke's RTM. Lunar soils contain both smaller and larger size SMFe, and their spectral effects are different (*James et al*., 2002, 2003; *Nobel et al*., 2007). However, the equation used in Hapke's RTM (Eq. 1) is only applicable for describing the spectral effect of small size SMFe in the rims of weathered minerals, not for larger size SMFe in the interior of agglutinitic glass. In Chapter 3, an equation describing the effects of larger size SMFe in agglutinitic glass (*Lucey and Riner*, 2011) was incorporated into the original Hapke's RTM. Building this modification on the frame work of *Li and Li* (2011) led to an improved Hapke's RTM. This modified Hapke's model was tested with the Lunar Soil Characterization Consortium (LSCC) dataset. Results revealed that accuracy of abundance estimates for agglutinitic glass, pyroxene, and plagioclase was significantly improved for both immature and mature lunar soils, although there is a poor agreement between measured and modeled mineral abundance for ilmenite, olivine and volcanic glass which only account for a small portion of lunar soils.

In Chapter 4, the dominant mechanism of space weathering (solar wind implantation versus micrometeorite impacts) was analyzed through exploration of the formation of lunar swirls. Lunar swirls are high albedo, optically immature regions on the Moon (Fig. 1-2). They are coincident with regions possessing high magnetic field strength, but not associated with distinct topography (*Blewett et al.,* 2011). One leading hypothesis for the

formation of lunar swirls is the solar wind ions deflection by magnetic anomalies meaning that implanted solar wind ions are deflected away from on-swirl surfaces and focused onto off-swirl surfaces, resulting in enhanced production of smaller size SMFe in off-swirl regions (*Hood and Schubert,* 1980). This process also enhances the possibility of building up of larger size SMFe via coalescence of abundant smaller SMFe. The immature on-swirl surfaces relative to off-swirl surfaces result from deficiency of both smaller and larger size SMFe in on-swirl regions. If this hypothesis is valid, solar wind implantation should be the main mechanism of space weathering. Otherwise, the mass fraction of smaller and larger size SMFe difference between on- and off-swirl surfaces would be absent because magnetic field cannot block micrometeorite impacts. To validate whether the solar wind deflection model is correct, the improved Hapke's RTM developed in Chapter 3 was used to estimate mass fraction of both smaller and larger size SMFe from measured reflectance spectra for on- and off-swirl regions. In addition, the cometary impact model and dust transport model (*Schultz and Srnka,* 1980; *Garrick-Bethell et al.,* 2011) which are another two major hypotheses for the formation of lunar swirls were also investigated using Hapke's RTM. Results showed that off-swirl regions are indeed enriched in both smaller and larger size SMFe than on-swirl regions and the solar wind deflection model is a valid hypothesis for the formation of lunar swirls. The cometary impact model and the dust transport model were ruled out because of their inability in accounting for the spectral difference between on- and off-swirl regions. These results strongly suggested that solar wind ions implantation is the major mechanism of space weathering.

[Insert Figure 1-2 here]

Figure Captions

Figure 1-1. (*Hapke,* 2001) Spectral comparison between pulverized lunar rocks and mature lunar soils. Solid line is the spectrum of a pulverized lunar rock sample unaffected by space weathering. Dashed line is the spectrum of a mature lunar sample strongly affected by space weathering.

Figure 1-2. (*Blewett et al*., 2011) The Reiner Gamma Formation, the type occurrence of a lunar swirl. Clementine color composite image: red (R) = 950 nm, green (G) = 750 nm, and blue (B) = 415 nm.

Figures

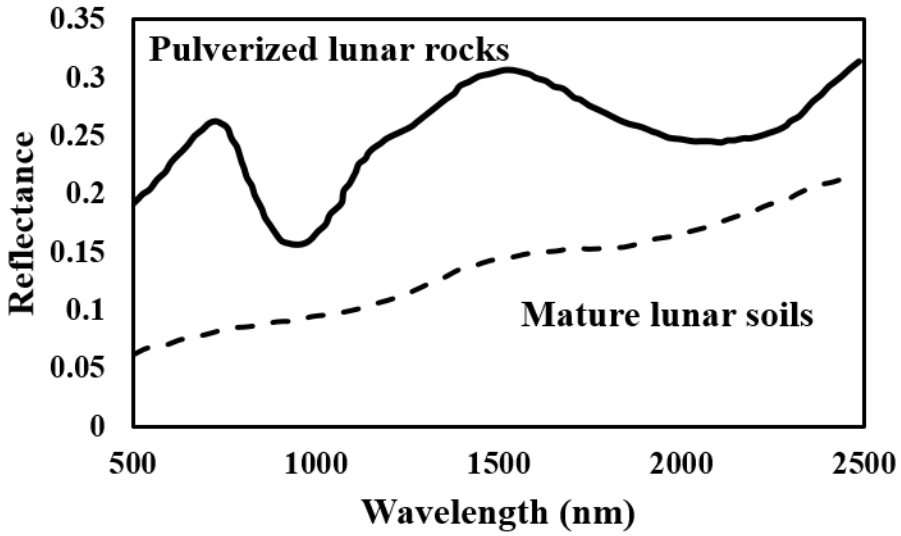

Figure 1-1

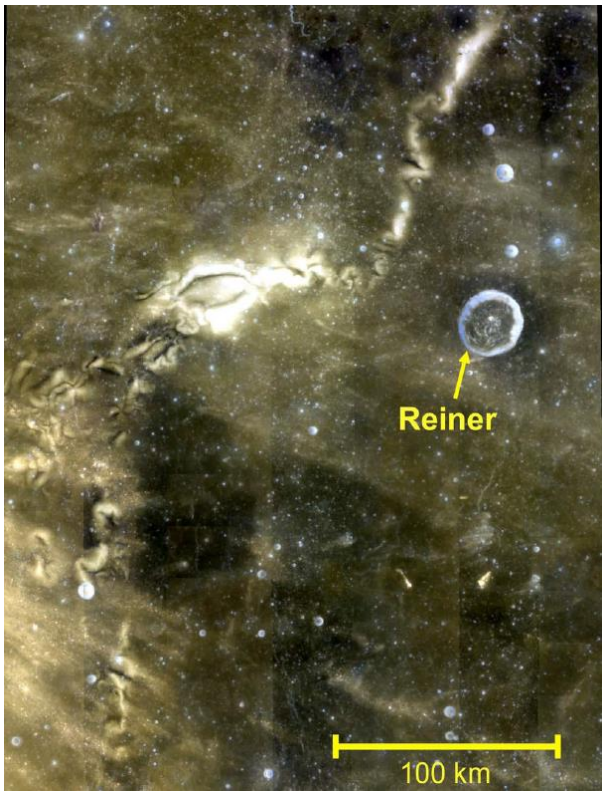

Figure 1-2

References

Adams, J. B., and T. B. McCord (1971), Alteration of lunar optical properties: age and composition effects, *Science* 171, 567-571.

Adams, J. B. (1974), Visible and near-infrared diffuse reflectance spectra of pyroxene as applied to remote sensing of solid objects in the solar system, *J. Geophys. Res*. - *Planets* 79, 4829-4836.

Adams, J. B. (1975), Interpretation of visible and near-infrared diffuse reflectance spectra of pyroxenes and other rock forming minerals, *Infrared and Raman Spectroscopy of lunar and Terrestrial Materials*, 91-116.

Blewett, D. T., E. I. Coman, B. R. Hawke, J. J. Gillis-Davis, M. E. Purucker, and C. G. Hughes (2011), Lunar swirls: Examining crustal magnetic anomalies and space weathering trends, *J. Geophys. Res*. - *Planets* 116, E02002.

Brunetto, R., and G. Strazzulla (2005), Elastic collisions in ion irradiation experiments: A mechanism for space weathering of silicates, *Icarus* 179, 265-273.

Brunetto, R., P. Vernazza, S. Marchi, M. Birlan, M. Fulchignoni, V. Orofino, and G. Strazzulla (2006), Modeling asteroid surfaces from observations and irradiation experiments: The case of 832 Karin, *Icarus* 184, 327-337.

Burns, R. G. (1993), Mineralogical applications of crystal field theory, Vol. 5. Cambridge University Press, New York.

Cahill, J. T. S., and P. G. Lucey (2007), Radiative transfer modeling of lunar highlands spectral classes and relationship to lunar samples, *J. Geophys. Res*. – *Planets* 112, E10007.

Cahill, J. T. S., P. G. Lucey, K. R. Stockstill-Cahill, and B. R. Hawke (2010), Radiative transfer modeling of near-infrared reflectance of lunar highland and mare soils, *J. Geophys. Res. - Planets* 115, E12019.

Chapman, C. R. (1996), S-type asteroids, ordinary chondrites, and space weathering: the evidence from Galileo's fly-bys of Gaspra and Ida, *Meteorit. Planet. Sci*. 31, 699 - 725.

Chapman, C. R. (2004), Space weathering of asteroid surfaces, *Annu. Res. Earth Planet. Sci*. 32, 539-67.

Clark, B. E., et al. (2001), Space weathering on Eros: Constraints from albedo and spectral measurements of Psyche crater, *Meteorit. Planet. Sci*. 36, 1617-1637.

Clouts, E. A., M. J. Gaffey, T. L. Jackowski, and K. L. Reed (1986), Calibrations of phase abundance, composition, and particle size distribution for olivine-orthopyroxnene mixtures from reflecatnce spectra, *J. Geophys. Res. - Planets* 91, 11641-11653.

Crider, D. H., and R. R. Vondrak (2002), Hydrogen migration to the lunar poles by solar wind bombardment of the moon, *Adv. Space Res*. 30, 1869-1874.

Denevi, B. W., P. G. Lucey, and S. B. Sherman (2008), Radiative transfer modeling of near-infrared spectra of lunar mare soils: Theory and measurement, *J. Geophys. Res. - Planet* 113, E02003.

Fischer, E. M., and C. M. Pieters (1994), Remote determination of exposure degree and iron concentration of lunar soils using VIS-NIR spectroscopic methods, *Icarus* 111, 475-488.

Garrick-Bethell, I., J. W. Head, and C. M. Pieters (2011), Spectral properties, magnetic fields, and dust transport at lunar swirls, *Icarus* 212, 480–492.

Garrick-Bethell, I. et al. (2015), Nanowarm: a cubesat discovery mission to study space weathering, lunar magnetism, lunar water, and small-scale magnetospheres. *Lunar Planet. Sci. 46*, 3000.

Hapke, B. (1965), Effects of a simulated solar wind on the photometric properties of rocks and powders, *Ann. N. Y. Acad. Sci.* 123, 711-721.

Hapke, B., A. Cohen, W. Cassidy, and E. Wells (1970), Solar radiation effects on the optical properties of Apollo 11 lunar samples, *Proc. Apollo 11 lunar Sci. Conf.* 2199-2212.

Hapke, B. (1977), Interpretations of optical observations of mercury and the Moon, *Phys. Earth Planet. Interi.* 15, 264-274.

Hapke, B. (1981), Bidirectional reflectance spectroscopy: I. Theory, *J. Geophys. Res*. 86, 3039-3054.

Hapke, B. (2001), Space weathering from Mercury to the asteroid belt, *J. Geophys. Res*. - *Planets* 106, 10039-10073.

Hapke, B. (2005), Theory of reflectance and emittance spectroscopy, Cambridge University Press, Cambridge, New York.

Hiroi, T., M. Abe, K. Kitazato, S. Abe, B. E. Clark, S. Sasaki, M. Ishiguro and O. S. Barnouin-Jha (2006), Developing space weathering on the asteroid 25143 Itokawa, *Nature* 443, 56 - 58.

Housley, R. M., R. W. Grant, and N. E. Paton (1973), Origin and characteristics of excess Fe metal in lunar glass welded aggregates, *Proc. Lunar Planet. Sci. Conf*. 4, 2737 – 2749.

Housley, R. M., (1979), A model for chemical and isotopic fractionation in the lunar regolith by impact vaporization, *Proc. Lunar Planet. Sci. Conf.* 10, 1673-1683.

Hood, L. L., and G. Schubert (1980), Lunar magnetic anomalies and surface optical properties, *Science* 208, 49–51.

James, C. L., S. L. Letsinger, A. Basu, S. J. Wentworth, and D. S. McKay (2002), Size Distribution of Fe0 Globules in Lunar Agglutinitic Glass, *paper presented at Lunar and Planetary Science Conference*.

James, C. L., S. L. Letsinger, A. Basu, S. J. Wentworth, and D. S. McKay (2003), Nanophase iron globules in lunar soils, *Proc. Lunar Planet Sci. Conf.* 34, 1992.

Keller, L. P., and D. S. Mckay (1993), Discovery of vapor deposits in the lunar regolith, *Science* 261, 1305-1307.

Keller, L. P., and D. S. McKay (1997), The nature and origin of rims on lunar soil grains, *Geochim. Cosmochim. Ac*. 61, 2331-2341.

Kramer, G. Y., J. P. Combe, E. M. Harnett, B. R. Hawke, S. K. Noble, D. T. Blewett, T. B. McCord, and T. A. Giguere (2011), Characterization of lunar swirls at Mare Ingenii: A model for space weathering at magnetic anomalies, *J. Geophys. Res. - Planets* 116, E04008.

Lawrence, S. J., and P. G. Lucey (2007), Radiative transfer mixing models of meteoritic assemblages, *J. Geophys. Res. - Planet* 112, E07005.

Li, S., and L. Li (2011), Radiative Transfer Modeling for quantifying lunar surface minerals, particle size and submicroscopic metallic Fe. *J. Geophys. Res. - Planets* 116, E09001.

Lucey, P. G., T. B. David, G. J. Taylor, and B. Ray Hawke (2000), Imaging of lunar surface maturity, *J. Geophys. Res. – Planets* 105, 20377-20386.

Lucey, P. G. (2004), Mineral maps of the Moon, *Geophys. Res. Lett*. 31, L08701.

Lucey, P., R. L. Korotev, J. J. Gillis, L. A. Taylor, D. Lawrence, B. A. Campbell, R. Elphic, B. Feldman, L. L. Hood, D. Hunten, M. Mendillo, S. Nobel, J. J. Papike, R. C. Reey, S. Lawson, T. Prettyman, O. Gasnault, and S. Maurice (2006), Understanding the lunar surface and space-moon interactions, *Rev. Mineral. Geochem.* 60, 83-219.

Lucey, P. G, and M. Riner (2011), The optical effects of small iron particles that darken but do not redden: evidence of intense space weathering on Mercury, *Icarus* 212, 451-462.

Loeffler, M. J., C. A. Dukes, and R. A. Baragiola (2009), Irradiatio of olivine by 4 keV He^{+}: Simulation of space weathering by the solar wind, *J. Geophys. Res. - Planets* 114. E03003.

Marchi, S., P. Paolicchi, M. Lazzarin, and S. Magrin, (2006), A general spectral slope-exposure relation for S-type main belt and near-earth asteroids, *Astron. J.* 131, 1138-1141.

McCord, T. B., and T. V. Johnson (1970), Lunar spectral reflectivity (0.30 to 2.50 microns) and implications for remote mineralogical analysis, *Science* 169, 855-858.

McCord, T. B., and J. B. Adam (1973), Progress in remote optical analysis of lunar surface composition, *Moon* 7, 453-474.

McCord, T. B., R. N. Clark, B. R. Hawke, L. A. McFadden, P. D. Owensby, C. M. Pieters, and J. B. Adams (1981), Moon: near-infrared spectral reflectance, a first good look, *J. Geophys. Res. – Solid Earth* 86, 10883-10892.

Moroz, L. V., A. V. Fisenko, and L. F. Semjonova (1996), Optical effects of regolith processes on S-Asteroids as simulated by laser shots on ordinary chondrite and other mafic materials, *Icarus* 122, 366-382.

Noble, S. K., C. M. Pieters, and L. P. Keller (2007), An experimental approach to understanding the optical effects of space weathering, *Icarus* 192, 629-642.

Nobel, S. K., and C. M. Pieters (2003), Space weathering on Mercury: Implications for remote sensing, *Sol. Syst. Res.* 37, 31-35.

Pieters, C. M., E. M. Fischer, O. Rode, and A. Basu (1993), Optical effects of space weathering - the role of the finest fraction, *J. Geophys. Res. – Planets* 98, 20817-20824.

Pieters, C. M., L. A. Taylor, S. K. Noble, L. P. Keller, B. Hapke, R. V. Morris, C. C. Allen, D. S. McKay, and S. Wentworth (2000), Space weathering on airless bodies: resolving a mystery with lunar samples, *Meteorit. Planet. Sci*. 35, 1101-1107.

Pieters, C. M., and I. Garrick-Bethell (2015), Hydration variations at lunar swirls. *Lunar Planet. Sci*. 46, 2120.

Sasaki, S. K. Nakamura, Y. Hamabe, E. Kurahashi, and T. Hiroi (2001), Production of iron nanoparticles by laser irradiation in a simulation of lunar-like space weathering, *Nature* 410, 555-557.

Serventi, G., C. Carli, M. Sgavetti, and L. Pompilio (2012), Effects of plagioclase chemistry and modal abundance on spectral properties of multi-mineral Fe, Mg mixtures, *Proc. Lunar Planet. Sci. Conf*. 43, 1404.

Serventi, G., C. Carli, and M. Sgavetti (2013), Plagioclase influence in mixtures with very low mafic mineral content, *Proc. Lunar Planet. Sci. Conf*. 44, 1490.

Stern, A., (1999), The lunar atmosphere: History, status, current problems, and context, *Rev. Geophys*. 37, 453-491.

Strazzulla, G., E. Dotto, R. Binzel, R. Brunetto, M. A. Barucci, A. Blanco, and V. Orofino (2005), Spectral alteration of the Meteorite Epinal (H5) induced by heavy ion irradiation: a simulation of space weathering effects on near-Earth asteroids, *Icarus* 174, 31-35.

Schultz, P. H., and L. J. Srnka (1980), Cometary collisions with the Moon and Mercury, *Nature* 284, 22–26.

Taylor, L. A., C. M. Pieters, L. P. Keller, R. V. Morris, and D. S. McKay (2001), Lunar Mare Soils: Space weathering and the major effects of surface-correlated nanophase Fe, *J. Geophys. Res*. - *Planets* 106, 27985-27999.

Taylor, L. A., C. M. Pieters, A. Patchen, D. S. Taylor, R. V. Morris, L. P. Keller, and D. S. Mckay (2010), Mineralogical and chemical characterization of lunar highland soils: Insights into the space weathering of soils on airless bodies, *J. Geophys. Res*. – *Planets* 115, E02002.

Vernazza, P., R. P. Binzel, A. Rossi, M. Fulchignoni, and M. Birlan (2009), Solar wind as the origin of rapid reddening of asteroid surfaces, *Nature* 458.

Willman, M., R. Jedicke, D. Nesvorny, N. Moskovitz, Z. Ivezic, and R. Fevig (2008), Redetermination of the space weathering rate using spectra of Iannini asteroid family members, *Icarus* 195, 663-673.

Yamada, M., S. Sasaki, H. Nagahara, A. Fujiware, S. Hasegawa, H. Yano, T. Hiroi, H. Ohashi, and H. Otake (1999), simulation of space weathering of planet-forming

materials: Nanophase pulse laser irradiation and proton implantation on olivine and pyroxene samples, *Earth Planets Sp.* 51, 1255-1265.

Zeller, E. J., L. B. Ronca, and P. W. Levy (1996), Proton-induced hydroxyl formation on the lunar surface, *J. Geophys. Res*. 71, 4855-4860.

CHAPTER 2

SENSITIVITY ANALYSIS FOR HAPKE'S RADIATIVE TRANSFER MODEL

Abstract

Hapke's radiative transfer model (RTM) is the most commonly used method to estimate mineral abundance on the lunar surface due to its capacity in accounting for the physical and chemical properties of lunar soils and for space weathering effects. Many factors influence the performance of Hapke's RTM such as particle size (PS) of soil grains, mass fraction of submicroscopic iron (SMFe), abundance and refractive index of minerals, as well as viewing geometry. In this study, we used Extended Fourier Amplitude Sensitivity Test (EFAST), a variance-based sensitivity analysis (SA), to quantitatively investigate the relative importance of PS, mass fraction of SMFe and mineral abundance in regulating Hapke's simulated reflectance spectra. Results show that the simulated reflectance are highly sensitive to PS and mass fraction of SMFe at all wavelengths. In contrast, the abundance of minerals merely accounts for a small portion of variation of output reflectance. This creates challenges for deriving mineral abundance, PS and mass fraction of SMFe simultaneously from measured reflectance spectra. Prior knowledge on the PS and mass fraction of SMFe of lunar soils is required for accurate prediction on the mineral abundance of lunar soils via Hapke's RTM. In addition, the 1000 nm and 2000 nm absorptions of simulated reflectance are more sensitive to the variation of abundance of pyroxene, and reflectance between 1200 nm and 1400 nm rather than assumed 1050 nm are most sensitive to the variation of abundance of olivine. When Hapke's RTM is applied to estimate mineral abundance of lunar soils, the estimation accuracy could be potentially improved by choosing 1000 nm and 2000 nm for pyroxene, and wavelength regions between 1200 nm and 1400 nm for olivine.

1. Introduction

Determination of the abundance and distribution of minerals on the lunar surface is of considerable interest for lunar scientists. It helps advance our understanding of the lunar evolution history and the crust structure and composition (*Wood*, 1975; *Tompkins*, 1999; *Jolliff et al*., 2000; *Wieczorek and Phillips*, 2000; *Hiesinger and Head*, 2006). Visible and near-infrared reflectance spectroscopy has been an important tool for compositional mapping of the lunar surface by use of diagnostic spectral features of dominant lunar minerals (*Adams and McCord*, 1970, 1972; *McCord and Adams*, 1973; *Charette et al*., 1974; *McCord et al*., 1981; *Pieters*, 1986). For example, the presence of 1 μm and 2 μm absorptions in the spectra of lunar soils is indicative of pyroxene. Although the reflectance spectra of the lunar surface are mainly dominated by pyroxene (*Adams*, 1974; *McCord et al*., 1981; *Noble et al*., 2006), abundant olivine is responsible for a broad Fe^{2+} absorption with the band minima close to 1.05 μm (*Burns*, 1970, 1993; *Sunshine et al*., 1990; *Sunshine and Pieters*, 1998; *Isaacson and Pieters*, 2010), and crystalline plagioclase results in an apparent absorption band around 1.25 μm (*Adams*, 1975; *McCord et al*., 1981; *Burns*, 1993; *Ohtake et al*., 2009; *Serventi et al*., 2012, 2013). However, identification and quantification of these typical lunar minerals could be complicated by a few compositional and physical properties of lunar soils as a result of space weathering on the Moon. Space weathering is known as continuous implantation of solar wind ions and the bombardment of micrometeorites on the lunar surface, and results in accumulation of fine-grained submicroscopic iron (SMFe) either in the rims of soil grains or in the interior of agglutinitic glasses (*McCord and Adams*, 1973; *Morris*, 1977, 1980; *Keller and Mckay*, 1993, 1997; *Keller et al*., 2000; *Keller and Clem*ett, 2001; *James et al*., 2002). The fine-grained SMFe

can significantly alter the optical properties of lunar soils, and this alteration is manifested as an overall reduction of reflectance, attenuated absorption strength and the creation of a red-sloped continuum (*Fischer and Pieters*, 1994; *Pieters et al.*, 1993, 2000; *Hapke*, 2001; *Noble et al.*, 2001, 2007; *Lucey and Noble*, 2008). Another apparent effect of space weathering is modification to the size of lunar soil grains due to comminution in space weathering, leading to a change to lunar soil reflectance (*Adams and Filice*, 1967; *Pieters*, 1983; *Clark and Roush*, 1984; *Hiroi and Pieters*, 1992; *Johnson et al*., 1992; *Shkuratov et al*., 1999). *Adams and Filice* (1967) and *Pieters* (1983) measured the reflectance of a suite of transparent materials of different particle size (PS) and observed that there is an increase in reflectance and a decrease in absorption band with decreasing PS.

The influence of different factors on the reflectance spectra of lunar soils has been investigated using the model simulations approach (*Hapke*, 1981; *Shkuratov et al*., 1999). The model simulation approach has advantages over lab spectral measurement because all the probable scenarios that possibly occur on the lunar surface such as different combinations of mineral abundances, variations in the SMFe content and PS of soil grains can be fully explored without being limited by the availability of lunar soil samples (*Li and Li*, 2011). For example, the model simulation approach allows us to focus on the spectral effects of factors of interest by varying their values in the modeling process, but fixing the values of other factors.

The effects of SMFe, PS, and mineral abundance have been examined by a number of investigators using Hapke's radiative transfer model (RTM), a widely used method that allows for simulation of the reflectance spectra of lunar soils (*Hapke*, 1981, 2001, 2005). In Hapke's model, reflectance at a particle phase function ($P(g)$) and a viewing geometry

(*Hapke*, 2005) can be related to refractive index (*n* and *k*) and PS of each of primary minerals contained in lunar soil samples with a specified mass fraction of SMFe via single scattering albedo (SSA). *Warell and Davidsson* (2010) used Hapke's model to fit measured reflectance spectra for plagioclase, olivine and pyroxene, and showed that a smaller variation of PS in Hapke's model could cause a more than 30% change to the magnitude of simulated reflectance. *Lucey* (1998) applied Hapke's model to derive *k* spectra for a suite of clinopyroxene samples with similar compositions but different PS, and found that a 10% offset of derived *k* spectra from the mean could be compensated by a very small change of input PS. *Denevi et al.* (2008) employed Hapke's RTM to simulate reflectance spectra of clinopyroxene and orthopyroxene mixtures with known mineral chemistry, and showed that the misfit between measured and simulated reflectance spectra can be corrected by slightly adjusting PS rather than increasing mineral abundance of orthopyroxene by a significant amount (e.g., 30%).

Hapke (2001) later proposed a detailed radiative transfer treatment to the effect of SMFe on a particulate surface and successfully mimicked reddening, darkening and subdued spectra contrast induced by SMFe. This improvement to Hapke's model makes it possible to quantitatively describe the spectral effect of SMFe. Results showed that the modeled spectra changed from a flat line with an apparent absorption band around 1.0 μm to an almost oblique straight line without evident absorption at 1.0 μm. *Lucey* (2008) explored the effect of SMFe on the simulated reflectance by fitting measured spectra of silica gel powder samples that infused with varying mass fraction of SMFe. A result similar to that presented by *Hapke* (2001) was obtained, i.e. that the continuum of the spectra increased with increasing SMFe, the reflectance at 1.5 μm decreased by more than 50%.

Ohtake et al. (2009) demonstrated that the image spectra with a higher magnitude of reflectance and a broad absorption band centered near 1.25 μm identified globally on the lunar surface can be best explained by soils contain as much as >98% plagioclase on the basis of spectral unmixing using Hapke's RTM. This implies that the presence of high abundance of plagioclase can lead to increased magnitude of reflectance and an absorption feature around 1.25 μm of simulated reflectance spectra. *Yamamoto et al*. (2010) applied Hapke's RTM to fit the image spectra of 245 points on the lunar surface that possess a broad absorption with minima at 1.05 μm, and concluded that these points should contain high olivine (> 40%). Results of this study also indicated that the 1.05 μm apparent broad absorption in a simulated reflectance curve can be attributed to the presence of abundant olivine.

In addition to the strong dependence of Hapke's RTM on PS, mass fraction of SMFe and mineral abundance, other factors such as viewing geometry, refractive index of silicate minerals (associated with Mg number), the back scattering function (*B(g)*), and phase function (*P(g)*) all influence the simulated reflectance (*Hapke and Well*, 1981; *Lucey*, 1998; *Hapke*, 2005; *Wilcox et al.*, 2006; *Denevi et al*., 2007). For example, *Mustard and Pieters* (1989) tested three forms of *P(g)* to derive mineral abundances for lab prepared mineral mixtures using Hapke's RTM. Compared to a constant or an empirical phase function, the result for a two-term legendre polynomial phase function shows the best agreement between known and estimated mineral abundance, indicating the importance of the form of *P(g)* in Hapke's RTM.

Although the performance of Hapke's RTM is affected by many factors as aforementioned, up to date, few investigations have been done to quantitatively assess the

contribution of these factors to the reflectance simulated with Hapke's RTM. Some previous studies only focus the analysis on one factor in Hapke's RTM while other influential factors were fixed (*Denevi*, 2008; *Lucey and Noble*, 2008; *Yamamoto et al*., 2010). To our best knowledge, no previous studies have examined the extent to which the mass fraction of SMFe and PS in lunar soils can interfere with estimation of lunar mineral abundance using Hapke's RTM. In this study, the sensitivity of Hapke's RTM simulated reflectance to the variation of PS, mass fraction of SMFe and mineral abundance was quantitatively determined with the aim of assessing the relative significance of these factors in controlling the simulated reflectance. Meanwhile, examined are spectral interactions between different mineral combinations and the factors (e.g., SMFe, PS) that interfere with spectral estimation of lunar mineral abundance. To reach these research goals, sensitivity analysis (SA) was used to determine the relative importance of different factors on the performance of Hapke's RTM.

Sensitivity analysis is a procedure to quantitatively or qualitatively apportion the variance in the output of a model to different sources of variation and to identify the factors mostly attributed to output variability (*Saltelli et al*, 1999; *Ekström*, 2005). It can also serve as an efficient tool for selecting a specific wavelength region that is most sensitive to the variations in the abundance of minerals making up lunar soils or in the mass fraction of SMFe, and building models for the derivation of the mineral abundance or mass fraction of SMFe.

2. Simulated Spectral Reflectance

Hapke's RTM was run in the forward mode to simulate spectral reflectance spectra, and a detailed description of Hapke's RTM is given in Appendix. The spectral reflectance

simulation via Hapke's RTM requires input factors such as PS, mass fraction of SMFe, abundance and refractive index of minerals, viewing geometry, *P(g)*, and *B(g)*. Here, *P(g)*, *B(g)*, viewing geometry, refractive index of SMFe and minerals were all set to known forms or constant values (Appendix). We only analyzed the sensitivity of Hapke's RTM to PS, mass fraction of SMFe, and abundance of typical lunar minerals including plagioclase, pyroxene and olivine. The ranges of the model variables for which the sensitivity of Hapke's RTM was analyzed were set as following. PS was set between 1 μm and 45 μm similar to that of lunar soils samples analyzed by Lunar Soil Characterization Consortium (LSCC) (*Pieter et al*., 1993). The mass fraction of SMFe ranged from 0% to 1% which is little higher than the commonly assumed values (0% - 0.5%) in lunar soils. This is because although the estimated mass fraction of SMFe in lunar soils by *Morris* (1976, 1980) was about 0-0.5%, a subsequent study showed that the finest fraction of lunar soils could contain mass fraction of SMFe higher than 0.5% (e.g., 79221 = 0.65%) (*Noble et al*., 2001). Furthermore, *Morris* (1980) only measured the mass fraction of SMFe at diameters between 4 nm and 33 nm, and some larger size SMFe (*James et al*., 2002; *Lucey and Riner*, 2011) in lunar soils were not accounted for due to the limitation of ferromagnetic resonance techniques. This limitation may lead to lower estimates of the mass fraction of SMFe than the commonly accepted amounts. The abundance of plagioclase, pyroxene and olivine was set to vary within the range of 0% - 100% to take pure mineral into account. Ilmenite was excluded because of the difference of its optical properties from other silicate minerals with $k >> 1$, violating the assumption of Hapke's RTM (*Hapke*, 2005). Seven groups of simulated reflectance spectra were generated using various combinations of PS, mass fractions of SMFe, abundances of plagioclase, pyroxene and olivine. The detailed

information on the variable inputs for Hapke's RTM to simulate reflectance spectra is presented in Table 2-1.

[Insert Table 2-1 here]

3. Extended Fourier Amplitude Sensitivity Test (EFAST)

A number of SA methods have been put forward to ascertain how a given model depends on its input factors. For example, local SA investigates local response of the outputs of a model by varying one input factor at a time while holding the others fixed to a nominal value. However, the volume of the region explored by this method is nil (*Saltelli et al*., 1999). *Morris* (1991) proposed a screen method to identify active factors in a model and to rank the factors in the order of their importance, but this method cannot be used to determine the percentage of the output variation that each factor can account for (*Saltelli et al*., 1999). Rank-transformed statistics is another SA method presented by *Saltelli et al*. (1993) and *Saltelli and Sobol* (1995), but it only works for monotonic models and not for nonlinear, non-monotonic problems. Fourier Amplitude Sensitivity Test (FAST) is one of the most effective SA method that works for both monotonic and non-monotonic models, and can quantitatively compute the main contribution of each input factor to the output variance (*Cukier et al*., 1978). However, FAST generally fails to describe the effect of interactions among factors. *Saltelli et al*. (1999) proposed the Extended Fourier Amplitude Sensitivity Test (EFAST) method, which not only measures the contribution of each input factor to the output variance, but also takes into account the effect of interaction among factors. Hapke's RTM is highly non-monotonic, and strong interactions may exist between different factors. Therefore EFAST was selected to conduct SA for Hapke's RTM in this study.

The main idea of EFAST is a parametric transformation that reduces multidimensional integrals over the space of the input factors to one-dimensional quadratures through a search curve which scans the whole input space (*Ceccato et al*., 2002). Each axis of the factor space is investigated with a different frequency after the scanning (*Ceccato et al*., 2002). Fourier decomposition is then used to obtain the contribution of each input factors to the output variance of the model. Two sets of indices are given by EFAST: (1) first order sensitivity index (SI), which is the main contribution of each input factor and (2) total sensitivity index (TSI), which not only evaluates the main contribution of each factor but also considers the effect of all interactions involving that factor. Assuming that reflectance spectra $\boldsymbol{Y_{rs}}$ are only controlled by PS ($\boldsymbol{X_{ps}}$), mass fraction of SMFe ($\boldsymbol{X_{Fe}}$) and mineral abundance ($\boldsymbol{X_{mi}}$). The variance of $\boldsymbol{Y_{rs}}$ can be decomposed via EFAST as following:

$$\boldsymbol{V(Y_{rs}) = V(X_{ps}) + V(X_{Fe}) + V(X_{mi}) + V(X_{ps}, X_{Fe}) + V(X_{ps}, X_{mi}) + V(X_{Fe}, X_{mi}) + V(X_{ps}, X_{Fe}, X_{mi})},$$

where $\boldsymbol{V(Y_{rs})}$ is the variance of $\boldsymbol{Y_{rs}}$, $\boldsymbol{V(X_{ps})}$ is the variance of $\boldsymbol{X_{ps}}$, $\boldsymbol{V(X_{Fe})}$ is the variance of $\boldsymbol{X_{Fe}}$, and $\boldsymbol{V(X_{mi})}$ is the variance of $\boldsymbol{X_{mi}}$. $\boldsymbol{V(X_{ps}, X_{Fe})}$, $\boldsymbol{V(X_{Fe}, X_{mi})}$ and $\boldsymbol{V(X_{ps}, X_{mi})}$ represent the variance of interaction between $\boldsymbol{X_{ps}}$ and $\boldsymbol{X_{Fe}}$, $\boldsymbol{X_{Fe}}$ and $\boldsymbol{X_{mi}}$, $\boldsymbol{X_{ps}}$ and $\boldsymbol{X_{mi}}$ respectively. $\boldsymbol{V(X_{ps}, X_{Fe}, X_{mi})}$ represents the variance of interaction among $\boldsymbol{X_{ps}}$, $\boldsymbol{X_{Fe}}$ and $\boldsymbol{X_{mi}}$. The SI of $\boldsymbol{X_{ps}}$ is defined as:

$$\boldsymbol{SI_{X_{ps}} = \frac{V(X_{ps})}{V(Y_{rs})}}$$

and the TSI of $\boldsymbol{X_{ps}}$ is calculated as:

$$\boldsymbol{TSI_{X_{ps}} = \frac{V(X_{ps}) + V(X_{ps}, X_{mi}) + V(X_{ps}, X_{Fe}) + V(X_{ps}, X_{Fe}, X_{mi})}{V(Y_{rs})}},$$

which is the total contribution of PS to the reflectance variance. The difference between TSI and SI values of PS can be used to evaluate the interaction of PS with other factors. Based on the simulated reflectance spectra, EFAST was conducted to estimate the relative importance of input variables and Fig. 2-1 shows the process of how EFAST works.

[Insert Figure 2-1 here]

4. Simulation Experiment

In this study, the TSI values of PS and SMFe for the simulated reflectance spectra of group I, II and III were first calculated via EFAST for the cases that only one mineral exists each time (Table 2-1). This step allows for investigating the sensitivity of Hapke's RTM to SMFe and PS of soil grains without varying mineral abundance. In the next step, EFAST was applied to the simulated reflectance spectra of group IV, V and VI to determine the spectral interaction resulting from different mineral combinations (plagioclase and pyroxene, olivine and plagioclase, olivine and pyroxene) and to identify the wavelength regions in which the interaction is significant. For the last group of simulated reflectance spectra, the sensitivity of Hapke's RTM to the input PS, SMFe, and abundance of the three minerals was determined. EFAST was applied to all seven groups of simulated reflectance spectra in the spectral range between 400 nm and 2500 nm with 5 nm intervals.

5. Analysis for Hapke's Radiative Transfer Model

5.1. Simulated Reflectance Spectra

Shown in Fig. 2-2 is a sub-dataset of simulated reflectance spectra when all the input factors (PS, SMFe, and the abundance of minerals) are allowed to change in the modeling process. Fig. 2-2 illustrates how changing the value of an input factor can alter the reflectance spectra simulated with Hapke's RTM. Spectral curves 1 and 2 represent a case

that increasing PS resulted in a significant decrease in the magnitude of simulated reflectance because of a longer travel distance of light resulting from increasing PS. Spectral curves 3 and 4 are for a case with different mass fractions of SMFe but similar mineral compositions and PS, and show an evident reddening, darkening, and reduced spectra contrast of curve 4 compared to curve 3. Variations in the abundance of minerals also resulted in significant changes in the simulated reflectance spectra: higher reflectance of curve 6 than curve 5 can be attributed to a higher plagioclase abundance for the former than latter; Increasing the abundance of pyroxene resulted in stronger absorption around 1.0 μm and 2.0 μm (curves 7 and 8), and a higher abundance of olivine is responsible for the broad absorption band close to 1.05 μm (curves 9 and 10). All these modeling results are expected and consistent with what are observed on the lunar surface.

[Insert Figure 2-2 here]

5.2. TSI of Particle Size and Submicroscopic Iron

Shown in Fig. 2-3 are TSI values for PS and SMFe considering 100% plagioclase, 100% olivine and 100% pyroxene, respectively. It can be seen that the peak of the TSI curve for PS and the valley of the TSI curve for SMFe are located in the wavelength regions where corresponding minerals absorb, indicating the dominating effects of mineral absorption on the spectral contrast. It is noteworthy that a high negative correlation exists between PS and SMFe. In Hapke's RTM, the internal-transmission factor $\Theta = e^{-\alpha D}$ is defined to describe the total fraction of light entering the particle that reaches another surface after one transmit (*Hapke*, 1981, 2005). Fig. 2-3 represents the cases each with a constant mineral composition, and the simulated reflectance was mainly controlled by Θ. A decreased simulated reflectance can be due to increasing SMFe and thus the absorption of

particles (α), but this reflectance decrease can be offset by a decrease in PS (D). Therefore, the effects of SMFe and PS on the simulated reflectance should be opposite. This is also consistent to the results of *Morris* (1977), *Pieters* (2000) and *Taylor et al*. (2001, 2010) who investigated both lunar highland and mare soils and found that the mass fraction of SMFe in lunar soils dramatically increases with decreasing PS. Therefore, when the reflectance of lunar soils shows high sensitivity to PS, the contribution from SMFe is relatively low. Another apparent trend in Fig. 2-3 is that the TSI values of SMFe are higher than those for PS in short wavelength regions, but opposite in longer wavelength regions. This could be ascribed to the stronger absorption coefficient of SMFe at short wavelengths than longer wavelengths as shown in Fig. 2-4. *Sasaki et al*. (2001, 2002) simulated the space weathering effect using a pulse laser beam to irradiate several mineral samples and found that the reduction of spectra is much larger in the visible than in the near-infrared region, which also validates the strong influence of SMFe at short wavelengths. In addition, the low sensitivity of simulated reflectance to PS at short wavelength regions might account for the convergence of the albedo in short wavelength regions for all size groups of lunar soil samples as noted in the work of *Pieters* (1993) and *Nobel* (2001).

[Insert Figure 2-3 here]

[Insert Figure 2-4 here]

5.3. Interaction between Different Mineral Combinations

Shown in Fig. 2-5b is the spectral interaction between plagioclase and pyroxene calculated by the difference between their TSI and SI values. It can be seen that clear interactions exist around 1000 nm and 2000 nm. This is not unexpected because bright crystalline plagioclase doesn't have apparent absorption at these two wavelengths; when

forming mixtures with pyroxene, plagioclase can reflect light around 1000 nm and 2000 nm, and significantly interferes with the absorption of pyroxene. A relatively strong interaction between plagioclase and olivine is present from 1100 nm to 1400 nm as indicated in Fig. 2-6b. Typical olivine should have a broad, composite absorption feature with one absorption band minima close to 1050 nm (M2 site) and another two absorptions around 850 nm (M1-1 site) and 1250 nm (M1-2 site) due to crystal field transitions of Fe^{2+} (*Burns*, 1970, 1993). Plagioclase on the lunar surface possesses the absorption feature close to 1300 nm (*Burns*, 1993). The 1250 nm absorption of olivine is overlapped with the absorption feature of plagioclase and thus introduces the apparent spectral interaction between 1100 nm and 1400 nm. Shown in Fig. 2-7 is the analysis result for the abundance combinations of olivine and pyroxene. Fig. 2-7b suggests that the interaction between olivine and pyroxene is stronger at wavelength 850 nm and 1050 nm than other wavelengths. These interactions can be attributed to the overlap of the absorption feature of pyroxene around 1000 nm with that of olivine at M2 (1050 nm) and M1-1(850 nm) sites. There is also a higher TSI-SI value close to 1600 nm which is ascribed to the crossing between the spectra of olivine and pyroxene suggested in Fig. 2-7a.

[Insert Figure 2-5 here]

[Insert Figure 2-6 here]

[Insert Figure 2-7 here]

5.4. TSI for PS, SMFe and All the Minerals

5.4.1. TSI Curves for PS and SMFe

Shown in Fig. 2-8 are the log transformed TSI values for all the input factors including PS, SMFe, and abundance of plagioclase, pyroxene and olivine. It can be seen that the

simulated reflectance is highly sensitive to PS and SMFe at all wavelengths. In contrast, the abundance of minerals merely accounts for a small portion of the variation of the output reflectance. The significant effect of PS at all wavelengths is expected because the variation of PS strongly affects the amount of light that is scattered out of the materials and thus the overall magnitude of reflectance, which contributes mostly to the variation of a spectrum (*Pieters*, 1983; *Hapke*, 2005). Compared with other spectral regions, PS shows the largest influence around 1000 nm and 2000 nm. One reason might be that these two regions are absorption wavelengths of mafic minerals. Variation in PS greatly changes the mean optical path length of light travelling in the particle and affects the amount of light absorbed at these wavelength regions, resulting in evident changes in absorption band depth (*Pieters*, 1983). This strong effect of varying PS on absorption depth is also manifested by the investigation of *David et al*. (2013) who found that when attempting to derive *k* spectrum of mineral using Hapke's RTM, the resulting absorption strength can vary up to an order of magnitude due to different PS selected as input into Hapke's RTM.

The sensitivity of simulated reflectance to SMFe is not as high as that to PS, SMFe contributes more to the modeled reflectance than the abundance of mineral because SMFe is a strong absorber of light. Compared to the primary minerals of lunar soils, the absorption coefficients of SMFe are several factors larger than those of minerals. Shown in Fig. 2-4 are the computed absorption coefficients for both SMFe and olivine, indicating that the absorption coefficient of SMFe is much larger than that of olivine. Therefore, a small variation in the mass fraction of SMFe in lunar soils could result in a significant change in the reflectance of lunar soils. In contrast, a large variation in mineral abundance is required to induce similar variation in the reflectance of lunar soils.

The sensitivity of simulated reflectance to SMFe decreases apparently around 1000 nm and 2000 nm, which can be explained by two reasons. First, these two spectral regions are greatly affected by the mineral absorption, and the abundance of minerals contributes more spectral variation in these two regions, which ultimately weakens the influence of SMFe. Second, as stated by *Adams and Ralph* (1978) and *Fischer and Pieters* (1994), the absorption band depth becomes constant once lunar soils reach a mature state. When samples are highly mature, the effect of SMFe on absorption depth is saturated and the variation of SMFe may no longer affect spectral absorption.

5.4.2. TSI Curve for Plagioclase

The TSI curve for plagioclase (Fig. 2-8) is relatively flat across almost the whole spectral region due to low spectral contrast of plagioclase. However, two peaks around 1000 nm and 2000 nm could be observed. This might be attributed to the interference from pyroxene. It can be seen from Fig. 2-5b that plagioclase and pyroxene exhibit evident spectral interaction around 1000 nm and 2000 nm. Although the TSI value of plagioclase is not comparable to that of PS and SMFe, it is still much higher than that of the abundances of pyroxene and olivine due to its strong influence on the magnitude of reflectance. *Serventi et al*. (2012) examined spectra of plagioclase mixed with olivine and pyroxene, and found that changing the abundance of plagioclase in the mixtures can cause an increase in reflectance up to 50%.

5.4.3. TSI Curve for Olivine

The variation in olivine abundance accounts for a very small portion of the simulated reflectance with only a flat peak value between 1200 nm and 1400 nm. Because the strongest absorption band of olivine centers around 1050 nm, the simulated reflectance

should be most sensitive to the variation of olivine abundance at this wavelength rather than between 1200 nm and 1400 nm. This observation can be explained by three reasons. First, strong spectral interaction between olivine and pyroxene around 1050 nm and 850 nm as shown in Fig. 2-7b could mask out the absorptions of olivine at the two wavelengths. *Adams* (1974) examined the diffuse reflectance spectra of mixtures of pyroxene and olivine and observed that even when the content of olivine is up to 50%, its absorption feature still cannot be detected. The interaction between olivine and pyroxene may contribute more to the TSI value of pyroxene than to that of olivine and results in the relative low TSI value for olivine around 1050 nm. Second, due to the strong spectral interaction between plagioclase and olivine from 1100 nm to 1400 nm as shown in Fig. 2-6b, the 1300 nm absorption of plagioclase is overwhelmed by the absorption of olivine and thus the simulated reflectance is more sensitive to olivine in the 1200 nm - 1400 nm region than the 850 nm - 1050 nm region (*Isaacson et al*., 2011). This is consistent with the observation made by *Serventi et al*. (2013), which revealed that olivine can be detected even with its content being as low as 3% when mixed with plagioclase. In addition, as shown in Fig. 2-7b, pyroxene exhibits no significant interaction with olivine in the 1200 nm - 1400 nm region, and thus cannot affect the absorption of olivine. Third, very Fe-rich olivine tends to exhibit stronger long-wavelength (M1-2) absorption at wavelengths longer than 1250 nm (*Sunshine and Pieters*, 1998), which makes the olivine contribute more to the variation of simulated reflectance between 1200 nm and 1400 nm.

5.4.4. TSI Curve for Pyroxene

The TSI curve for pyroxene bears resemblance to its absorption spectrum and shows relatively higher value around 1000 nm and 2000 nm due to strong Fe^{2+} absorption of

pyroxene (*Adams*, 1974; *Burns*, 1993). The TSI curves of PS and SMFe in Fig. 2-8 are mostly similar to that of pure pyroxene (Fig. 2-3c), which suggests that pyroxene play an important role in regulating the absorption feature of simulated reflectance compared with other minerals. *Adams and McCord* (1972) and *Adams* (1974) compared the spectra of powdered lunar basalts with the spectra of mineral separates from the same rock, and indicated the significance of the pyroxene in defining the overall rock powder absorption feature. An overestimate of enstatite and an underestimate of anorthite for a mixture by *Mustard and Pieters* (1989) using Hapke's RTM also indicate significant contribution of pyroxene to the reflectance spectra. *Cheek and Pieters* (2012) and *Serventi et al*. (2013) investigated a mixture of pyroxene and plagioclase, and observed that the 1 μm pyroxene absorption band is still discernible even at 2% pyroxene. Moreover, *Yamada et al*. (1999), *Hiroi and Sasaki* (2001), and *Sasaki et al*. (2002) applied laser-irradiation on olivine and pyroxene samples to simulate the effects of space weathering. Results show that olivine was weathered more rapidly than pyroxene. This may suggest that when there is a small amount of SMFe in lunar soils, the absorption feature of olivine can be subdued dramatically and what left is the absorption feature mainly dominated by pyroxene. Therefore, the reflectance spectra show a high sensitivity to the abundance of pyroxene at absorption wavelengths than that of other minerals.

[Insert Figure 2-8 here]

6. Implications of TSI Values for Application of Hapke's RTM

6.1. Estimating Mass Fraction of SMFe in Lunar Soils

Results from SA of Hapke's RTM suggest that the variation in the mass fraction of SMFe in lunar soils has great impacts across the whole spectral range and SMFe is the

most important factor that drives the variation of the lunar soil reflectance (Fig. 2-8). This creates challenges for deriving mineral abundance and mass fractions of SMFe simultaneously from measured reflectance spectra. It is necessary to develop a strategy to address this challenge. Specifically, a simple empirical approach to estimating the mass fraction of SMFe in the lunar soils can be developed first, and then the derived SMFe can be input into Hapke's RTM to minimize the effect of SMFe and to improve the estimation accuracy of mineral abundance from measured reflectance spectra of lunar soils. For example, the mass fraction of SMFe can be estimated using the ratio of 540 nm/810 nm for single scattering albedo spectra (*Liu and Li*, 2015).

6.2. Estimating PS of Lunar Soils

Variation of PS also exhibits a significant influence on the reflectance spectra of lunar soils and interferes with spectral estimation of mineral abundance using Hapke's RTM (Fig. 2-8). Prior knowledge on the PS of lunar soils is required for accurate prediction on the mineral abundance of lunar soils via Hapke's RTM, which can be determined through thermal inertia data obtained from Lunar Reconnaissance Orbiter (*Gundlach and Blum*, 2013). Alternatively, some empirical models can be designed to eliminate first the effects of PS on the spectral estimation of mineral abundance. For example, *Clouts et al*. (1986) found the ratio of areas for 1 μm and 2 μm absorption bands is highly sensitive to the mineral abundances of olivine and orthopyroxene while insensitive to the variation of PS, suggesting that the ratio could be used to eliminate PS effects effectively.

6.3. Implications for Estimating Mineral Abundance of Lunar Soils

Reflectance spectra are sensitive to plagioclase abundance across the whole wavelength region because of the strong effects of plagioclase in regulating the magnitude

of reflectance of lunar soils. This can explain the high prediction accuracy of plagioclase abundance than other minerals from measured reflectance using Hapke's RTM in previous studies (*Li and Li*, 2011; *Liu et al*., 2015). The whole spectral wavelengths should be considered in future applications of Hapek's RTM for deriving the abundance of plagioclase.

Olivine possesses the strongest absorption band around 1050 nm (M2 site), and Hapke's RTM should be more sensitive to the variation of olivine at this wavelength. However, it can be seen that olivine contributes most to the simulated reflectance between 1200 nm and 1400 nm (Fig. 2-8). Although the 1050 nm absorption of olivine is masked out due to strong interaction with the 1000 nm absorption of pyroxene (Fig. 2-7), there is no spectral overlapping for 1250 nm olivine absorption (M1-2 site) with pyroxene absorption features and thus the longer wavelength absorption feature of olivine (1250 nm M1-2 site) can be retained and detected. Spectral measurement on the mixture of olivine and pyroxene has demonstrated that the diagnostic absorption feature of olivine around 1250 nm is still detectable even for a small amount of olivine in the mixture and the most useful indication of olivine abundance in an olivine-bearing mixture is the shallow depression centered around 1250 nm of the mixture spectra (*Singer*, 1981). Although olivine and plagioclase also have a strong interaction between 1100 nm and 1400 nm due to overlapping of olivine 1250 nm (M1-2 site) absorption with plagioclase 1300 nm absorption, the 1300 nm absorption of plagioclase could be overwhelmed by 1250 nm absorption of olivine. *Cheek and Pieters* (2014) found that the plagioclase absorption band is easily masked in mixtures containing small proportion of olivine resulting in the spectral feature between 1100 nm and 1400 nm mainly dominated by 1250 nm absorption of olivine.

Future applications of Hapke's RTM in estimating abundances of olivine should be focused on the wavelength range between 1200 nm and 1400 nm rather than 1050 nm.

Results from SA of Hapke's RTM showed that pyroxene dominates absorption features of simulated reflectance. This might be due to the higher extinction coefficients of pyroxene than other minerals in the mixture (*Singer*, 1981; *Clout et al*., 1986). The dominant effect of pyroxene in regulating absorption features of mineral mixture spectra is also supported by a number of studies (*Adams and McCord*, 1972; *Adams*, 1974; *Nash and Conel*, 1974; *Burn*, 1989). Through investigating the absorption features of lunar samples, *Adams* (1974) found that 1 μm versus 2 μm absorption of lunar samples lie on the trend line defined by 1 μm versus 2 μm absorption of pure terrestrial pyroxene and concluded that pyroxene always dominates the reflectance spectra of lunar soils. In addition, *Nobel et al*. (2006) compared the spectral properties of LSCC soil samples with their petrologic and chemical compositions using modified Gaussian model (MGM) and found that a strong correlation exists between the total pyroxene abundance and strength of four MGM decomposed bands representing 1 μm and 2 μm absorptions of clinopyroxene and orthopyroxene in lunar soils. Our results from SA of Hapke's RTM are consistent with these investigations and demonstrated the dominant effects of pyroxene in defining 1 μm and 2 μm absorptions of reflectance spectra. Therefore, 1 μm and 2 μm wavelength regions rather than the whole spectral wavelength regions should be selected in Hapke's RTM to improve the estimation accuracy of pyroxene abundance in future work.

7. Conclusions

Application of EFAST to the Hapke's RTM simulated reflectance spectra shows that PS and SMFe have the strongest impact across the whole wavelength region and they are

the two most important factors that drive the variance of lunar soil reflectance. The contribution of mineral abundance to the reflectance is much less significant than that of PS and SMFe and could be suppressed by PS and SMFe. This creates a challenge for deriving lunar mineral abundance from remotely sensed data.

Absorption feature of lunar soil reflectance spectra is mainly dominated by pyroxene and a strong spectral interaction occurs for pyroxene and olivine around 1000 nm resulting in the 1050 nm absorption of olivine being overwhelmed by that of pyroxene close to 1000 nm. A spectral interaction between plagioclase and olivine can be also observed from 1200 nm to 1400 nm.

When Hapke's RTM is applied to derive the abundance of minerals in lunar soils, the estimation accuracy could be potentially improved by choosing specific spectral regions where minerals contribute more to the variation of reflectance. 1000 nm and 2000 nm could be used to derive abundance of pyroxene and the best wavelength regions to estimate abundance of olivine is between 1200 nm and 1400 nm rather than 1050 nm as generally assumed.

At the current state, the sensitivity of Hapke's RTM was only analyzed for PS, abundance of minerals, and mass fraction of SMFe. However, the variation of chemical composition of lunar soils was not taken into account which also greatly affects the reflectance spectra. Changing relative content of FeO, MgO and CaO in a lunar soil could result in differing refractive index (*n* and *k*) and thus affect the surface reflection, absorption band position and depth of reflectance spectra (*Lucey*, 1998; *Wilcox et al.*, 2006; *Denevi et al*., 2007). The importance of chemical composition of lunar soils in regulating reflectance spectra should be quantified in future SA.

Appendix: Hapke's Radiative Transfer Model

Hapke's RTM computes the bidirectional reflectance of a surface using the following equation:

$$R = \frac{\omega_{ave}}{4\pi}\frac{\mu_0}{\mu_0+\mu}\{[1 + B(g)]P(g) + H(\mu_0, \omega_{ave})H(\mu, \omega_{ave}) - 1\}, \quad (1)$$

where *R* is the bidirectional reflectance, ω_{ave} is the average SSA of all the components in the medium. μ_0 and μ are the cosine of the incidence angle and emittance angle, which were set as 30^0 and 0^0 respectively. g is the phase angle (equal to 30^0). *P(g)* is the phase function describing the angular pattern into which the incident power is scattered. A two-term legendre polynomial as following was used:

$$P(g) = 1 + b\,cos\,g + c\left(\frac{3}{2}cos^2 g - \frac{1}{2}\right), \quad (2)$$

where b and c are often set to be -0.4 and 0.25, respectively, as suggested by *Lucey* (1998). *B(g)* is the backscattering function describing the opposition effects. Because the phase angle was set as 30^0 greater than 15^0, the effect of backscattering was ignored in this work (*Mustard and Pieters*, 1989). H is the isotropic scattering function and can be approximated by:

$$H(x) = \{1 - [1 - \gamma]x\left[r_0 + \left(1 - \frac{1}{2}r_0 - r_0 x\right)ln\left(\frac{1+x}{x}\right)\right]\}^{-1}, \quad (3)$$

where x represents either μ_0 or μ, $\gamma = (1 - \omega_{ave})^{1/2}$ and $r_0 = \frac{1-\gamma}{1+\gamma}$.

ω_{ave} is a linear combination of SSA of end-member components weighted by their mass fraction and can be described as:

$$\omega_{ave} = \sum_i \frac{M_i\omega_i}{\rho_i d_i} / \sum_i \frac{M_i}{\rho_i d_i}. \quad (4)$$

i represents the i^{th} component. M_i is the mineral abundance. ω_i, ρ_i and d_i are the SSA, density and mean PS of the i^{th} component.

SSA of an end-member component (ω_i) can be calculated using following equations:

$$\omega = S_e + (1 - S_e)\frac{(1-S_i)\Theta}{1-S_i\Theta}, \quad (5)$$

$$S_e = \frac{(n-1)^2+k^2}{(n+1)^2+k^2} + 0.05, \quad (6)$$

$$S_i = 1 - \frac{4}{n(n+1)^2}, \quad (7)$$

$$\Theta = e^{-\alpha<D>}, \quad (8)$$

$$< D > = \frac{2}{3}[n^2 - \frac{1}{n}(n^2-1)^{\frac{3}{2}}]D. \quad (9)$$

Here, S_e is the external surface scattering coefficient for Fresnel reflection, S_i is the internal surface scattering coefficient and Θ is the internal-transmission factor. $< D >$ is the mean path length of light in the particle, a function of end-member PS that can be evaluated by Eq. 5.41 in *Hapke* (2005). α is the absorption coefficient of end-member component. *Hapke* (2001) incorporated space weathering effects into the calculation of absorption coefficient α of end-member component defined as below:

$$\alpha = \frac{4\pi n_h k_h}{\lambda} + \frac{36\pi z M_c \rho_h}{\lambda \rho_{Fe}}, \quad (10)$$

where

$$z = \frac{n_h^3 n_{Fe} k_{Fe}}{(n_{Fe}^2 - {k_{Fe}}^2 + 2n_h^2)^2 + (2n_{Fe}k_{Fe})^2}. \quad (11)$$

Here, *n* and *k* are real and imaginary parts of the refractive index and ρ is solid density. These three parameters are indicated with appreciate suffixes, wherein h and Fe indicate host mineral and SMFe, respectively. M_c is the mass fraction of SMFe coating on the surface of a particle, λ is the wavelength. In this work, the refractive index for plagioclase, olivine and pyroxene were set the same as that used in the study of *Li and Li* (2011) and refractive index for SMFe was from *Johnson and Christy* (1974).

Acknowledgements

We gratefully acknowledge the suggestion and support of Jia Du. We also appreciates discussion with Ying Sun in the preparation of manuscript.

Table Captions

Table 2-1. Different mineral parameters used for simulating reflectance spectra

Table 2-1

Group	Selected factors as input variables	Fixed factors	Variation range
I	PS + SMFe	plagioclase: 100%, olivine: 0%, pyroxene: 0%	PS: 1-45 μm, SMFe: 0-1%
II	PS + SMFe	olivine: 100%, plagioclase: 0%, pyroxene: 0%	PS: 1-45 μm, SMFe: 0-1%
III	PS + SMFe	pyroxene: 100%, plagioclase: 0%, olivine: 0%	PS: 1-45 μm, SMFe: 0-1%
IV	plagioclase + pyroxene	PS: 15 μm, SMFe: 0.2%, olivine: 0%	plagioclase: 0-100%, pyroxene: 0-100%
V	plagioclase + olivine	PS: 15 μm, SMFe: 0.2%, pyroxene: 0%	plagioclase: 0-100%, olivine: 0-100%
VI	olivine + pyroxene	PS: 15 μm, SMFe: 0.2%, plagioclase: 0%	olivine: 0-100%, pyroxene: 0-100%
VII	PS, SMFe, plagioclase, pyroxene, olivine	--	PS: 1-45 μm, SMFe: 0-1%, plagioclase: 0-100%, pyroxene: 0-100%, olivine: 0-100%

Figure Captions

Figure 2-1. Flowchart of sensitivity analysis.

Figure 2-2. Subset of simulated reflectance spectra when all the input factors (PS, SMFe and abundance of minerals) are allowed to vary in Hapke's RTM.

Figure 2-3. TSI values for PS and SMFe considering 100% plagioclase, 100% olivine, 100% pyroxene, respectively.

Figure 2-4. Absorption coefficients of SMFe and olivine. The refractive index (*n* and *k*) used to calculate absorption coefficient of SMFe and olivine are from *Johnson and Christy* (1974) and *Li and Li* (2011).

Figure 2-5. (a) Simulated reflectance spectra of group IV with different abundance of plagioclase and pyroxene. (b) Interaction between plagioclase and pyroxene based on TSI-SI values.

Figure 2-6. (a) Simulated reflectance of group V with different abundance of olivine and plagioclase. (b) Interaction between olivine and plagioclase based on TSI-SI.

Figure 2-7. (a) Simulated reflectance of group VI with different abundance of olivine and pyroxene. (b) Interaction between olivine and pyroxene based on TSI-SI.

Figure 2-8. Log scale of TSI value for all input factors.

Figures

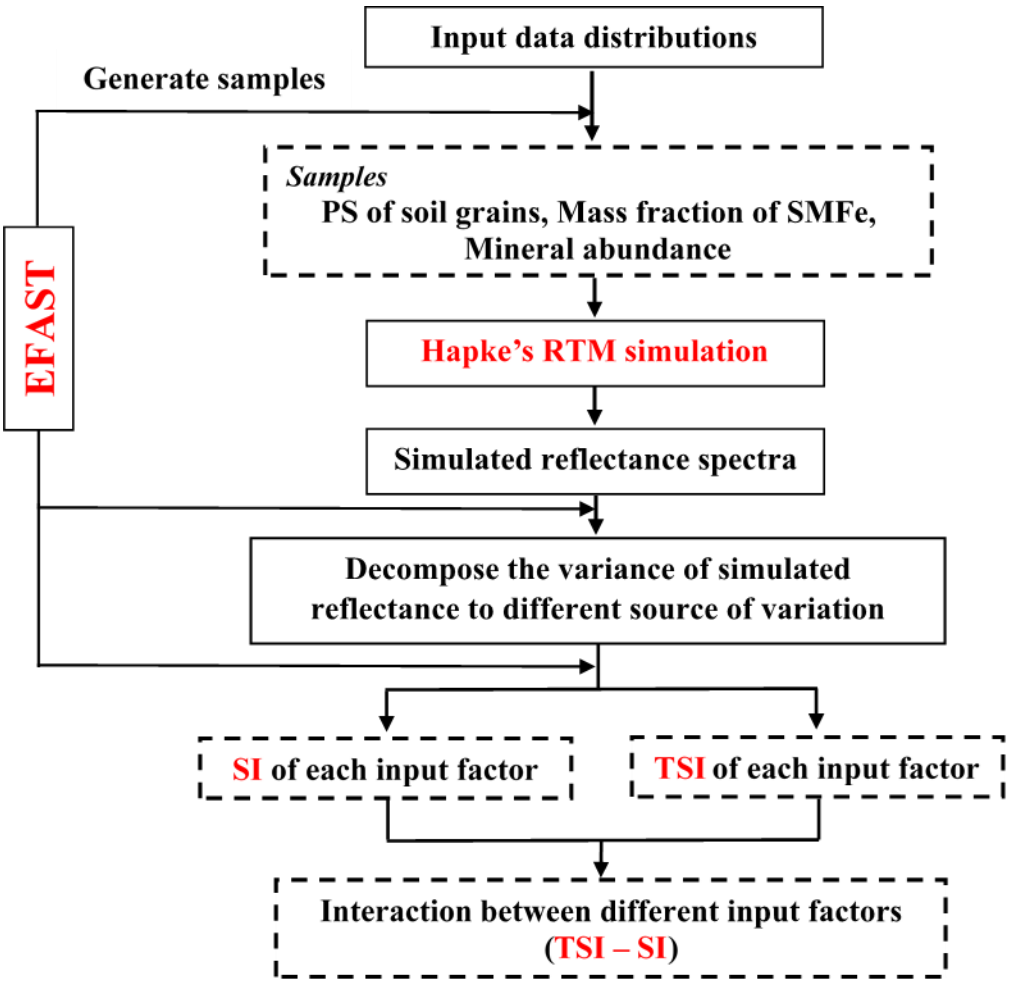

Figure 2-1

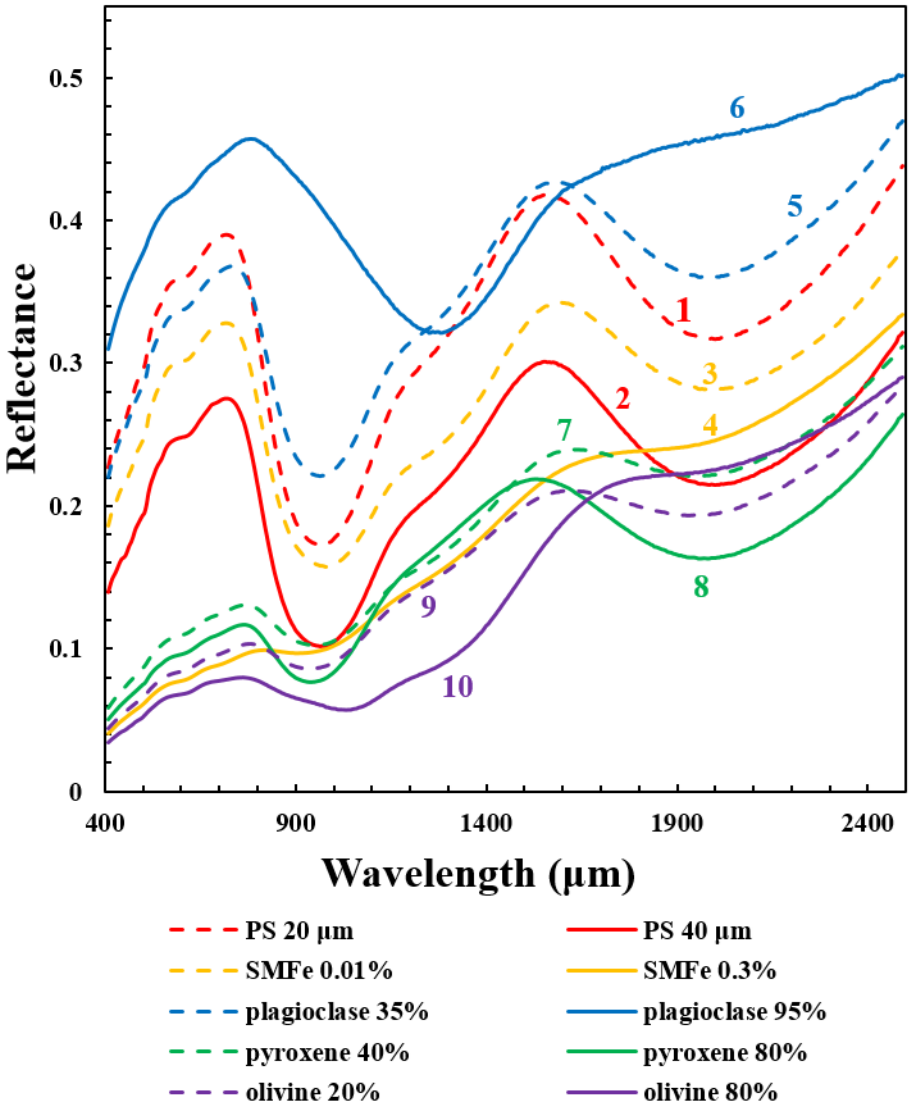
Reflectance
0.5
0.4
0.3
0.2
0.1
0
400
900
1400
1900
2400
Wavelength (µm)
6
5
1
3
2
4
7
8
9
10
PS 20 µm
PS 40 µm
SMFe 0.01%
SMFe 0.3%
plagioclase 35%
plagioclase 95%
pyroxene 40%
pyroxene 80%
olivine 20%
olivine 80%

Figure 2-2

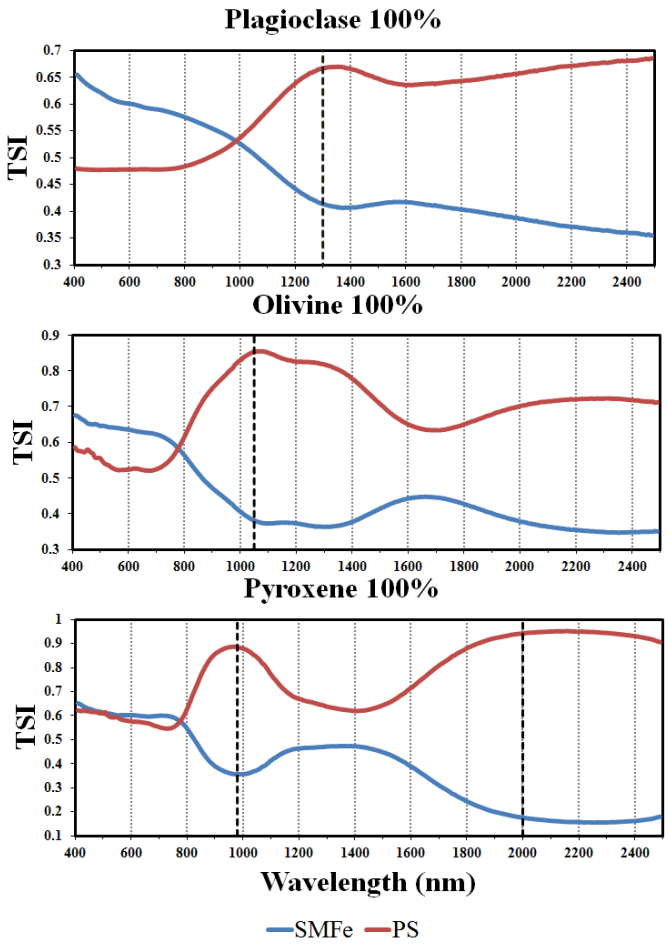
Plagioclase 100%
TSI
Olivine 100%
TSI
Pyroxene 100%
TSI
Wavelength (nm)
SMFe
PS

Figure 2-3

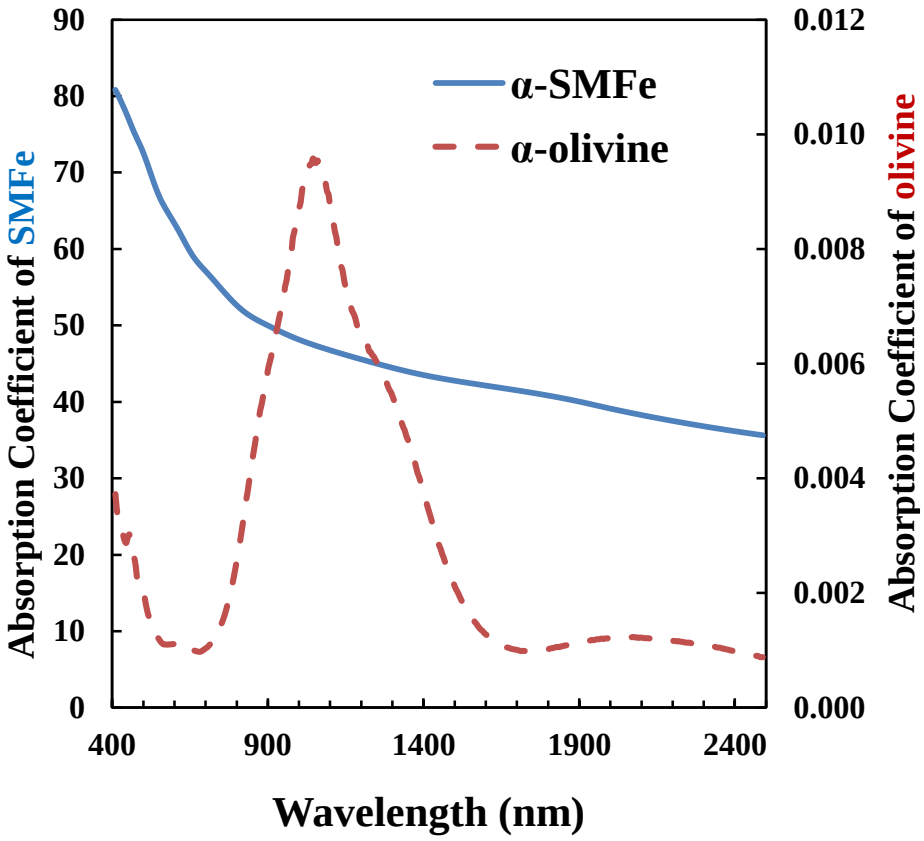
α-SMFe
α-olivine
Absorption Coefficient of SMFe
Absorption Coefficient of olivine
Wavelength (nm)
90
80
70
60
50
40
30
20
10
0
0.012
0.010
0.008
0.006
0.004
0.002
0.000
400
900
1400
1900
2400

Figure 2-4

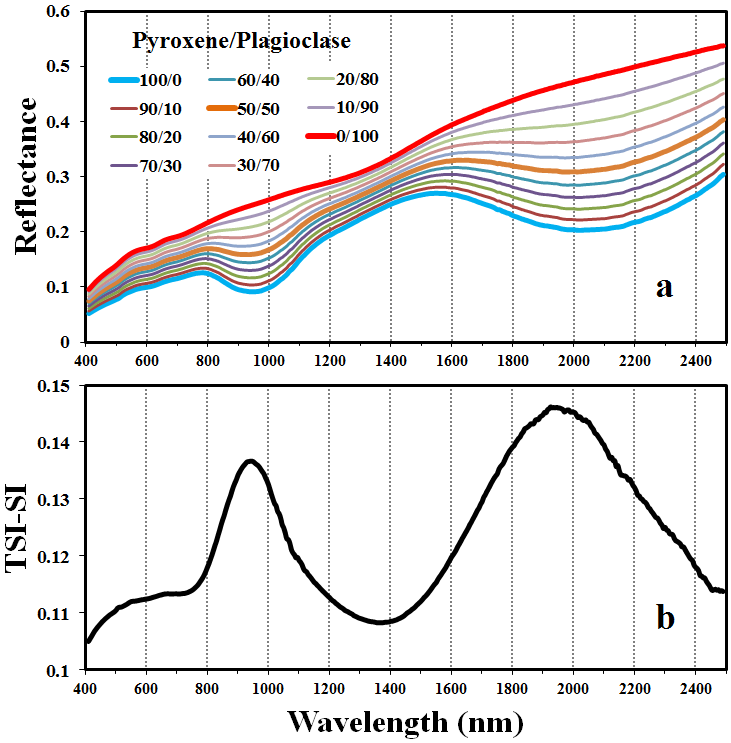
Pyroxene/Plagioclase
100/0
90/10
80/20
70/30
60/40
50/50
40/60
30/70
20/80
10/90
0/100
Reflectance
a
TSI-SI
b
Wavelength (nm)

Figure 2-5

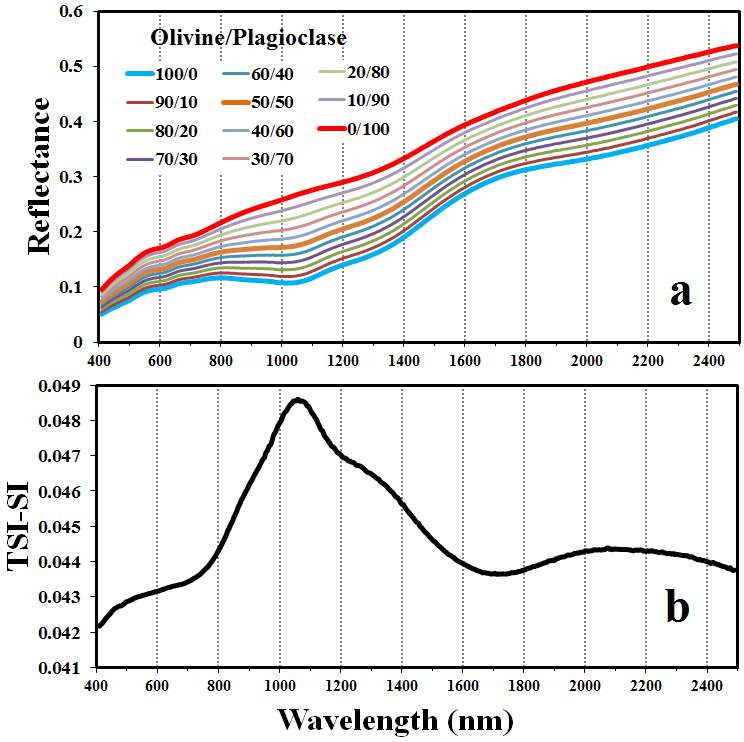
Olivine/Plagioclase
100/0
90/10
80/20
70/30
60/40
50/50
40/60
30/70
20/80
10/90
0/100
Reflectance
a
TSI-SI
b
Wavelength (nm)

Figure 2-6

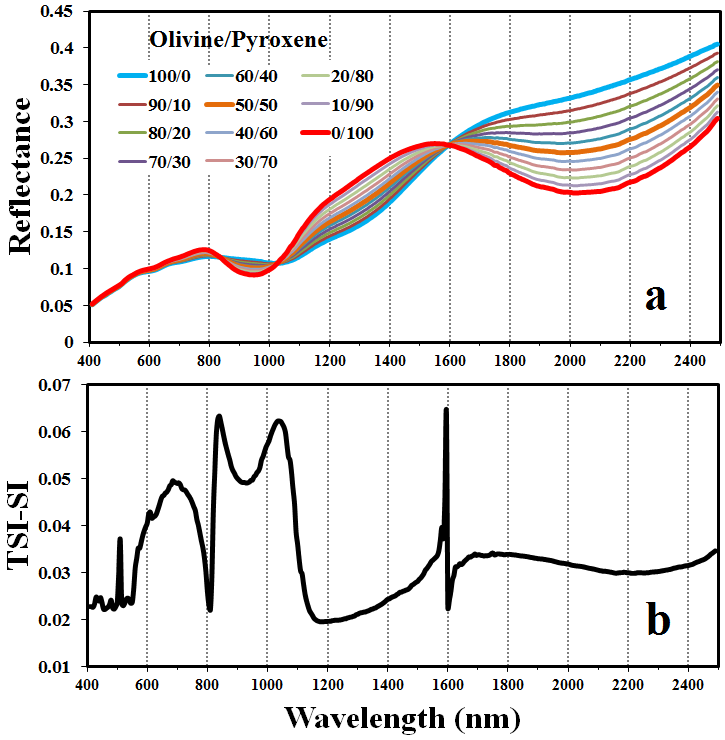
Olivine/Pyroxene
100/0
90/10
80/20
70/30
60/40
50/50
40/60
30/70
20/80
10/90
0/100
Reflectance
a
TSI-SI
b
Wavelength (nm)

Figure 2-7

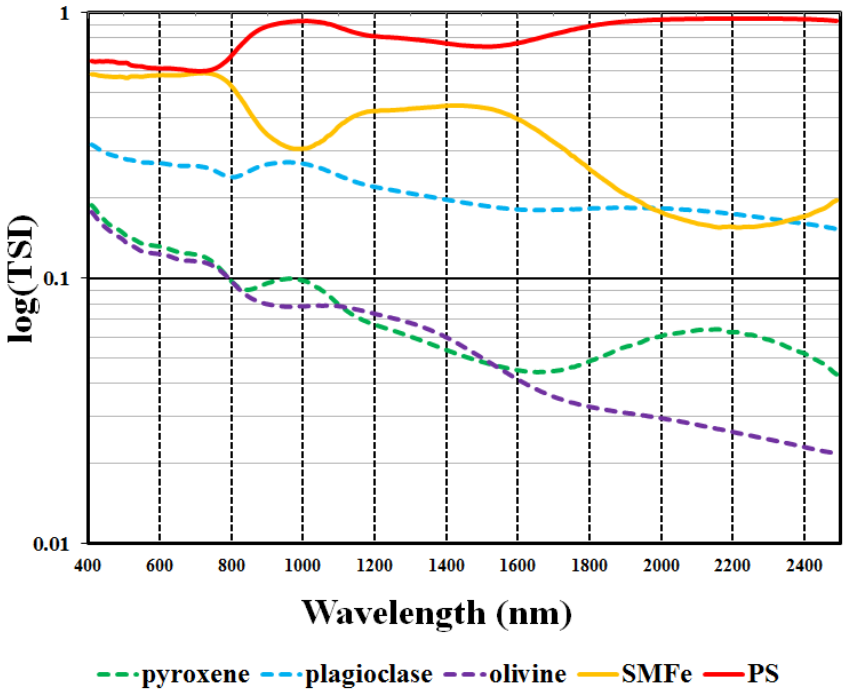
1
0.1
0.01
log(TSI)
400
600
800
1000
1200
1400
1600
1800
2000
2200
2400
Wavelength (nm)
pyroxene
plagioclase
olivine
SMFe
PS

Figure 2-8

References

Adams, J. B., and A. L. Filice (1967), Spectral reflectance 0.4 to 2.0 microns of silicate rock powders, *J. Geophys. Res.* 72, 5705-5715.

Adams, J. B., and T. B. McCord (1970), Remote sensing of lunar surface mineralogy: Implications from visible and near-infrared reflectivity of Apollo 11 samples, *Proc. Apollo 11 Lunar Sci. Conf.* 3, 1937-1945.

Adams, J. B., and T. B. McCord (1972), Electronic spectra of pyroxenes and interpretation of telescopic spectral reflectivity curves of the moon, *Proc. Lunar Sci. Conf.* 3, 3021-3034.

Adams, J. B. (1974), Visible and near-infrared diffuse reflectance spectra of pyroxene as applied to remote sensing of solid objects in the solar system, *J. Geophys. Res.* 79, 4829-4836.

Adams, J. B. (1975), Interpretation of visible and near-infrared diffuse reflectance spectra of pyroxenes and other rock forming minerals, *Infrared and Raman Spectroscopy of lunar and Terrestrial Materials*, New York.

Adams, J. B., and R. L. Ralph (1978), Diffuse reflectance spectra of Luna 24 soils. *In Mare Crisium: The view from luna 24*, 81-87.

Burns, R. G. (1970), Crystal field spectra and evidence of cation ordering in olivine minerals. *Am. Mineral*. 55, 1608–1632.

Burns, R. G. (1989), Spectral mineralogy of terrestrial planets - Scanning their surfaces remotely, *Mineral. Mag.* 53, 135-151.

Burns, R. G. (1993), Mineralogical Applications of Crystal Field Theory, Cambridge University Press, New York.

Ceccato, P., N. Gobron, S. Flasse, B. Pinty, and S. Tarantola (2002), Desiging a spectral index to estimate vegetation water content from remote sening data: Part 1: Theoretical approach, *Remote Sens. Environ.* 82, 188-197.

Cheek, L. C., and C. M. Pieters (2012), Variations in anorthosite purity at Tsiolkovsky crater on the moon, *Lunar Planet. Sci. Conf.* 43, 2624.

Cheek, L. C., and C. M. Pieters (2014), Reflectance spectroscopy of plagioclase-dominated mineral mixtures: Implications for characterizing lunar anorthosites remotely, *Am. Mineral.* 99, 1871-1892.

Charette, M. P., T. B. McCord, C. M. Pieters, and J. B. Adams (1974), Application of remote spectral reflectance measurements to lunar geology classification and determination of titanium content of lunar soils, *J. Geophys. Res. – Solid Earth* 79, 1605-1613.

Clark, R. N., and T. L. Roush (1984), Reflectance spectroscopy: quantitative analysis techniques for remote sensing applications, *J. Geophys. Res. – Solid Earth* 89, 6329-6340.

Clouts, E. A., M. J. Gaffey, T. L. Jackowski, and K. L. Reed (1986), Calibrations of phase abundance, compostion, and particle size distribution for olivine-orthopyroxnene mixtures from reflecatnce spectra, *J. Geophyis. Res. – Solid Earth* 91, 11641-11653.

Cukier, R. I., H. B. levine, and K. E. Shuler (1978), Nonlinear sensitivity anallysis of multiparameter model systems, *J. Comput. Phys.* 26, 1-42.

David, T., P. G. Lucey, J. J. Gillis-Davis, J. T. S. Cahill, R. L. Klima, and P. J. Isaacson (2013), Near-infrared optical constants of naturally occurring olivine and synthetic pyroxene as a function of mineral composition, *J. Geophys. Res. Planets* 118, 708-732.

Denevi, B. W., P. G. Lucey, E. J. Hochberg, and D. Steutel (2007), Near-infrared optical constants of pyroxene as a function of iron and calcium content, *J. Geophys. Res. - Planets* 112, E05009.

Denevi, B. W., P. G. Lucey, and S. B. Sherman (2008), Radiative transfer modeling of near-infrared spectra of lunar mare soils: Theory and measurement, *J. Geophys. Res. Planets* 113, E02003.

Ekström, P. A. (2005), A simulation toolbox for Sensitivity Analysis, Masters Degree Project.

Fischer, E. M., and C. M. Pieters (1994), Remote determination of exposure degree and iron concentration of lunar soils using VIS-NIR spectroscopic methods, *Icarus* 111, 475-488.

Gundlach, B., and J. Blum (2013), A new method to determine the grain size of planetary regolith. *Icarus* 223, 479-492.

Hapke, B. (1981), Bidirectional reflectance spectroscopy: I. Theory, *J. Geophys. Res. - Solid Earth* 86, 3039-3054.

Hapke, B., and E. Wells (1981), Bidirectional reflectance spectroscopy 2. Experiments and Observations, *J. Geophys. Res. - Solid Earth* 86, B4, 3055-3060.

Hapke, B. (2001), Space weathering from Mercury to the asteroid belt, *J. Geophys. Res. - Planets* 106, 10039-10073.

Hapke, B. (2005), Theory of reflectance and emittance spectroscopy, Cambridge University Press, Cambridge, New York.

Hiesinger, H., and J. W. Head (2006), New views of lunar geoscience: An introduction and overview, *Rev. Mineral. Geochem*. 60.

Hiroi, T., and C. M. Pieters (1992), Effects of grain size and shape in modeling reflectance spectra of mineral mixture, *Proc. Lunar Planet. Sci.* 22, 313-325.

Hiroi, T., and S. Sasaki (2001), Importance of space weathering simulation products in compositional modeling of asteroids: 349 Dembowska and 446 Aeternitas as examples, *Meteorit. Planet. Sci.* 36, 1587-1596.

Isaacson, P. J., and C. M. Pieters (2010), Deconvolution of lunar olivine reflectance spectra: Implications for remote compositional assessment, *Icarus* 210, 8–13.

Isaacson et al. (2011), Remote compositional analysis of lunar olivine-rich lithologies with Moon Mineralogy Mapper (M^3) spectra, *J. Geophys. Res. - Planets* 116, E00G11.

James, C. L., S. L. Letsinger, A. Basu, S. J. Wentworth, and D. S. McKay (2002), Size Distribution of Fe^0 Globules in Lunar Agglutinitic Glass, paper presented at Lunar and Planetary Science Conference.

Jolliff, B. L., J. J. Gillis, L. A. Haskin, R. L. Korotev, and M. A. Wieczorek (2000), Major lunar crustal terranes: Surface expressions and crust-mantle origins, *J. Geophys. Res. - Planets* 105, 4197-4216.

Johnson, P. E., M. O. Smith, and J. B. Adams (1992), Simple algorithms for remote determination of mineral abundances and particle sizes from reflectance spectra, *J. Geophys. Res. - Planets* 97, 2649-2657.

Johnson, P. B., and R. W. Christy (1974), Optical constants of transition metals: Ti, V, Cr, Mn, Fe, Co, Ni, and Pd, *Phys. Rev.* 9, 5056-5070.

Keller, L. P., and D. S. Mckay (1993), Discovery of vapor deposits in the lunar regolith, *Science* 261, 1305-1307.

Keller, L. P., and D. S. McKay (1997), The nature and origin of rims on lunar soil grains, *Geochim. Cosmochim. Ac.* 61, 2331-2341.

Keller, L. P., S. J. Wentworth, D. S. McKay, L. A. Taylor, C. M. Pieters, and R. V. Morris (2000), Space weathering in the fine size frations of lunar soils: mare/highland differences, *Lunar Planet. Sci. 56*, 1655.

Keller, L. P., and S. J. Clemett (2001), Formation of nanophase iron in the lunar regolith, *Lunar Planet. Sci.* 57, 2097.

Li, S., and L. Li (2011), Radiative transfer modeling for quantifying lunar surface minerals, particle size and submicroscopic metallic Fe. *J. Geophys. Res. - Planets* 116, E09001.

Liu, D., and L. Li, (2015). An empirical approach to estimating mass fraction of submicroscopic iron in lunar soils. *Lunar Planet. Sci*. 46, 2560.

Liu, D., L. Li, and Y. Sun (2015), An improved radiative transfer model for estimating mineral abundance of immture and mature lunar soils, *Icarus* 253, 40-50.

Lucey, P. G. (1998), Model near-infrared optical constants of olivine and pyroxene as a function of iron content, *J. Geophys. Res. - Planets* 103, 1703-1713 .

Lucey, P. G., D. T. Blewett, and B. R. Hawke (1998), Mapping the FeO and TiO_2 content of the lunar surface with multispectral imagery, *J. Geophys. Res. - Planets* 103, 3679-3699.

Lucey, P. G., and S. K. Noble (2008), Experimental test of a radiative transfer model of the optical effects of space weathering, *Icarus* 197, 348-353.

Lucey, P. G, and M. A. Riner (2011), The optical effects of small iron particles that darken but do not redden: evidence of intense space weathering on Mercury, *Icarus* 212, 451-462.

McCord, T. B., and J. B. Adams (1973), Progress in remote optical analysis of lunar surface composition, *The Moon* 7, 453-474.

McCord, T. B., R. N. Clark, B. R. Hawke, L. A. McFadden, P. D. Owensby, C. M. Pieters, and J. B. Adams (1981), Moon: near-infrared spectral reflectance, a first good look, *J. Geophys. Res. – Solid Earth* 86, 10883-10892.

Morris, R. V. (1976), Surface exposure indices of lunar rocks: A comparative FMR study, *Proc. Lunar Sci*. 7, 315 – 335.

Morris, R. V. (1977), Origin and evolution of the grain-size dependence of the concentration of fine-grained metal in lunar soils: The maturation of lunar soils to a steady-state stage, *Proc. Lunar Sci. Conf*. 8, 3719-3747.

Morris, R. V. (1980), Origins and size distribution of metallic iron particles in the lunar regolith, *Proc. Lunar Sci. Conf*. 11, 1697-1712.

Morris, M. D. (1991), Fractorial sampling plans for preliminary computational experiments, *Technometrics* 33, 161-174.

Mustard, J. F., and C. M. Pieters (1989), Photometric phase functions of common geologic minerals and applications to quantitative-analysis of mineral mixture reflectance spectra, *J. Geophys. Res. – Solid Earth* 94, 13619-13634.

Nash, D. B., and J. E. Conel (1974), Spectral reflectance systematics for mixtures of powered hyperthene, labradorite, and ilmenite, *J. Geophys. Res*. *– Solid Earth* 79, 16415-1621.

Noble, S. K., C. M. Pieters, L. A. Taylor, R. V. Morris, C. C. Allen, D. S. McKay, and L. P. Keller (2001), The optical properties of the finest fraction of lunar soil: Implications for space weathering, *Meteorit. Planet. Sci.* 36, 31-42.

Noble, S. K., C. M. Pieters, T. Hiroi, and L. A. Taylor (2006), Using the modified Gausssian model to extract quantitative data from lunar soils, *J. Geophys. Res. - Planets* 11, E11009.

Noble, S. K., C. M. Pieters, and L. P. Keller (2007), An experimental approach to understanding the optical effects of space weathering, *Icarus* 192, 629-642.

Ohtake, M., T. Matsunaga, J. Haruyama, and Y. Yokota (2009), The global distribution of pure anorthosite on the moon, *Nature* 461.

Pieters, C. M. (1983), Strength of mineral absorption features in the transmitted component of near-infrared reflected light: first results from RELAB, *J. Geophys. Res*. – Solid Earth 88, 9534-9544.

Pieters, C. M. (1986), Composition of the lunar highland crust from near-infrared spectroscopy, *Rev. Geophys.* 24, 557-578.

Pieters, C. M., E. M. Fischer, O. Rode, and A. Basu (1993), Optical effects of space weathering - the role of the finest fraction, *J. Geophys. Res. – Planets* 98, 20817-20824.

Pieters, C. M., L. A. Taylor, S. K. Noble, L. P. Keller, B. Hapke, R. V. Morris, C. C. Allen, D. S. McKay, and S. Wentworth (2000), Space weathering on airless bodies: Resolving a mystery with lunar samples, *Meteorit. Planet. Sci*. 35, 1101-1107.

Sasaki, S., K. Nakamura, Y. Hamabe, E. Kurahashi, and T. Hiroi (2001), Production of iron nanoparticles by laser irradiation in a simulation of lunar-like speca weathering, *Nature* 410, 555-557.

Sasaki, S., T. Hiroi, K. Nakamura, Y. Hamabe, E. Kurahashi, and M. Yamada (2002), Simulation of space weathering by nanosecond pulse laser heating: Dependence on

mineral composition, weathering trend of asteroids and discovery of nanophase iron particles, *Adv, Sp. Res*. 29, 783-788.

Saltelli, A., T. H. Andres, and T. Homma (1993), Sensitivity analysis of model putput: An investigation of new techniques, *Comput. Statistics Data Anal* 15, 211-238.

Saltelli, A., and I. M. Sobol (1995), About the use of rank transformation in sensitivity analysis of model output, *Reliab. Eng. Syst. Safe.* 50, 225-239.

Saltelli, A., S. Tarantola, and K. P.-S. Chan (1999). A quantitative model independent method for global sensitivity analysis of model output. *Technometrics* 41, 39-56.

Shkuratov, Y., L. Starukhina, H. Hoffmann, and G. Arnold (1999), A model of spectral albedo of particulate surface: Impilcaitions for optical properties of the moon, *Icarus* 137, 235-246.

Singer, R. B. (1981), Near-infrared spectral reflectance of mineral mixtures: systematic combinations of pyroxenes, olivine, and iron oxides, *J. Geophys. Res*. – *Solid Earth* 86, 7967-7982.

Sunshine, J. M., C. M. Pieters, and S. F. Pratt (1990), Deconvolution of mineral absorption bands: An improved approach, *J. Geophys. Res*. 95, 6955-6966.

Sunshine, J. M., and C. M. Pieters (1998), Determining the composition of olivine from reflectance specttapscopy, *J. Geophys. Res. – Planets* 103, 13675-13688.

Serventi, G., C. Carli, M. Sgavetti, and L. Pompilio (2012), Effects of plagioclase chemistry and modal abundance on spectral properties of multimineral Fe, Mg mixtures, *Lunar Planet. Sci. Conf.* 43, 1404.

Serventi, G., C. Carli, and M. Sgavetti (2013), Plagioclase influence in mixtures with very low mafic mineral content, *Lunar Planet. Sci. Conf.* 44, 1490.

Tompkins, S., and C. M. Pieters (1999), Mineralogy of the lunar crust: Results from Clementine, *Meteorit. Planet. Sci*. 34, 25-41.

Taylor, L. A., C. M. Pieters, L. P. Keller, R. V. Morris, and D. S. McKay (2001), Lunar mare soils: Space weathering and the major effects of surface-correlated nanophase Fe, *J. Geophys. Res. - Planets* 106, 27985-27999.

Taylor, L. A., C. M. Pieters, A. Patchen, D. S. Taylor, R. V. Morris, L. P. Keller, and D. S. Mckay (2010), Mineralogical and chemical characterization of lunar highland soils: Insights into the space weathering of soils on airless bodies, *J. Geophys. Res. – Planets* 115, E02002.

Warell, J., and B. J. R. Davidsson (2010), A Hapke's model implementation for compositional analysis of VNIR spectra of Mercury, *Icarus* 209, 164-178.

Wieczorek, M. A., and R. J. Phillips (2000), The "Procellarum KREEP Terrane": Implications for mare volcanism and lunar evolution, *J. Geophys. Res.* 105, 20417-20430.

Wood, J. A. (1975), Lunar petrogenesis in a well-stirred magma ocean, *Proc. Lunar Sci. Conf.* 6, *15*.

Wilcox, B. B., P. G. Lucey, and B. R. Hawke (2006), Radiative transfer modeling of compositions of lunar pyroclastic deposits, *J. Geophys. Res. - Planets* 111, E09001.

Yamamoto, S., et al. (2010), Possible mantle origin of olivine around lunar impact basins detected by SELENE, *Nat. Geosci* 3, 533-536.

Yamada, M., S. Sasaki, H. Nagahara, A. Fujiware, S. Hasegawa, H. Yano, T. Hiroi, H. Ohashi, and H. Otake (1999), simulation of space weathering of planet-forming

materials: Nanophase pulse laser irradiation and protion implantation on olivine and pyroxene samples, *Earth Planets Sp.* 51, 1255-1265.

CHAPTER 3

AN IMPROVED RADIATIVE TRANSFER MODEL FOR ESTIMATING MINERAL ABUNDANCE OF IMMATURE AND MATURE LUNAR SOILS

Abstract

An improved Hapke's radiative transfer model (RTM) is presented to estimate mineral abundance for both immature and mature lunar soils from the Lunar Soil Characterization Consortium (LSCC) dataset. Fundamental to this improved Hapke's model is the application of an alternative equation to describe the effects of larger size submicroscopic metallic iron (SMFe) (>50 nm) in the interior of agglutinitic glass that mainly darken the host material, contrasting to the darkening and reddening effects of smaller size SMFe (<50 nm) residing in the rims of mineral grains. Results from applying a nonlinear inversion procedure to the improved Hapke's RTM show that the average mass fraction of smaller and larger size SMFe in lunar soils was estimated to be 0.30% and 0.31% respectively, and the particle size distribution of soil samples is all within their measured range. Based on the derived mass fraction of SMFe and particle size of the soil samples, abundance of end-member components composing lunar soil samples was derived via minimizing the difference between measured and calculated spectra. The root mean square error (RMSE) between the fitted and measured spectra is lower than 0.01 for highland samples and 0.005 for mare samples. This improved Hapke's model accurately estimated abundance of agglutinitic glass (R-squared = 0.88), pyroxene (R-squared = 0.69) and plagioclase (R-squared = 0.95) for all 57 samples used in this study including both immature and mature lunar soils. However, the improved Hapke's RTM showed poor performance for quantifying abundance of olivine, ilmenite and volcanic glass. Improving the model performance for estimation of these three end-member components should be the central focus for our future work.

1. Introduction

Global determination of the abundance and distribution of minerals on the lunar surface is of significant importance for studying lunar geology (*Heiken et al*., 1992; *Hiesinger and Head*, 2006). The information can be used to characterize the lunar crustal structure and compositional variation with depth (*Pieters*, 1986; *Tompkins and Pieters*, 1999; *Jolliff et al*., 2000; *Cahill et al*., 2009). Identification of minerals on the lunar surface also provides evidence for the 'magma ocean' hypothesis which pertains to the evolution history of the Moon (*Smith et al*., 1970; *Wood*, 1975; *Warren*, 1990; *Wieczorek and Phillips*, 2000; *Elkins-Tanton et al*., 2002; *Ohtake et al*., 2009). Moreover, according to the mineralogy distribution of the lunar surface, some primary lunar sites for future resource utilization such as locations with abundant ilmenite can be determined (*Johnson et al*., 1991; *Melendrez et al*., 1994; *Standart and Hurtado*, 2012).

Remote sensing has proved its utility in mapping the lunar surface on a global scale. However, remotely sensed spectra of the lunar surface are strongly affected by space weathering which impedes our ability to remotely assess lunar mineralogy and composition. Space weathering refers to any alteration process acting on an airless body that greatly changes the physical, chemical and optical properties of planetary surface materials. It mainly involves solar wind sputtering and implantation, and micrometeorite bombardment (*Hapke*, 1965; *Hapke et al*., 1970; *Pieters et al*.,1993). A thin amorphous rim deposits on the surface of lunar soil grains by the growth of materials generated from solar wind sputtering and micrometeorite vaporization (*Hapke et al*, 1975; *Cassidy and Hapke*, 1975). As indicated by *Hapke* (1973, 2001) and *Cassidy and Hapke* (1975), such rims could contain abundant fine-grained submicroscopic metallic iron (SMFe) which manifests its

optical effects in several ways: reduction of overall reflectance, development of a red-sloped continuum, and attenuation of diagnostic absorption bands. With a longer exposure time to the space environment fresh lunar soils are weathered, gradually changing to a mature soil with an increasing component of SMFe. To accurately estimate mineral abundance on the lunar surface, space weathering effects must be compensated for in the modeling process.

Numerous empirical and statistical methods have been put forward to map the lunar surface mineralogy through remote sensing (*Sunshine et al*., 1990; *Sunshine and Pieters*, 1993; *Pieters et al*., 2002; *Shkuratov et al*., 2003; *Li*, 2006; *Korokhin et al*., 2008; *Tsuboi*, 2010). However, models in most of these applications cannot explicitly take the effects of space weathering into account and require 'ground truth' data which are constrained by limited lunar samples. Radiative transfer theory has the advantage over these methods in that it effectively accommodates the effects of space weathering and no 'ground truth' data are required. To date, two types of radiative transfer models (RTMs) are widely used for quantifying mineral abundance on the lunar surface. One is proposed by *Shkuratov et al*. (1999) and the other by *Hapke* (1981, 2001, 2005). In Shkuratov's model, although space weathering effects were considered in detail, the dependence of reflectance on viewing geometry was ignored. In contrast, Hapke's RTM can account for both spectral effects of viewing geometry and space weathering.

Many investigations have been carried out to explore the efficiency of Hapke's RTM in deriving mineral abundance of the lunar surface (*Mustard and Pieters*, 1987, 1989; *Clark et al*., 2001; *Lucey*, 2004; *Wilcox et al*., 2006; *Cahill and Lucey*, 2007; *Lawrence and Lucey*, 2007; *Denevi et al*., 2008; *Wu et al*., 2009; *Cahill et al*., 2009, 2010; *Yamamoto et al*.,

2010). Using Hapke's RTM, *Lucey* (2004) mapped the global mineral abundance of clinopyroxene, orthopyroxene, plagioclase and olivine for spectrally fresh lunar surface areas by means of creating a large lookup-table against which the lunar multispectral measurements were compared. *Cahill and Lucey* (2007) estimated mineral abundance of eleven spectral classes identified by *Tompkins and Pieters* (1999) through matching spectral classes to Hapke's radiative transfer computed spectra. *Denevi et al.* (2008) examined the ability of Hapke's RTM to reproduce reflectance spectra of lunar mare soils studied by the Lunar Soil Characterization Consortium (LSCC) considering all dominant regolith materials: agglutinitic glass, pyroxene, plagioclase, olivine, ilmenite and volcanic glass. Using Hapke's RTM, *Cahill et al*. (2009) successfully evaluated mineralogy of 55 impact crater central peaks and investigated the variation of lunar crustal composition with depth. *Ohtake et al*. (2009) reported the global distribution of pure anorthosite (~98% plagioclase) on the Moon by spectral unmixing using Hapke's model, providing a valuable constraint on the model of lunar magma ocean evolution. Recent work using Hapke's model has been done by *Cahill et al.* (2010) who used a lookup-table to determine Mg number and mineralogy of lunar highland and mare soils.

Several limitations exist in these previous applications of Hapke's model. First, some significant components such as agglutinitic glass and volcanic glass, which account for a large portion of the lunar soils, were not accommodated in their studies (*Lucey*, 2004; *Cahill and Lucey*, 2007; *Cahill et al*., 2009). This may lead to uncertainties in the estimated mineral abundance. Second, although other investigations have considered all the important components composing the lunar soils (*Denevi et al*., 2008; *Cahill et al*., 2010), their treatments of agglutinitic glass as a dark and neutral component were inappropriate

because space weathering effects (SMFe in agglutinitic glass) were not taken into account. Third, most applications of Hapke's RTM used a lookup-table to derive mineral abundance by setting fixed variation step for each mineral (*Clark et al*., 2001; *Lucey*, 2004; *Cahill and Lucey*, 2007; *Denevi et al*., 2008; *Cahill et al*., 2010). However, the values of measured mineral abundance may not be at these pre-set steps and thus will be inconsistent with the derived mineral abundance. Accounting for all these limitations, *Li and Li* (2011) used Newton's theory and the least square optimization method rather than a lookup-table to solve nonlinear equations to estimate abundance of agglutinitic glass, plagioclase, pyroxene, olivine, ilmenite and volcanic glass for 57 mare and highland soils samples measured by the Lunar Soil Constituent Consortium (LSCC). Mass fractions of SMFe and particle size of these soils samples were also reported in their study. Results showed that mineral abundance could be accurately evaluated only for fresh lunar soils although the estimated mass fraction of SMFe and particle size for all the soils samples are within their measured range. The poor performance of the method by *Li and Li* (2011) for mature lunar soils may result from an inaccurate expression in Hapke's RTM describing the effects of SMFe in lunar soils. Lunar soils contain both smaller and larger size SMFe and their spectral effects are different (*James et al*., 2002, 2003; *Noble et al*., 2007; *Lucey and Noble*, 2008; *Lucey and Riner*, 2011). The equation used in Hapke's model describing the effects of SMFe only represents the effects of smaller size SMFe in the rims of weathered transparent minerals, while it ignores larger size SMFe in the interior of agglutinitic glass.

In this study, an equation describing the effects of SMFe in agglutinitic glass proposed by *Lucey and Riner* (2011) was incorporated into the original Hapke's RTM. Building this modification onto the framework of *Li and Li* (2011) led to the development of an improved

Hapke's RTM. This study is aimed at testing whether the modification to Hapke's model by *Lucey and Riner* (2011) to accommodate the effects of larger size SMFe on lunar soil spectra can improve the performance of Hapke's RTM in reproducing measured reflectance and deriving mineral abundance for both immature and mature lunar soils.

2. Dataset

The LSCC dataset was used to test the improved Hapke's RTM. The dataset includes 9 mare and 10 highland soil samples prepared by the LSCC (*Taylor et al*., 1999, 2001, 2010), which contain the systematic measurements of compositional parameters along with lab reflectance spectra of these soils samples and is publically available at Reflectance Experiment Laboratory (RELAB) in Brown University. Each soil sample was subdivided into four particle size groups (< 10 μm, 10 – 20 μm, 20 – 45 μm, and < 45 μm). For the particle size groups < 10 μm, 10 – 20 μm, and 20 – 45 μm, measurements of corresponding reflectance, modal mineral abundance, and chemistry were carried out, generating 57 data samples (< 10 μm, 10 – 20 μm, 20 – 45 μm) to be analyzed in this study. The reflectance spectra of all these soil samples were measured at the incidence angle 30^{o}, emittance angle 0^{o} and phase angle 30^{o}.

3. Improved Hapke's Radiative Transfer Model

3.1. Hapke's RTM Corrected for the Effects of Larger Size SMFe

Assuming that materials on the lunar surface are intimately mixed and the grains of lunar soils are closely spaced with a particle size larger than observational wavelengths, *Hapke* (1981, 2001, 2005) provided an approximate analytic solution to the radiative transfer equation, which describes the scattering of light from the surface of a complex medium. In his work, the mixing systematic was linearized by converting the bidirectional

reflectance from a surface to its average single scattering albedo (SSA) via the following equation:

$$R = \frac{\omega_{ave}}{4\pi}\frac{\mu_0}{\mu_0+\mu}\{[1+B(g)]P(g) + H(\mu_0,\omega_{ave})H(\mu,\omega_{ave}) - 1\}, \quad (1)$$

where *R* is the bidirectional reflectance, ω_{ave} is the average SSA of all the components in the medium, μ_0 and μ are the cosine of the incidence angle and emittance angle, respectively, and g is the phase angle. *P(g)* is the phase function describing the angular pattern into which the incident power is scattered. In this study, a two-term Legendre polynomial of the form $P(g) = 1 + b\,cos\,g + c(3/2\,cos^2 g - 1/2)$ was employed, in which the parameter *b* describes the degree of forward and backward scattering and the parameter *c* describes the degree of side scattering. Using Hapke's RTM, *Mustard and Pieters* (1989) fitted the reflectance spectra of anorthite, olivine, enstatite and magnetite measured at several viewing geometries by allowing *b*, *c* and SSA of minerals to float. *Mustard and Pieters* (1989) concluded that each mineral defines a relatively unique suite of *b* and *c* values as a function of their SSA. To simplify our model, *b* and *c* were set to be -0.4 and 0.25 with reference to the values used by *Lucey* (1998). *B(g)* is the backscattering function describing the opposition effect. Because all the samples used in this study were measured at phase angle 30^0, which is greater than a phase angle of 15^0, thus the effect of backscattering was ignored (*Mustard and Pieters*, 1989). $H(\mu)$ is an approximation to the Chandrasekhar H-function which is shown in Eqs. 8.57, 8.22, and 8.25 in *Hapke* (2005).

One of the most important parameters in Eq. 1 is the average SSA (ω_{ave}) of the medium. *Hapke* (1981) stated that ω_{ave} of a mixture is a linear combination of SSA of each end-member component weighted by their mass fraction:

$$\omega_{ave} = \sum_i \frac{M_i\omega_i}{\rho_i D_i} / \sum_i \frac{M_i}{\rho_i D_i}. \quad (2)$$

i represents the i^{th} component, M_i is the mineral abundance, ω_i, ρ_i and D_i are the SSA, density, and mean grain size of the i^{th} component.

SSA of an end-member component (ω_i) is a function of its refractive index and grain size, and can be calculated using following equations given by *Hapke* (2005):

$$\omega = S_e + (1 - S_e)\frac{(1-S_i)\Theta}{1-S_i\Theta}, \quad (3)$$

$$S_e = \frac{(n-1)^2+k^2}{(n+1)^2+k^2} + 0.05, \quad (4)$$

$$S_i = 1 - \frac{4}{n(n+1)^2}, \quad (5)$$

$$\Theta = e^{-\alpha<D>}. \quad (6)$$

Here, S_e is the external surface scattering coefficient for Fresnel reflection from the surface of a particle averaged over all directions of incidence light on an external hemisphere of the particle. S_i is the internal surface scattering coefficient for light internally incident on the surface of the particle. *n* and *k* are the real and imaginary parts of the refractive index of an end-member component. Θ is the internal-transmission factor representing the total fraction of light entering the particle that reaches another surface after one transit. α is the absorption coefficient of an end-member component, and can be calculated by its refractive index via $4\pi nk/\lambda$, where λ is the wavelength. $< D >$ is the mean path length of light in the particle, a function of end-member particle size (*D*) that can be evaluated by Eq. 5.41 in *Hapke* (2005). In this research, Eqs. 3-6 were applied to calculate SSA for each end-member component composing LSCC soil samples. Values for the refractive index (*n* and *k*) of each end-member component used in this study can be referred to section 3.2.

As a result of space weathering, fine grained SMFe could accumulate both in the rims of weathered mineral grains (*Keller and McKay*, 1997; *Pieters et al*., 2000) and in the interior of agglutinitic glass. These SMFe change the physical properties and spectral features of lunar soils, reddening, darkening, and diminishing the spectral contrast of lunar soil spectra (*Fischer and Pieters*, 1994). *Hapke* (2001) incorporated these spectral effects of space weathering into the calculation of absorption coefficients α of end-member components defined as below:

$$\alpha = \frac{4\pi n_h k_h}{\lambda} + \frac{36\pi z M_c \rho_h}{\lambda \rho_{Fe}}, \tag{7}$$

where

$$z = \frac{n_h^3 n_{Fe} k_{Fe}}{(n_{Fe}^2 - {k_{Fe}}^2 + 2n_h^2)^2 + (2n_{Fe}k_{Fe})^2}. \tag{8}$$

Here, *n* and *k* are real and imaginary parts of the refractive index respectively and ρ is solid density. These three parameters correlated to the host mineral and SMFe by the suffixes *h* and *Fe*, respectively. M_c is the mass fraction of SMFe residing in the rim of a soil grain and λ is the wavelength. The first term on the right side of Eq. 7 represents absorption by a host end-member component and the second term describes the amount of light absorbed by SMFe imbedded within the rims of the host end-member component.

Although Hapke's radiative transfer theory as shown in Eqs. 1-8 has shown some success for quantifying mineral abundance of younger lunar soils, the results are not satisfactory for mature lunar soils (*Lucey*, 2004; *Li and Li*, 2011). *Li and Li* (2011) suggested that the poor correlation between measured and estimated mineral abundance for mature soils could be attributed to the inaccurate description of the effects of SMFe by using Eq. 7. Hapke's absorption coefficient for space weathered soils (Eq. 7) is only appropriate for the SMFe with particle sizes < 50 nm found in lunar soil grain coatings, not

the SMFe with particle sizes > 50 nm found mainly within the interior of host soil grains (*James et al*., 2002; 2003). This is especially the case for mature lunar soils containing abundant agglutinitic glass in which larger size SMFe is generated via the coalescence of smaller size SMFe during impact melting processes. Experimental work has demonstrated that SMFe of different size groups has very different spectral effects (*Nobel et al*., 2007). Smaller size SMFe increases the spectral slope over the visible to near-infrared wavelength range (reddening and darkening), whereas larger size SMFe tends to reduce overall reflectance and create little effect on the continuum slope (only darkening). *Lucey* (2008) compared the measured reflectance with computed reflectance from Hapke's RTM, and found that the computed reflectance cannot match the measured reflectance for samples containing larger size SMFe. Therefore, the effect of larger size SMFe on the spectra of lunar soils has to be compensated for achieving accurate estimation of lunar mineral abundance. Using Mie theory, *Lucey and Riner* (2011) modified Eq. 7 to model the effects of both smaller and larger size SMFe, reproduced below:

$$\alpha = \frac{4\pi n_h k_h}{\lambda} + \frac{36\pi z M_c \rho_h}{\lambda \rho_{Fe}} + \frac{3 q_a M_{in} \rho_h}{d_{Fe} \rho_{Fe}}, \quad (9)$$

where M_c is the mass fraction of smaller size SMFe imbedded within the rim of soil grain, M_{in} is the mass fraction of larger size SMFe in the interior of soil grains, and q_a is the absorption efficiency of a SMFe particle, which can be calculated through Mie theory. d_{Fe} is the particle size of large grained SMFe, and *z* is defined by Eq. 8. The first two terms on the right side of Eq. 9 are the same as those in the original Hapke's model representing absorption of light resulting from host minerals and smaller size SMFe in the rims of soil grains. The third term on the right side of Eq. 9 is used to account for absorption of light by larger size SMFe in the interior of host grains.

In this study, the absorption coefficient of agglutinitic glass was calculated using Eq. 9 because agglutinitic glass is not only enriched in smaller size SMFe in the rim (<50 nm) but also contains some amounts of SMFe with particle size larger than 50 nm (*James et al*., 2002; 2003). For calculations of the absorption coefficient of other end-member components in lunar soils, Eqs. 7-8 were employed based on the observation that these components only contain the extremely fine grained SMFe with particle size smaller than 50 nm residing in the rims of their grains (*Keller and McKay*, 1993, 1997).

3.2. Determination of Imagery Part (*k*) of End-members' Refractive Index

Quantifying mineral abundance using Eqs. 1-9 requires the refractive index of each end-member component and also SMFe to be determined first. In this study, all the major components in lunar soils were considered including agglutinitic glass, orthopyroxene, clinopyroxene, plagioclase, olivine, ilmenite, and volcanic glass. The corresponding reflectance spectra used to calculate *k* of these end-member components are shown in Fig. 3-1. All these spectra were selected from the RELAB spectral library at Brown University with their sample ID shown in Table 3-1. The end-member minerals were all separated from Apollo samples except ilmenite. To derive *k* for mineral end-members from RELAB spectra, the real part of refractive index (*n*) and particle size (*D*) of these selected end-members were specified (Tables 3-1 and 3-2). *Lucey* (1998) found that the variation of the real part (*n*) of refractive index of orthopyroxene, clinopyroxene, and olivine is a function of their composition (Mg number). The variation range is 1.65 to 1.77, 1.64 to 1.73, and 1.64 to 1.83 for orthopyroxene, clinopyroxene, and olivine respectively. For simplicity, we assumed that each end-member component in different LSCC soil samples has the same *n*, and 1.77, 1.73, and 1.83 were used for orthopyroxene, clinopyroxene, and olivine,

respectively. The *n* value for plagioclase was set as 1.56 (*Egan and Hilgeman*, 1973). Agglutinitic glass was assumed to have the same *n* value as silica glass, which was reported to be 1.49 (*Kitamura et al*., 2007). This value is also within the range of measured *n* for a suite of synthetic glasses (1.42 to 1.75) by *Ghosh* (1998). The real part (*n*) of refractive index of all these end-member components is the same as that used in the work of *Li and Li* (2011). Because the particle size value presented in Table 3-1 for each end-member component has a wide range, the mean value of each of these ranges was set as the particle size of end-member component for calculating its *k*. On the basis of these fixed *n* and particle size of end-member components, the imaginary part (*k*) of refractive index of these end-member components was derived from their corresponding reflectance spectrum by solving the non-linear equation for their measured reflectance spectrum (*R*) and *k* using Newton's method. Detailed processes of deriving *k* can be referred to *Li and Li* (2011). The spectrum of volcanic glass is not shown in Fig. 3-1 because the refractive index of volcanic glass was not derived by the method of *Li and Li* (2011). It was calculated by use of the method of *Wilcox et al*. (2006), i.e. a linear relationship between FeO and TiO_2 content of volcanic glass and its refractive index at each wavelength. First, the FeO and TiO_2 content of all soil samples presented by *Taylor et al*. (2001) was averaged respectively in this study. Then, these two averaged values were input into the model of *Wilcox et al*. (2006) to calculate the refractive index (*n* and *k*) of volcanic glass. The refractive index of SMFe used in this work was reported by *Johnson and Christy* (1974), who determined *n* and *k* of SMFe by inverting normal-incidence reflection and transmission functions with the reflection and transmission measurements on a vacuum-evaporated thin film of iron metal.

[Insert Figure 3-1 here]

[Insert Table 3-1 here]

[Insert Table 3-2 here]

3.3. Determination of Single Scattering Albedo of Ilmenite

The estimated refractive index using above method can be applied in Eqs. 3-9 to compute SSA for agglutinitic glass, plagioclase, orthopyroxene, clinopyroxene, olivine and volcanic glass. However, SSA of opaque ilmenite cannot be evaluated through its refractive index because Eqs. 3-9 are only appropriate for transparent minerals with $k << 1$ (*Hapke*, 2005). In this study, SSA of ilmenite was derived by feeding the measured reflectance spectrum of ilmenite (Table 3-1: MR-MSR-006) into Eq. 1. The derived SSA for ilmenite was then used with the SSA of other end-member components to evaluate the average SSA of lunar soils. One limitation of this treatment is that the space weathering effects on ilmenite cannot be accommodated. However, as indicated by *Pieters* (2000) and *Chapman* (2004), opaque minerals are less affected by modification by space weathering. Therefore, the space weathering effects on ilmenite can be ignored.

3.4. Deriving SMFe, Particle Size of Soil Grains, and Mineral Abundance

Sensitivity analysis reveals that the performance of Hapke's RTM is significantly influenced by variations in soil particle size and SMFe mass fraction, such that the diagnostic spectral signatures for various minerals can be suppressed by these grain size variations and SMFe mass fractions (*Liu et al*., 2013). A small variation in particle size of soil grains and/or mass fraction of SMFe leads to a large deviation in the estimated mineral abundance (*Lucey*, 1998; *Warell and Davidsson*, 2010; *Trang et al*., 2013). It is a great challenge to predict mineral abundance, particle size of soil grains, and mass fraction of SMFe simultaneously from measured reflectance spectra. Therefore, to accurately estimate

mineral abundance, mass fractions of both smaller and larger size SMFe and particle size of soil samples should be known. However, no measured data are currently available for these parameters. Although the particle size range of the soil samples was reported by LSCC, no measurement of the median value was provided. Thus, the values of these parameters need to be derived first. In *Li and Li* (2011), the measured spectra and mineral abundance provided by the LSCC dataset were used as known input into Hapke's model. Mass fraction of SMFe and the particle size of soil samples were set as free parameters to vary within their ranges. Newton's method and least square were used to solve for SMFe and particle size of soil grains by minimizing the difference between fitted and measured reflectance spectra:

$$\boldsymbol{\varepsilon} = R(PS, M_c) - R_{measured}\ , \tag{10}$$

where R is the calculated bidirectional reflectance by Eqs. 1-8, and modeled as a function of mass fraction of SMFe (M_c) and particle size (PS) of soil grains, and $R_{measured}$ is the measured bidirectional reflectance by LSCC. In this study, we added another free parameter to represent the mass fraction of large size SMFe (>50 nm) in the interior of agglutinitic glass denoted as M_{in} in addition to using M_c to represent the mass fraction of smaller size SMFe residing in the rims of mineral grains and agglutinitic glass. According to *Li and Li* (2011), and using known spectra and mineral abundance provided by LSCC as input into the Hapke's model, the non-linear equation in Eq. 10 is modified as:

$$\boldsymbol{\varepsilon} = R(PS, M_{in}, M_c) - R_{measured}\ . \tag{11}$$

Here, R is calculated reflectance via Eqs. 1-9 as a function of particle size of soil grains, mass fraction of smaller and larger size SMFe. When $\boldsymbol{\varepsilon}$ is minimized, the optimized soil particle size, mass fraction of both smaller and larger size SMFe can be obtained.

After this step, the similar fitting procedure was repeated for estimating the abundance of minerals from the measured spectra by LSCC in which derived particle size of soil grains and mass fractions of smaller and larger size SMFe were used as known inputs for the Hapke's model, but mineral abundance as unknown to derive. Solving the following non-linear equation

$$\boldsymbol{\varepsilon} = R(mineral\ abundance) - R_{measured}\ , \qquad (12)$$

leads to optimized mineral abundance of all end-member components. The fitted spectra were also obtained through this fitting process. Comparison between fitted spectra and measured spectra by LSCC was employed as the first-order measure for accuracy of derived mineral abundance.

4. Results and Discussion

4.1. Estimated SMFe and Particle Size of Soil Grains

Shown in Figs. 3-2 and 3-3 are the derived mass fractions of smaller size SMFe (< 50 nm) in the rims of mineral grains and larger size SMFe (> 50 nm) in the interior of agglutinitic glass. In these two figures, the sample numbers 1-19, 20-38, and 39-57 represent lunar soil samples with particle size < 10 μm, 10 - 20 μm, and 20 – 45 μm, respectively. The mass fractions of smaller and larger size SMFe increase with decreasing particle size of soil samples. This is consistent with the results of other investigations (e.g., *Morris*, 1977; *Taylor et al*., 2001, 2010). *Taylor et al*. (2001, 2010) found the value of *Is*/FeO increased with decreasing particle size for each LSCC soil sample. As an index of surface exposure time, *Is*/FeO indicates that small particle size groups of LSCC soil samples might have longer exposure time to space environment and a greater amount of smaller size SMFe could accumulate in small size lunar soils through continual reduction

of Fe^{2+} induced by implanted solar wind and micrometeorites impacts. This process also enhances the possibility of the generation of larger size SMFe within small grain lunar soils via the coalescence of abundant smaller size SMFe. Although the mass fractions of smaller and larger size SMFe increase with decreasing lunar soil particle size, the change of the mass fraction of larger size SMFe between different soil particle size groups is not as evident as that of smaller size SMFe, espectially for the variation from particle size group 10 – 20 μm to particle size group < 10 μm. This can be accounted for by the fact that the < 10 μm size fraction is most sensitive to surface-correlated processes (*Pieters et al*., 2000; *Noble et al*., 2001) and when particle size of soil grains decreases, smaller size SMFe in the rims of mineral grains could increase substantially (*Taylor et al*., 2001, 2010). The average mass fraction of smaller and larger size SMFe of all the 57 soil samples is 0.30% and 0.31% respectively. This result is close to the values reported in *Morris* (1980) who estimated the mass fraction of SMFe in the lunar soil to be 0.20% for smaller size SMFe and 0.34% for larger size SMFe. The derived mass fraction of smaller SMFe (0.30%) in our study is slight higher than that of *Morris* (1980) (0.20%), which can be explained by the different particles size of lunar soil samples used in these two studies. In *Morris* (1980), the mass fraction of SMFe was estimated through investigating soil samples with particle size < 250 μm which is quite larger than the particle size applied in this study (< 45 μm). As stated by *Taylor et al*. (2001, 2010), the content of SMFe increases with decreasing particle size of lunar soils. This could result in the higher estimated mass fraction of SMFe in our study with particle size < 45 μm relative to that of *Morris* (1980) with particle size < 250 μm. Two size groups of sample 71061 (< 10 μm and 10 – 20 μm) show extreme high mass fraction of larger size SMFe (Fig. 3-3) with their content up to 1.8% and 1.2%. These

two extremely high values of larger size SMFe may result from the unusual component in sample 71061. A significant abundance of black beads (9%) is contained in soil 71061 (*Heiken and McKay,* 1974) leading to a different spectral characteristic from spectra of other samples (*Nobel et al*., 2001; *Taylor et al*., 2001). However, black beads were not considered as a mineral end-member when we attempted to estimated mass fraction of SMFe and particle size for 71061 through fitting the measured spectrum, which may result in the inaccurate estimation for its mass fraction of SMFe.

Estimated particle size values for all the 57 soil samples in the LSCC dataset are shown in Fig. 3-4. It can be seen that the estimated particle size for all these three size groups is within their corresponding ranges measured by LSCC. The agreement between predicted and measured mass fraction of SMFe and soil particle size demonstrates the efficiency of this improved Hapke's RTM in deriving the SMFe content and particle size of lunar soils from measured reflectance spectra, and confirms the feasibility of the approach proposed by *Lucey and Riner* (2011) in describing the effects of large size SMFe in lunar soils.

[Insert Figure 3-2 here]

[Insert Figure 3-3 here]

[Insert Figure 3-4 here]

4.2. Fitted Spectra

Shown in Figs. 3-5 and 3-6 are the comparison between modeled and measured spectra for highland and mare lunar soil samples. These modeled spectra can be used as the first-order accuracy estimation for the derived mineral abundance. Here only the 10 - 20 μm size group samples are shown because their spectral characteristics are most representative of bulk lunar soils (*Pieters et al*., 1993). For highland samples (Fig. 3-5), all the fitted

spectra agree well with measured spectra with the lowest RMSE being 0.0019 and highest RMSE being less than 0.01. The highest RMSE values occurred for samples 61221, 67461, and 67481 for which modeled spectra show lower reflectance than the measured LSCC spectra in the wavelength region between 1250 nm and 1400 nm. This slight discrepancy may be attributed to the end-member plagioclase selected in this study. It is acknowledged that the variation of measured reflectance spectra of lunar soils manifests itself mainly by changing their reflectance magnitude which could be controlled by the content of plagioclase. To fit the measured reflectance spectra of the LSCC lunar soils accurately, the improved Hapke's RTM was forced to fit the magnitude of reflectance by changing the content of plagioclase, while the absorption features of lunar soils were weighted less. The end-member spectrum of plagioclase selected in this study exhibits a strong absorption feature around 1300 nm (Fig. 3-1), and all these three samples contain the highest abundance of plagioclase as compared to other soil samples. When such high abundance of plagioclase were determined for accurately fitting the magnitude of the measured reflectance spectra for the three samples (sample: 61221, 67461, and 67481), a misfit was yielded for the strong absorption of selected end-member plagioclase at around 1300 nm because the actual plagioclase contained in these three soil samples might not possess such strong absorption around 1300 nm as the selected plagioclase end-member. For mare samples, the modeled spectra fit well with measured spectra with the lowest and highest RMSE being 0.001 and 0.0044 respectively. A slight mismatch between modeled and measured spectra occurs for samples 71501, 79221, 70181, 10084 and 12030 for which modeled spectra show lower reflectance and redder slope than that measured in the short wavelength region. This drop off in the short wavelength region might be attributed to a

feature in the spectrum of the real part (*n*) of refractive index of iron metal (SMFe) (*Lucey and Noble*, 2008).

Nevertheless, all the effects analyzed above have no significant impact on the estimated mineral abundance as indicated by the low RMSE between modeled and measured spectra for all the samples.

[Insert Figure 3-5 here]

[Insert Figure 3-6 here]

4.3. Estimated Mineral Abundance

Shown in Fig. 3-7 and Table 3-3 are the comparison between predicted and measured mineral abundances for both immature and mature lunar soils. Here, the sum of the derived mineral abundances for orthopyroxene and clinopyroxene was used to compare with the measured abundance of pyroxene. It can be seen from Fig. 3-7 that the estimated abundance for agglutinitic glass, pyroxene, and plagioclase are highly correlated to the measured abundance with the coefficient of determination (R-squared) being 0.88, 0.69 and 0.95 respectively. The estimated abundance of agglutinitic glass shows the most pronounced improvement with an R-squared of 0.88 over the result of *Li and Li* (2011) with an R-squared of 0.72. This could be contributed to that the improved Hapke's model effectively accounted for the influence of larger size SMFe in the agglutinitic glass. Moreover, the improved Hapke's RTM shows good performance in estimating agglutinitic glass, pyroxene, and plagioclase for all the 57 lunar samples including both immature and mature lunar soils, contrasting to the results of *Li and Li* (2011) where high correlation was obtained merely for immature soil samples. However, the estimated abundances for ilmenite, olivine, and volcanic glass are poorly correlated with the measured abundance as

indicated in Table 3-3. For ilmenite, it is overestimated although there is a relatively high R-squared between measured and predicted abundance. This is because the influence of smaller size SMFe embedded in the rims of ilmenite was not taken into account in our model when calculating its SSA. SMFe can reduce the reflectance significantly. To fit the low reflectance of soil samples, a higher amount of dark ilmenite would be required to compensate for the lack of SMFe. In addition, experimental studies on mineral abundance deconvolution (*Yan et al*., 2008; 2010) showed that minerals of lower reflectance would be overestimated and minerals of higher reflectance would be underestimated in mineral mixtures. The overestimated abundance of ilmenite could result from a compensation for the slightly underestimated abundance of plagioclase in this work (Fig. 3-7). The estimated abundance of olivine shows a large deviation from measured data. This can be explained by three reasons. First, the refractive index (*n* and *k*) for olivine used in this study was fixed for all the 57 lunar samples. However, the refractive index of olivine is determined by its chemical composition and in reality is a function of its Fe^{2+} and Mg^{2+} proportion (Mg number) (*Lucey*, 1998; *Trang et al*., 2013). Lunar samples contain olivine of diverse composition ranging from Mg-rich forsterite to Fe-rich fayalite (*Isaacson et al*., 2011) and their refractive index should be different. LSCC measured the FeO and MgO content of olivine for highland and high-Ti mare soil samples used in this study. The Mg number of olivine in these samples ranges from 48 to 64 (*Taylor et al*., 2010), assigning one refractive index value for olivine in all the 57 samples could introduce errors in estimating their olivine content. Second, the 1050 nm absorption band of olivine is close to the absorption band of pyroxene around 1000 nm, and the former could be masked out by the latter. *Adams* (1974) examined the spectra of a suite of pyroxene and olivine mixtures and found that

even when the content of olivine is up to 50%, its absorption feature is not yet detectable. All the soil samples used in this study contain olivine with their abundance lower than 5%. It is difficult for the model to distinguish such a small portion of olivine from pyroxene. Third, laboratory simulations of space weathering effects have shown that olivine is weathered more rapidly relative to pyroxene (*Sasaki et al*., 2001; 2002). This might indicate that the spectral feature of olivine could be lost rapidly when a small amount of SMFe is generated in lunar soils, leaving the absorption features of lunar soils mainly dominated by pyroxene. Therefore, a variation of olivine in its abundance contributes much smaller to the measured reflectance than that of pyroxene and the improved Hapke's model is insensitive to the variation of olivine content. The improved Hapke's model also shows poor performance for evaluating the content of volcanic glass. One reason might be ascribed to inaccurate calculation of the refractive index of volcanic glass. The regressed relationship between the refractive index of volcanic glass and the FeO and TiO_2 contents from *Wilcox et al.* (2006) was based on seven synthetic glasses samples. However, volcanic glass on the lunar surface shows a larger chemical variation. This regressed relationship might not cover all the compositional variations within the volcanic glass. Thus, the estimated value cannot represent the actual refractive index of volcanic glass that is included in the soil samples, which could introduce bias in the estimated results. Moreover, volcanic glass exhibits broad 1 μm and 2 μm absorptions and could be masked out by the absorptions of pyroxene because of strong overlapping. This strong absorption interference from pyroxene might also degrade the estimation accuracy for the abundance of volcanic glass.

[Insert Figure 3-7 here]

[Insert Table 3-3 here]

5. Limitations of the Improved Hapke's Radiative Transfer Model

Our previous work demonstrated that it is difficult to predict mineral abundance, soil grain size, and SMFe mass fraction simultaneously with measured reflectance data. *Liu and Li* (2013) conducted a sensitivity analysis for a suite of reflectance spectra simulated with Hapke's RTM to determine the relative importance of the mass fraction of SMFe, *PS* and mineral abundance in regulating the reflectance of lunar soils. Results show that SMFe and particle size have the strongest impact across the whole wavelength regions and they are the two most important factors that drive the variation of lunar soil reflectance.

One plausible solution to this problem is that the particle size of soil grains, and the mass fraction of smaller and larger size SMFe could be first predicted using other approaches, and then the derived values are input into the improved Hapke's RTM to determine mineral abundance in lunar soils. For example, the mass fraction of smaller size SMFe can be estimated by the ratio of 540 nm/810 nm single scattering albedo of measured reflectance spectra (*Liu and Li*, 2015), and the mass fraction of larger size SMFe can be evaluated using Eq. 6 of *Morris* (1980) based on measured maturity index. Thermal inertia data obtained from Diviner Lunar Radiometer Experiments aboard Lunar Reconnaissance Orbiter and radar data can also be used to determine particle size of soil grains (*Zisk et al*. 1974; *Presley*, 2002; *Gupta and Ghent*, 2008; *Gundlach and Blum*, 2013).

Although this improved Hapke's RTM is unable to predict mineral abundance without prior knowledge on the particle size of soil grains and mass fraction of SMFe, this study has demonstrated that the effects of larger size SMFe on measured reflectance should be considered in Hapke's RTM to fully address the effects of space weathering on lunar soils.

Prediction of lunar mineral abundance is significantly improved using this improved Hapke's RTM as long as knowledge on the particle size of soil grains and the mass fraction of smaller and larger size SMFe is available. This study represents a step forward toward ultimately mapping global mineralogy of the lunar surface.

6. Conclusions and Future Work

Based on the work of *Lucey and Riner* (2011) and *Li and Li* (2011), an improved Hapke's RTM has been developed. In this improved Hapke's RTM, the spectral influence of space weathering on the lunar soils is accounted for by considering the effects of both smaller size SMFe residing in the rims of soil grains and larger size SMFe in agglutinitic glass. The mass fraction of SMFe and grain size of all the 57 LSCC soil samples were estimated by using this improved Hapke's RTM. What this investigation differs from previous studies lies in that mass fractions of larger size SMFe of lunar soils were first evaluated with the corresponding mean value being 0.31, which is in accordance with results of *Morris* (1980). The measured LSCC spectra of each soil sample can be accurately fitted by this improved Hapke's RTM. The maximum RMSE between calculated and measured reflectance spectra is no larger than 0.01 for highland samples, and less than 0.005 for mare samples. Additionally, this improved Hapke's RTM indeed enables relatively accurate prediction on abundance of agglutinitic glass, pyroxene, and plagioclase for both immature and mature lunar soils. Through addition of larger size SMFe effects into the original Hapke's RTM, the improved Hapke's model can efficiently reveal the characteristics of space weathered mature lunar soils and raise the estimation accuracy of mineral abundance for mature lunar soils.

However, this improved Hapke's RTM shows poor performance for deriving abundance of olivine, ilmenite, and volcanic glass. One reason may be due to improper treatment of some end-members, such as deriving SSA of ilmenite with rims containing SMFe and calculating refractive index values of olivine and volcanic glass. On the other hand, because of low abundance of these three end-members in lunar soils, their contributions to measured spectra are very limited compared to that of agglutinitic glass, pyroxene, and plagioclase. It is a great challenge for this improved Hapke's RTM to accurately estimate their abundance through measured spectra.

In future work, new treatments to calculate SSA of ilmenite are required by taking into account SMFe in the rims of its grains. Furthermore, Mg number associated with the chemical composition of end-member components should be introduced into this improved Hapke's RTM. This would allow to further constrain the refractive index of (n and k) of silicate minerals, especially for olivine, and improve the model performance. After making these modifications, this improved Hapke's model could ultimately be used to quantify the mineral abundance on the lunar surface.

Acknowledgements

We thank Bruce Hapke and Deborah Domingue for their insights and comments, which greatly improved the manuscript. We also acknowledge the assistance of Kaishan Song, Shuai Li, and Zuchuan Li for their technical support.

Table Captions

Table 1. Spectra information of selected end-members in this study.

Table 2. Refractive indices of all end-member components used in this study.

Table 3. Regressed parameters for ilmenite, olivine and volcanic glass.

Table 3-1

Mineral	RELAB sample ID	Size range (µm)	Size used (µm)	Reference
Agglutinitic glass	LU – CMP – 007 - 1	100-1000	550	RELAB
Orthopyroxene	LR – CMP - 173	0-125	62.5	RELAB
Clinopyroxene	LR – CMP - 170	0-125	62.5	RELAB
Plagioclase	LR – CMP - 171	0-125	62.5	RELAB
Olivine	LR – CMP - 169	0-125	62.5	RELAB
Ilmenite	MR – MSR -006	0-20	--	RELAB
Volcanic glass	--	--	--	--

Table 3-2

Mineral	Refractive index (*n*)	Reference
Agglutinitic glass	1.49	*Kitamura et al*. (2007)
Orthopyroxene	1.77	*Lucey* (1998)
Clinopyroxene	1.73	*Lucey* (1998)
Plagioclase	1.56	*Egan and Hilgeman*, (1973)
Olivine	1.83	*Lucey* (1998)
Ilmenite	--	--
Volcanic glass	--	*Taylor et al*. (2001), *Wilcox et al*. (2006)

Table 3-3

Mineral	Slope	Intercept	R^2
Ilmenite	1.58	0.74	0.62
Olivine	1.41	1.88	0.18
Volcanic glass	0.29	1.42	0.17

Figure Captions

Figure 3-1. Reflectance spectra of end-members used in this study (from RELAB).

Figure 3-2. Estimated mass fraction of smaller size SMFe of three size group soil samples of LSCC dataset.

Figure 3-3. Estimated mass fraction of larger size SMFe of three size group samples of LSCC dataset.

Figure 3-4. Estimated particle size for three size group samples of LSCC dataset.

Figure 3-5. Comparison between modeled and measured spectra for highland soil samples with particle size of 10 – 20 μm.

Figure 3-6. Comparison between modeled and measured spectra for mare soil samples with particle size of 10 – 20 μm.

Figure 3-7. Correlation between derived and measured mineral abundance of agglutinitic glass, pyroxene and plagioclase.

Figures

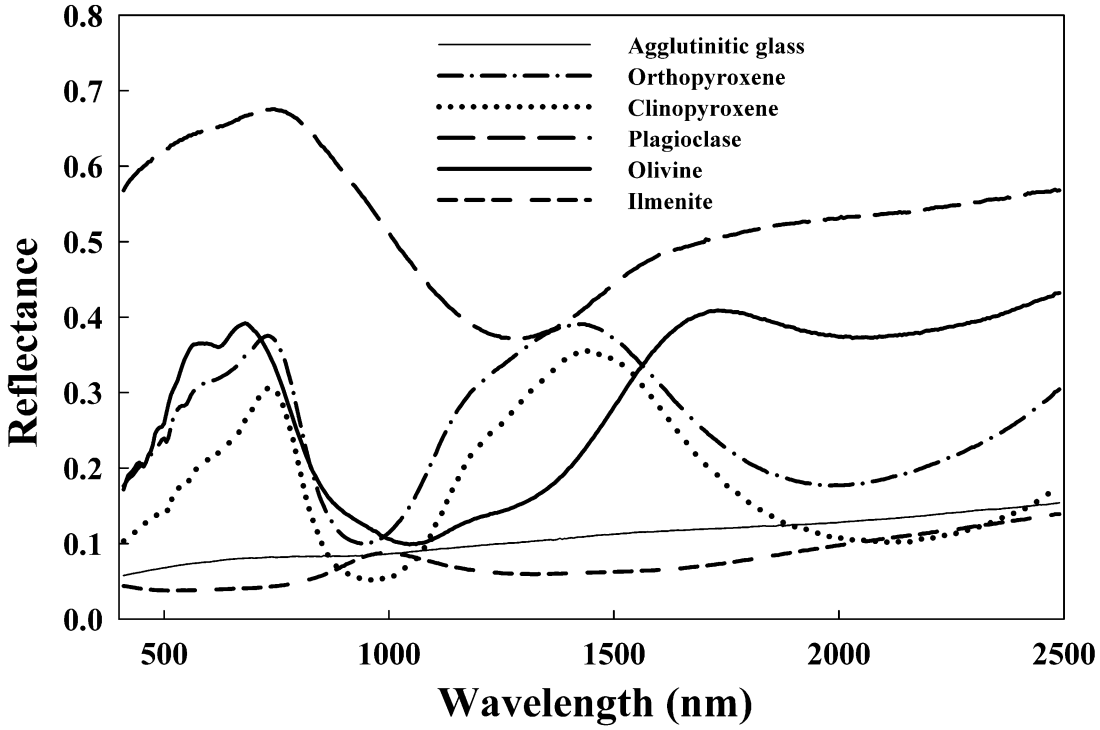

Figure 3-1

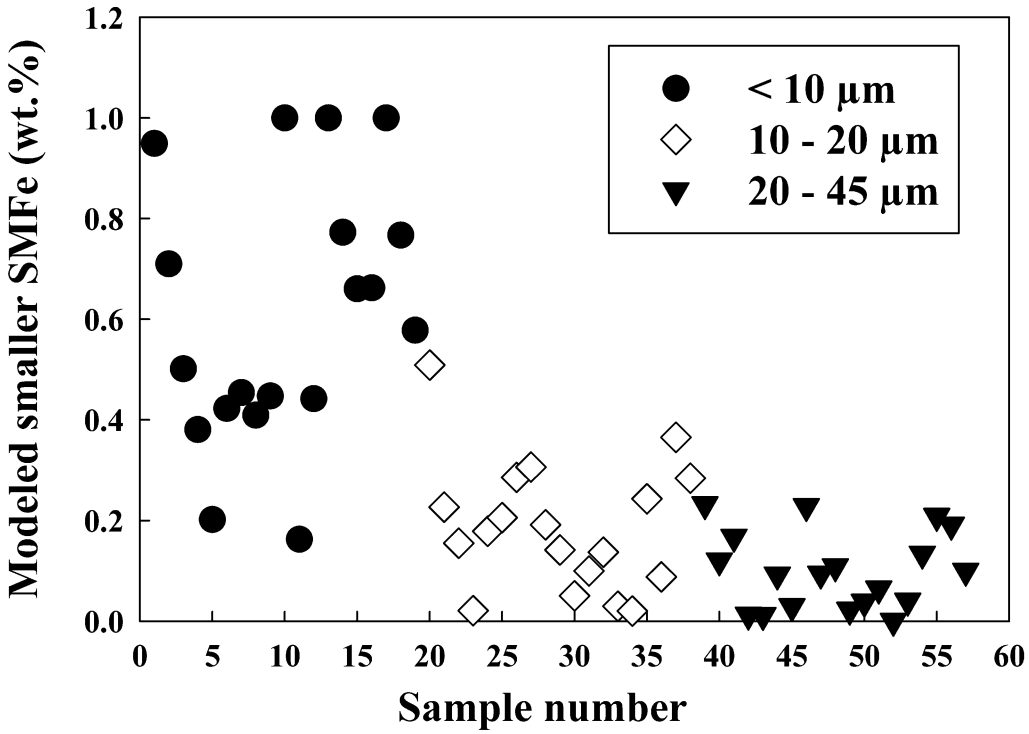
Modeled smaller SMFe (wt.%)
1.2
1.0
0.8
0.6
0.4
0.2
0.0
0
5
10
15
20
25
30
35
40
45
50
55
60
Sample number
< 10 µm
10 - 20 µm
20 - 45 µm

Figure 3-2

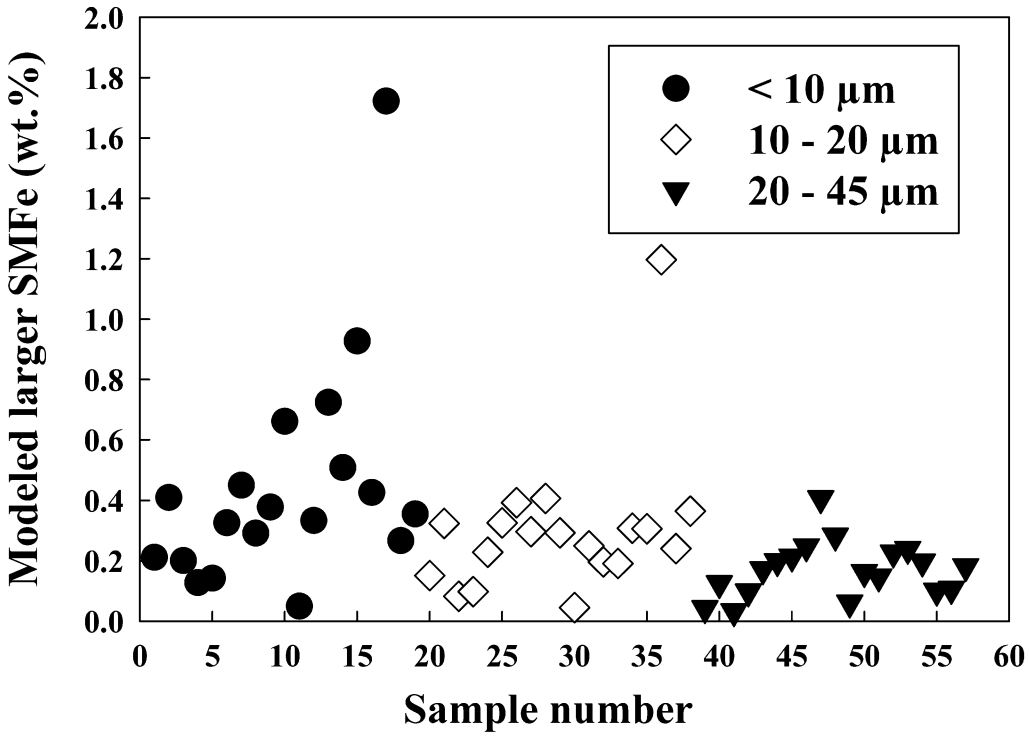
Modeled larger SMFe (wt.%)
2.0
1.8
1.6
1.4
1.2
1.0
0.8
0.6
0.4
0.2
0.0
0
5
10
15
20
25
30
35
40
45
50
55
60
Sample number
< 10 µm
10 - 20 µm
20 - 45 µm

Figure 3-3

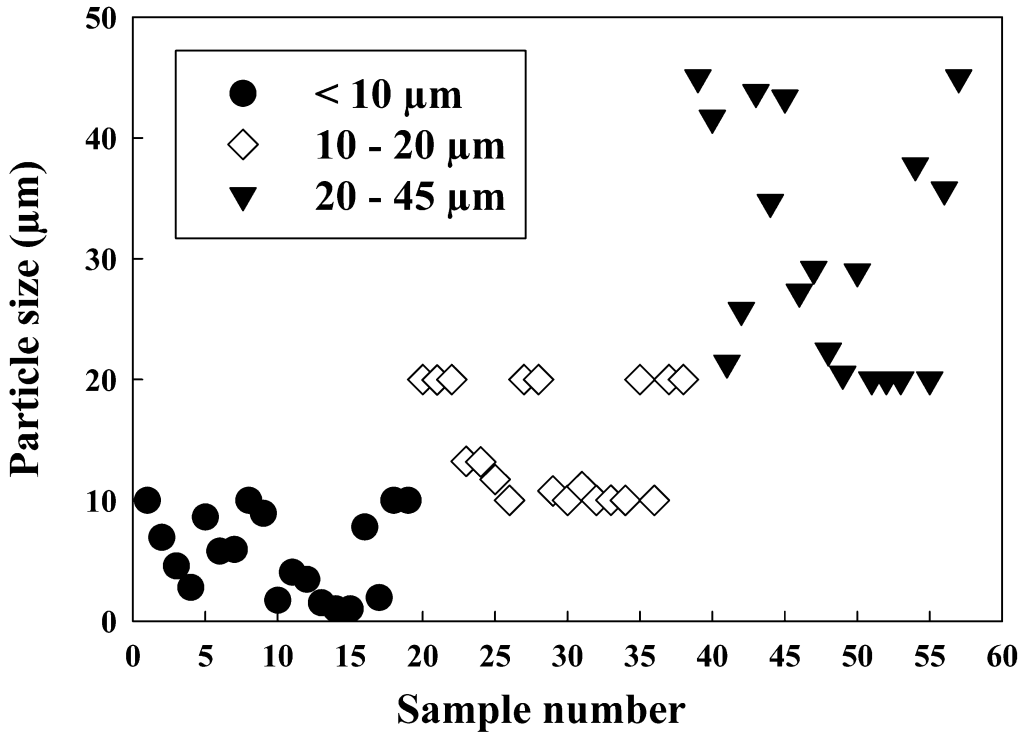
< 10 µm
10 - 20 µm
20 - 45 µm
Particle size (µm)
Sample number
0
10
20
30
40
50
0
5
10
15
20
25
30
35
40
45
50
55
60

Figure 3-4

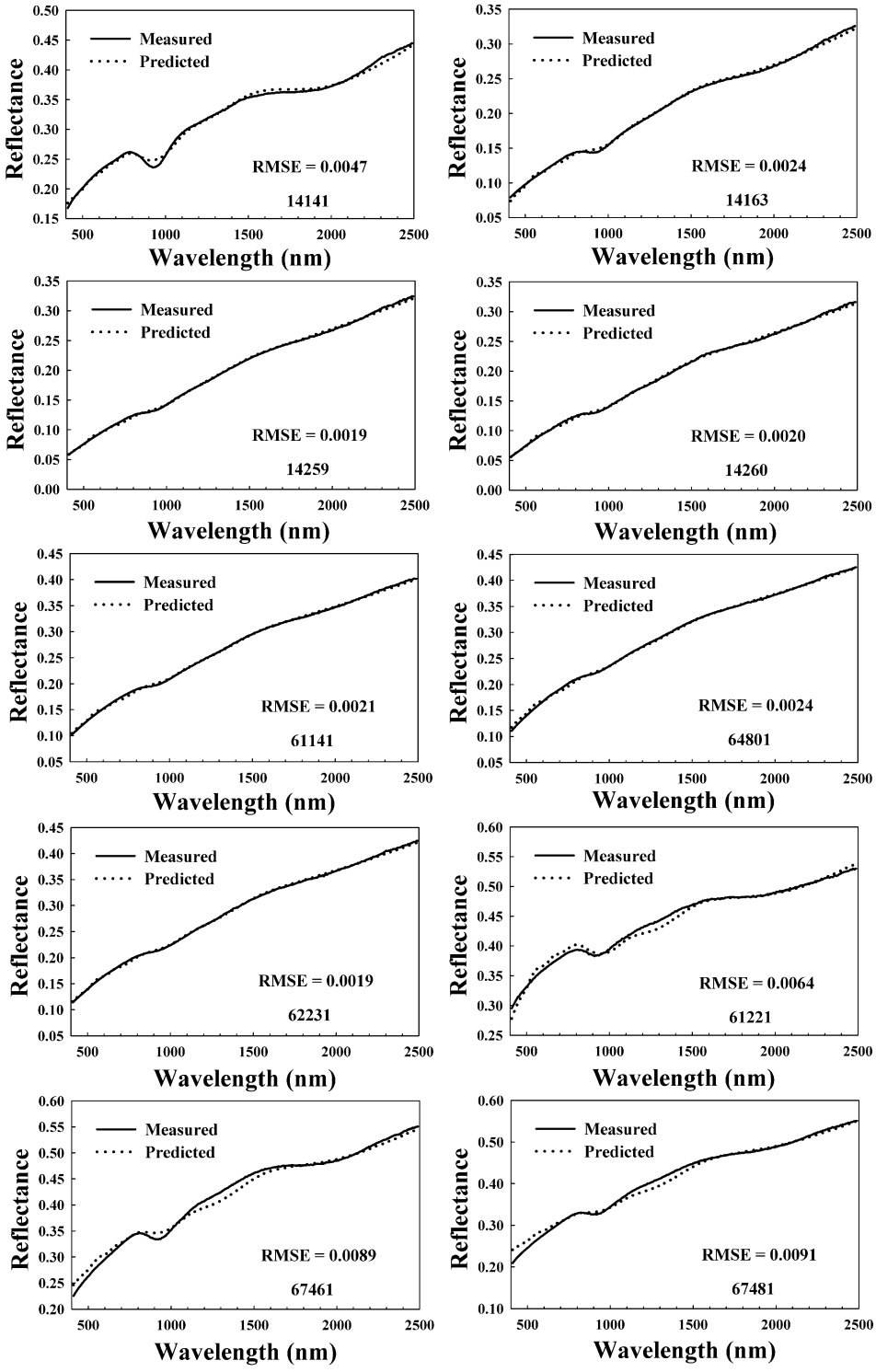
Measured
Predicted
Reflectance
Wavelength (nm)
RMSE = 0.0047
14141
RMSE = 0.0024
14163
RMSE = 0.0019
14259
RMSE = 0.0020
14260
RMSE = 0.0021
61141
RMSE = 0.0024
64801
RMSE = 0.0019
62231
RMSE = 0.0064
61221
RMSE = 0.0089
67461
RMSE = 0.0091
67481

Figure 3-5

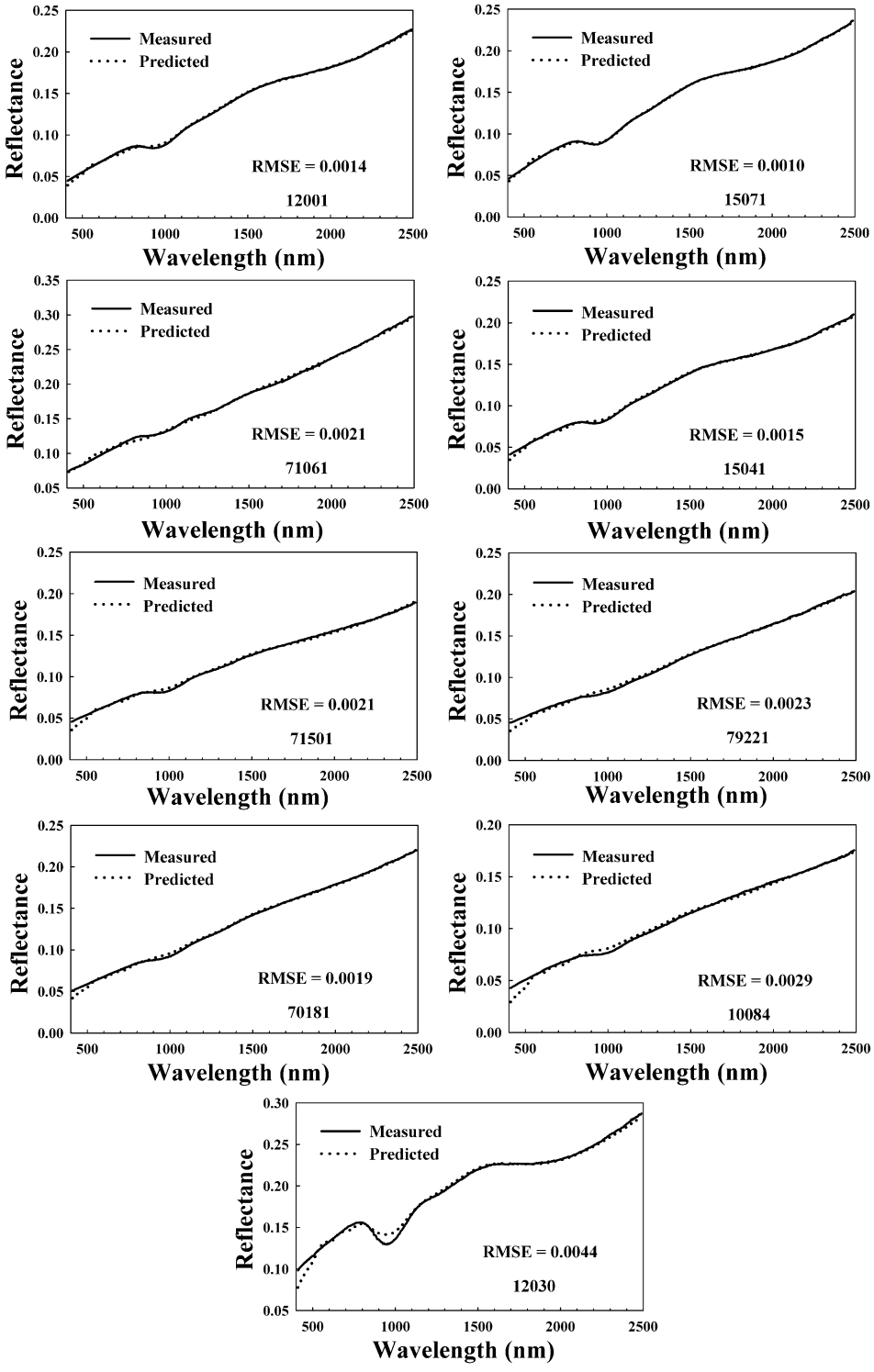
Measured
Predicted
Reflectance
Wavelength (nm)
RMSE = 0.0014
12001
RMSE = 0.0010
15071
RMSE = 0.0021
71061
RMSE = 0.0015
15041
RMSE = 0.0021
71501
RMSE = 0.0023
79221
RMSE = 0.0019
70181
RMSE = 0.0029
10084
RMSE = 0.0044
12030

Figure 3-6

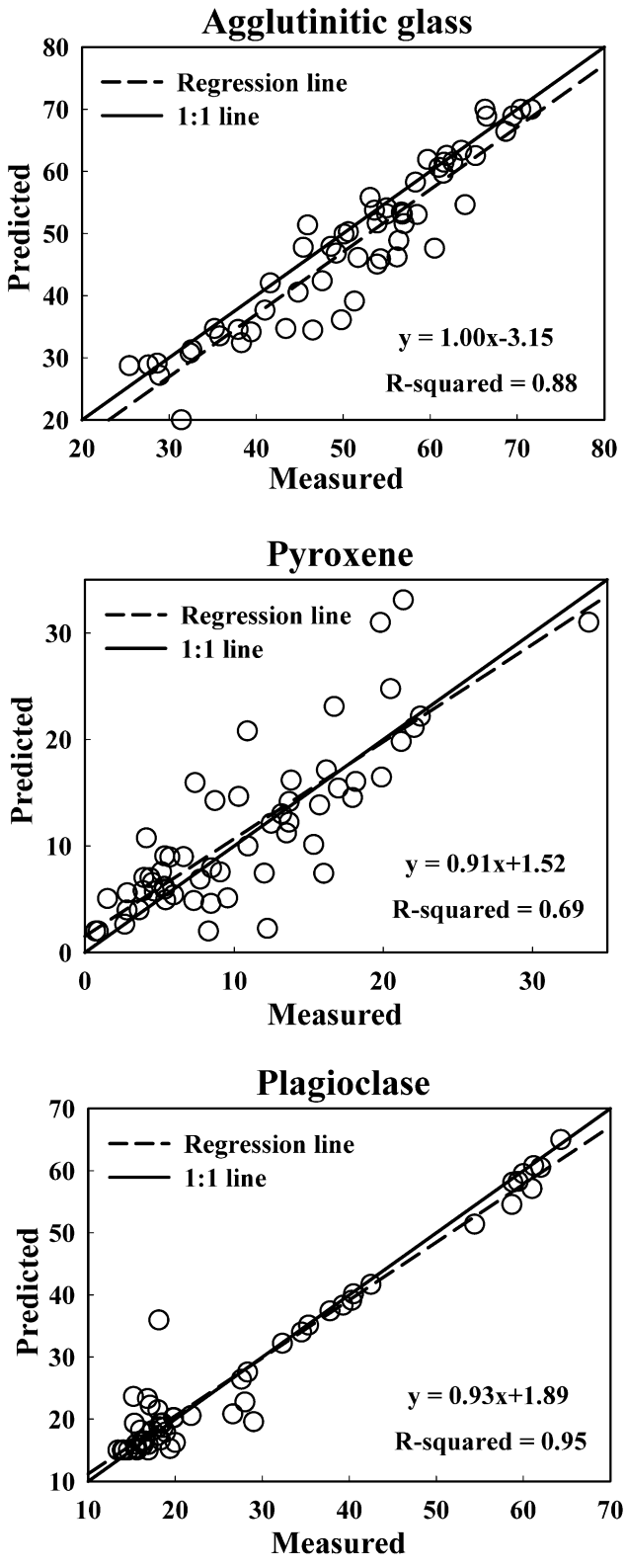
Agglutinitic glass
Regression line
1:1 line
y = 1.00x-3.15
R-squared = 0.88
Predicted
Measured
Pyroxene
Regression line
1:1 line
y = 0.91x+1.52
R-squared = 0.69
Predicted
Measured
Plagioclase
Regression line
1:1 line
y = 0.93x+1.89
R-squared = 0.95
Predicted
Measured

Figure 3-7

References

Adams, J. B. (1974), Visible and near-infrared diffuse reflectance spectra of pyroxene as applied to remote sensing of solid objects in the solar system, *J. Geophys. Res*. 79, 4829-4836.

Cahill, J. T. S., P. G. Lucey, and M. A. Wieczorek (2009), Compositional variations of the lunar crust: Results from radiative transfer modeling of central peak spectra, *J. Geophys. Res.-Planets* 114, E09001.

Cahill, J. T. S., and P. G. Lucey (2007), Radiative transfer modeling of lunar highlands spectral classes and relationship to lunar samples, *J. Geophys. Res.-Planets* 112, E10007.

Cahill, J. T. S., P. G. Lucey, K. R. Stockstill-Cahill, and B. R. Hawke (2010), Radiative transfer modeling of near-infrared reflectance of lunar highland and mare soils, *J. Geophys. Res.-Planets* 115, E12013.

Cassidy, W., and B. Hapke (1975), Effects of darkening processes on surfaces of airless bodies, *Icarus* 25, 371-383.

Chapman, C. R. (2004), Space weathering of asteroid surfaces, *Annu. Rev. Earth Planet. Sci*. 32, 539-567.

Clark, B. E., P. Lucey, P. Helfenstein, J. F. Bell lii, C. Peterson, J. Veverka, T. Mcconnochie, M. S. Robinson, B. Bussey, S. L. Murchie, N. I. Izenberg, and C. R. Chapman (2001), Space weathering on Eros: Constraints from albedo and spectral measurements of Psyche crater. *Meteorit. Planet. Sci*. 36, 1617-1637.

Denevi, B. W., P. G. Lucey, and S. B. Sherman (2008), Radiative transfer modeling of near-infrared spectra of lunar mare soils: Theory and measurement, *J. Geophys. Res.-Planets* 113, E02003.

Elkins-Tanton, L. T., J. A. Van Orman, B. H. Hager, and T. L. Grove (2002), Re-examination of the lunar magma ocean cumulate overturn hypothesis: melting or mixing is required, *Earth Planet. Sci. Lett*. 196, 239-249.

Egan, W. G., and T. Hilgeman (1973), Optical constants for terrestrial analogs of lunar materials, *Astron. J*. 78, 799.

Fischer, E. M., and C. M. Pieters (1994), Remote determination of exposure degree and iron concentration of lunar soils using VIS-NIR spectroscopic methods, *Icarus* 111, 475-488.

Ghosh, G. (1998), Handbook of thermal-optical coefficients of optical materials with applications, 325 pp., Elservier, New York.

Gundlach, B., and J. Blum (2013), A new method to determine the grain size of planetary regolith, *Icarus* 223, 479-492.

Guptia, V. and R. R. Ghent (2008), Radar-bright and radar-dark halos around craters on lunar nearside: implications on particle-size distribution of ejecta, *Lunar Planet. Sci*. 39, 1947.

Hapke, B. (1965), Effects of a simulated solar wind on the photometric properties of rocks and powders, *Ann. N. Y. Acad. Sci*. 123, 711-721.

Hapke, B. (1970), Inferences from the optical properties of the moon concerning the nature and evolution of the lunar surface, *Radio Sci*. 5, 293-299.

Hapke, B. (1973), Darkening of silicate rock powders by solar wind sputtering, *The moon* 7, 342-355.

Hapke, B., W. Cassidy and E. Well (1975), Effects of vapor-phase deposition processes on the optical, chemical, and magnetic properties of the lunar regolith, *The moon* 13, 339-353.

Hapke, B. (1981), Bidirectional reflectance spectroscopy: 1. Theory. *J. Geophys. Res.-Solid Earth* 86, 3039-3054.

Hapke, B. (2001), Space weathering from Mercury to the asteroid belt, J. *Geophys. Res.-Planets* 106, 10039-10073.

Hapke, B. (2005), Theory of reflectance and emittance spectroscopy. Cambridge Univ. Press, New York.

Heiken, G. and D. S. McKay (1974), Petrography of Apollo 17 soils, *Proc. Lunar Sci. Conf.* 5, 843-860.

Heiken, G. H., D. T. Vaniman and B. M. French (1992), Lunar Sourcebook - a Users Guide to the Moon. Combridge Univ. Press, New York, 5-25.

Hiesinger, H. and J. W. Head III (2006), New views of lunar geoscience: An introduction and overview, *Rev. Mineral. Geochem*. 60, 1-81.

Isaacson, P. J. et al. (2011), Remote compositional analysis of lunar olivine-rich lithologies with Moon Mineralogy Mapper (M^3) spectra, *J. Geophys. Res.-Planets* 116, E00G11.

James, C. L., S. Letsinger, A. Basu, S. J. Wentworth and D. S. McKay (2002), Size distribution of Fe^0 globules in lunar agglutinitic glass, *Lunar Planet. Sci*. 33, 1827.

James, C. L., S. L. Letsinger, A. Basu, S. J. Wentworth and D. S. McKay (2003), Nanophase iron globules in lunar soils, *Lunar Planet. Sci*. 34, 1992.

Johnson, J. R., S. M. Larson, and R. B. Singer (1991), Remote sensing of potential lunar resources: 1. Near-Side compositional properties, *J. Geophys. Res.-Planets* 96, 18861-18882.

Johnson, P. B. and R. W. Christy (1974), Optical constants of transition metals: Ti, V, Cr, Mn, Fe, Co, Ni, and Pd, *Phys. Rev. B* 9, 5056-5070.

Jolliff, B. L., J. J. Gillis, L. A. Haskin, R. L. Korotev and M. A. Wieczorek (2000), Major lunar crustal terranes: Surface expressions and crust-mantle origins, *J. Geophys. Res.-Planets* 105, 4197-4216.

Keller, L. P. and D. S., Mckay (1993), Discovery of vapor deposits in the Lunar Regolith, *Science* 261, 1305-1307.

Keller, L. P. and D. S. McKay (1997), The nature and origin of rims on lunar soil grains, *Geochim. Cosmochim. Acta* 61, 2331-2341.

Kitamura, R., L. Pilon and M. Jonasz (2007), Optical constants of silica glass from extreme ultraviolet to far infrared at near room temperature, *Appl. Opt.* 46, 8118.

Korokhin, V. V., V. G. Kaydash, Y. G. Shkuratov, D. G. Stankevich and U. Mall (2008), Prognosis of TiO_2 abundance in lunar soil using a non-linear analysis of Clementine and LSCC data, *Planet. Space Sci*. 56, 1063-1078.

Lawrence, S. J. and P. G. Lucey (2007), Radiative transfer mixing models of meteoritic assemblages, *J. Geophys. Res.-Planets* 112, E07005.

Li, L. (2006), Partial least squares modeling to quantify lunar soil composition with hyperspectral reflectance measurements, *J. Geophys. Res.-Planets* 111, E04002.

Li, S. and L. Li (2011), Radiative transfer modeling for quantifying lunar surface minerals, particle size, and submicroscopic metallic Fe, *J. Geophys. Res.-Planets* 116, E09001.

Liu, D., L. Li and Y. Z. Zhang (2013), Sensitivity analysis for Hapke's radiative transfer model, *Lunar Planet. Sci*. 44, 1290.

Liu, D. and L. Li (2015), An empirical approach to estimating mass fraction of submicroscopic iron in lunar soils, *Lunar Planet. Sci*. 46, 2560.

Lucey, P. G. (1998), Model near-infrared optical constants of olivine and pyroxene as a function of iron content, *J. Geophys. Res.-Planets* 103, 1703-1713.

Lucey, P. G. (2004), Mineral maps of the Moon, *Geophys. Res. Lett*. 31, L08701.

Lucey, P. G. and S. K. Noble (2008), Experimental test of a radiative transfer model of the optical effects of space weathering, *Icarus* 197, 348-353.

Lucey, P. G. and M. A. Riner (2011), The optical effects of small iron particles that darken but do not redden: Evidence of intense space weathering on Mercury, *Icarus* 212, 451-462.

Melendrez, D. E., J. R. Johnson, S. M. Larson and R. B. Singer (1994), Remote sensing of potential lunar resources: 2. High spatial resolution mapping of spectral reflectance ratios and implications for nearside mare TiO_2 content, *J. Geophys. Res.-Planets* 99, 5601-5619.

Morris, R. V. (1977), Origin and evolution of the grain-size dependence of the concentration of fine-grained metal in lunar soils: The maturation of lunar soils to a steady-state stage, *Proc. Lunar Sci. Conf*. 8, 3719-3747.

Morris, R. V. (1980), Origins and size distribution of metallic iron particles in the lunar regolith, *Proc. Lunar Sci. Conf*. 11, 1697-1712.

Mustard, J. F. and C. M., Pieters (1987), Quantitative abundance estimates from bidirectional reflectance measurements, *J. Geophys. Res.-Solid Earth* 92, E617-E626.

Mustard, J. F. and C. M. Pieters (1989), Photometric phase functions of common geologic minerals and applications to quantitative analysis of mineral mixture reflectance spectra, *J. Geophys. Res.-Solid Earth* 94, 13619-13634.

Noble, S. K., C. M. Pieters, and L. P. Keller (2007), An experimental approach to understanding the optical effects of space weathering, *Icarus* 192, 629-642.

Noble, S. K., C. M. Pieters, L. A. Taylor, R. V. Morris, C. C. Allen, D. S. McKay and L. P. Keller (2001), The optical properties of the finest fraction of lunar soil: Implications for space weathering, *Meteorit. Planet. Sci*. 36, 31-42.

Ohtake, M. et al. (2009), The global distribution of pure anorthosite on the Moon, *Nature*, 461, 236-240.

Pieters, C. M. (1986), Composition of the lunar highland crust from near-infrared spectroscopy, *Rev. Geophys*. 24, 557-578.

Pieters, C. M., E. M. Fischer, O. Rode and A. Basu (1993), Optical effects of space weathering: The role of the finest fraction, *J. Geophys. Res.-Planets* 98, 20817-20824.

Pieters, C. M., D. G. Stankevich, Y. G. Shkuratov and L. A. Taylor (2002), Statistical analysis of the links among lunar mare soil mineralogy, chemistry, and reflectance spectra, *Icarus* 155, 285-298.

Pieters, C. M., L. A. Taylor, S. K. Noble, L. P. Keller, B. Hapke, R. V. Morris, C. C. Allen, D. S. McKay and S. Wentworth (2000), Space weathering on airless bodies: Resolving a mystery with lunar samples, *Meteorit. Planet. Sci*. 35, 1101-1107.

Presley, M. A. (2002), What can thermal inertia do for you? *Lunar Planet. Sci*. 33, 1144.

Sasaki, S., K. Nakamura, Y. Hamabe, E. Kurahashi and T. Hiroi (2001), Production of iron nanoparticles by laser irradiation in a simulation of lunar-like speca weathering, *Nature* 410, 555-557.

Sasaki, S., T. Hiroi, K. Nakamura, Y. Hamabe, E. Kurahashi and M. Yamada (2002), Simulation of space weathering by nanosecond pulse laser heating: Dependence on mineral composition, weathering trend of asteroids and discovery of nanophase iron particles, *Adv. Space Res*. 29, 783-788.

Shkuratov, Y., L. Starukhina, H. Hoffmann and G. Arnold (1999), A model of spectral albedo of particulate surfaces: Implications for optical properties of the Moon, *Icarus* 137, 235-246.

Shkuratov, Y. G. et al. (2003), Composition of the lunar surface as will be seen from SMART-1: A simulation using Clementine data, *J. Geophys. Res.-Planets* 108, 5020.

Smith, J. V., A. T. Anderson, R. C. Newton, E. J. Olsen, P. J. Wyllie, A. V. Crewe, M. S. Isaacson and D. Johnson (1970), Petrologic history of the moon inferred from petrography, mineralogy, and petrogenesis of Apollo 11 rocks, *Proc. Apollo 11 Lunar Sci. Conf*. 1, 897-925.

Standart, D. L. and J. M. Hurtado (2012), Lunar mineralogy exploration using moon mineralogy mapper (M^3) hyperspectral imagery, *Lunar Planet. Sci*. 43, 2142.

Sunshine, J. M. and C. M. Pieters (1993), Estimating modal abundances from the spectra of natural and laboratory pyroxene mixtures using the modified Gaussian model, *J. Geophys. Res.-Planets* 98, 9075-9087.

Sunshine, J. M., C. M. Pieters and S. F. Pratt (1990), Deconvolution of mineral absorption bands: An improved approach, *J. Geophys. Res.-Solid Earth* 95, 6955-6966.

Taylor, L. A., C. M. Pieters, L. P. Keller, R. V. Morris and D. S. McKay (2001), Lunar mare soils: Space weathering and the major effects of surface-correlated nanophase Fe, *J. Geophys. Res.-Planets* 106, 27985-27999.

Taylor, L. A., C. M. Pieters, R. V. Morris, L. P. Keller, D. S. Mckey, A. Parchen and S. Wentworth (1999), Integration of the chemical and mineralogical characteristics of lunar soils with reflectance spectroscopy, *Lunar Planet. Sci*. 30, 1859.

Taylor, L. A., , C. M. Pieters, A. Patchen, D. S. Taylor, R. V. Morris, L. P. Keller and D. S. Mckay (2010), Mineralogical and chemical characterization of lunar highland soils: Insights into the space weathering of soils on airless bodies, *J. Geophys. Res.-Planets* 115, E02002.

Tompkins, S. and C. M. Pieters (1999), Mineralogy of the lunar crust: Results from Clementine, *Meteorit. Planet. Sci*. 34, 25-41.

Trang, D., P. G. Lucey, J. J. Gillis-Davis, J. T. S. Cahill, R. L. Klima and P. J. Isaacson (2013), Near-infrared optical constants of naturally occurring olivine and synthetic pyroxene as a function of mineral composition, *J. Geophys. Res.-Planets* 118, 708-732.

Tsuboi, N., S. Sugita, T. Hiroi, K. Nagata and M. Okada (2010), A new modified Gaussian model (MGM) using the cross-validation method, *Lunar Planet. Sci*. 41, 1744.

Warell, J. and B. J. R. Davidsson (2010), A Hapke's model implementation for compositional analysis of VNIR spectra of Mercury, *Icarus* 209, 164-178.

Warren, P. H. (1990), Lunar anorthosites and the magma-ocean plgioclase-flotation hypothesis: Importance of FeO enrichment in the parent magma, *Am. Mineral*. 75, 46-58.

Wieczorek, M. A. and R. J. Phillips (2000), The "Procellarum KREEP Terrane": Implications for mare volcanism and lunar evolution, *J. Geophys. Res.-Planets* 105, 20417-20430.

Wilcox, B. B., P. G. Lucey and B. R. Hawke (2006), Radiative transfer modeling of compositions of lunar pyroclastic deposits, *J. Geophys. Res.-Planets* 111, E09001.

Wood, J. A. (1975), Lunar petrogenesis in a well-stirred magma ocean, *Proc. Lunar Sci. Conf.* 6, 1087-1102.

Wu, Y. Z., P. Gong, Q. Liu and A. Chappell (2009), Retrieving photometric properties of desert surfaces in China using the Hapke model and MISR data, *Remote Sens. Environ*. 113, 213-223.

Yan, B., S. Liu, R. Wang, X. Guo and W. Sun (2008), Experiment study in quantitative retrieval of mineral abundances from reflectance spectra, *SPIE* 7123, 712303.

Yan, B., R. Wang, F. Gan and Z. Wang (2010), Minerals mapping of the lunar surface with Clementine UVVIS/NIR data based on spectra unmixing method and Hapke model, *Icarus* 208, 11-19.

Yamamoto, S. et al. (2010), Possible mantle origin of olivine around lunar impact basins detected by SELENE, *Nat. Geosci*. 3, 533-536.

Zisk, S. H., G. H. Pettengill, and G. W. Catuna (1974), High-resolution radar maps of the lunar surface at 3.8cm wavelength, *The Moon* 10, 17-50.

CHAPTER 4

THE FORMATION OF LUNAR SWIRLS: RESULTS FROM HAPKE'S RADIATIVE TRANSFER MODELING

Abstract

The formation of lunar swirls remains an unresolved question in planetary geology literature. Three leading hypotheses have been invoked to explain their formation including the solar wind deflection model, the cometary impact model, and the dust transport model. In this study, each of these hypotheses was tested by fitting measured reflectance data of Moon Mineralogy Mapper (M^3) for both on- and off- swirl surfaces via Hapke's radiative transfer model (RTM). Our results show that the spectral differences between on- and off-swirl surfaces are due to different mass fraction of smaller and larger size submicroscopic metallic iron (SMFe) in lunar soils rather than changing particle size (PS) of soil grains and abundance of plagioclase. On-swirl surfaces have a lower mass fraction of smaller and larger size SMFe than off-swirl surfaces for all the investigated swirl regions (Reiner Gamma, Airy, Firsov, Marginis, and three locations in Ingenii) probably due to magnetic field shielding from solar wind ions implantation. The solar wind deflection model is the likely mechanism for the formation of lunar swirls, while the cometary impact and the dust transport models are not supported by our results. The validity of the solar wind deflection model in accounting for the formation of lunar swirls also indicates that the solar wind ions implantation is the main mechanism of space weathering instead of micrometeoroid bombardment.

1. Introduction

Lunar swirls are bright curvilinear markings in both highlands and maria on the lunar surface (*Schultz and Srnka*, 1980; *Hood and Williams*, 1989; *Blewett et al*., 2011). All of the identified lunar swirls show higher albedo than the surrounding areas (*Hood and Schubert*, 1980; *Hood and Williams*, 1989; *Kramer et al*., 2011a, b) and are coincident with regions possessing high magnetic field strength. While lunar swirls are not associated with a distinct topography or morphology (*Bell and Hawke*, 1981; *Richmond et al*., 2005; *Blewett et al*., 2011; *Neish et al*., 2011), they are important natural laboratories where space weathering and crustal magnetism intersect (*Hemingway and Garrick-Bethell*, 2012). Studying lunar swirls could help understand the relative importance of solar wind implantation and micrometeorite bombardment on space weathering, and the origin of lunar surface magnetic field (*Blewett et al*., 2011; *Garrick-Bethell et al*., 2015). In addition, lunar swirls are excellent mission targets to investigate the production and distribution of OH^-/H_2O over the lunar surface (*Garrick-Bethell et al*., 2015; *Pieters and Garrick-Bethell*, 2015).

The formation of lunar swirls has been an outstanding puzzle to lunar geoscientists. The leading hypotheses for the origin of lunar swirls are the solar wind deflection model, the cometary impact model, and the dust transport model (*Hood and Schubert*, 1980; *Schultz and Srnka*, 1980; *Hood and Williams*, 1989; *Pinet et al*., 2000; *Garrick-Bethell et al*., 2011). The solar wind deflection model suggests that the formation of lunar swirls results from atypical space weathering in which the magnetic anomaly shields the lunar surface from the solar wind ions bombardment (*Hood and Schubert*, 1980; *Hood and Williams*, 1989; *Richmond et al*., 2003). Space weathering, which is referred to as any

modification processes that act on an airless planetary body, changes the physical, chemical and optical properties of its surface materials (*McCord and Adams*, 1973; *Pieters et al*., 1993). It mainly involves continuous bombardment of solar wind ions and micrometeorites (*Hapke*, 1965; *Hapke et al*., 1970; *Pieters et al*.,1993, 2000; *Noble et al*., 2001, 2007; *Lucey and Noble*, 2008). Materials generated from solar wind sputtering and micrometeorite vaporization can grow and form thin amorphous rims on the surface of lunar soil grains, and Fe^{2+} in lunar soils is reduced to submicroscopic metallic iron (SMFe) residing in the rims (*Hapke et al*., 1975; *Cassidy and Hapke*, 1975; *Keller and Mckay*, 1993, 1997). With a longer exposure time to the space environment, fresh lunar soils are expected to be weathered and gradually mature with increasing SMFe. Compared to fresh lunar soils, mature lunar surfaces exhibit low spectral reflectance in the visible to near-infrared spectral region (darkening), develop a red slope continuum (reddening), and show subdued mineral absorption bands (*Hapke*, 1973, 2001; *Cassidy and Hapke*, 1975; *Fischer and Pieters*, 1994). The solar wind deflection model uses magnetic anomalies to explain high albedo on-swirl surfaces and low albedo off-swirl surfaces. Because of the deflection effect of lunar magnetic anomalies, a lesser amount of SMFe is generated in on-swirl regions because of a reduced solar wind flux, resulting in higher albedo of the lunar on-swirl regions than off-swirl regions to which solar wind ions are deflected to and a higher amount SMFe is generated (*Blewett et al*., 2011). Indeed, this model is consistent with the observations that on-swirl spectra show partial reddening with low degree darkening due to retarded space weathering, and off-swirl spectra exhibit only darkening with little or no reddening because of accelerated space weathering (*Kramer et al*., 2011a, b). The dark and relatively flat off-swirl spectra can be explained by the presence of larger size SMFe via

coalescence of excess smaller size SMFe in off-swirl regions produced by enhanced implantation of solar wind fluxes. *Blewett et al*. (2011) observed a slightly lower FeO content in on-swirl regions than off-swirl regions, and attributed this FeO difference to a lack of larger size SMFe and a decreased amount of smaller size SMFe in on-swirl regions as a result of anomalous space weathering (little darkening with limited reddening). Although these studies support the solar wind deflection model, they are merely a speculation for which no quantitative analysis has been conducted on the measured reflectance spectra to confirm the enrichment of SMFe in off-swirl regions relative to on-swirl regions. In addition, *Starukhina and Shkuratov* (2004) pointed out that the intensity of magnetic field above the lunar surface might not be so strong as to deflect implanted solar wind flux efficiently, which could still result in the maturation of lunar soils in on-swirl regions. Furthermore, newly emplaced materials in on-swirl regions, though protected by magnetic field, may eventually reach a state of background maturity after exposure of billion years to space environment. Even in regions with strong magnetic anomalies, swirls would fade away if they have not received any fresh materials (*Garrick-Bethell et al*., 2011).

Another hypothesis is the cometary impact model stating that gas and dust from the coma stripe away the mature, dark and fine fraction of lunar surface soils, redeposit them in the surrounding areas and expose fresh underlying unweathered lunar soils (*Schultz and Srnka*, 1980; *Bell and Hawke*, 1987; *Pinet et al*., 2000). The observed sinuous features of lunar swirls are the remnant manifestation of the coma's turbulent flow of gas and dust. It is suggested that the cometary impact process could create magnetic anomalies associated with swirls (*Schultz and Srnka*, 1980). Thermal remanence can be created when the near-

surface materials are heated above the Curie temperature by hypervelocity gas collisions and microimpacts in the presence of the ambient field (*Schultz and Srnka*, 1980; *Kramer et al*., 2011a). According to this hypothesis, on-swirl surfaces with exposure of underlying fresh soils should have a lower mass fraction of SMFe but larger PS of soil grains than relatively mature off-swirl surfaces. This hypothesis was strongly supported by *Pinet et al*. (2000), who compared multispectral data acquired for on-swirl regions with laboratory spectra of lunar soils of different particle sizes and concluded that on-swirl regions should have a relatively larger particle size than their surrounding areas. However, their work was limited by the spectral resolution of the multispectral data, which could miss important spectral features of on-swirl surfaces and lead to a misinterpretation of the formation of lunar swirls. Another limitation to the cometary impact model is that it fails to explain why lunar swirls are mainly found antipodal to the large impact basin (*Kramer et al*., 2011a, b).

Recently, a dust transport model was proposed by *Garrick-Bethell et al.* (2011) to explain the origin of lunar swirls. In this model, an electrostatic potential could be generated at magnetic anomaly as implanted solar wind protons penetrate more deeply into the magnetic field than electrons. This electrostatic potential can attract electrically charged finest lunar soils, which are enriched in plagioclase and have been lofted above the surface during terminator crossings (*Criswell*, 1972; *Zook et al*., 1995). The swirls are formed as a result of the accumulation of abundant bright fine sized plagioclase. The spectral difference between on- and off- swirl surfaces is explained by different abundances of plagioclase and soil grain PS. However, few attempts have been made to determine whether the spectral and maturity trend observed at lunar swirls can be adequately characterized by accumulation of fine sized plagioclase.

The fundamental difference among these three hypotheses lies in how to explain the observed spectral differences between on- and off- swirl surfaces and what factors such as maturity of lunar soils (mass fraction of SMFe), soil grain PS, and composition (abundance of plagioclase) contribute most to this difference. The main goal of this study is to determine which of these hypothesis is plausible. To achieve this goal, an effective method is needed to quantitatively determine and compare the contributions of these factors to driving the spectral difference between on- and off-swirl regions. Hapke's radiative transfer model (RTM) can meet this need and is used in this study. Hapke's RTM has been widely used in simulating the measured reflectance spectra of the lunar surface and proved as an effective method in evaluating the physical and compositional properties of lunar soils (*Mustard and Pieters*, 1987, 1989; *Lucey, 2004*; *Cahill and Lucey*, 2007; *Denevi et al.*, 2008; *Cahill et al.*, 2009, 2010).

2. Study Areas and Dataset Preprocessing

Five lunar swirls in both highland and mare regions were investigated in this study, including Reiner Gamma, Airy, Firsov, Marginis, and Ingenii (Fig. 4-1a to Fig. 4-5a). Their geological settings, magnetic field strength, and locations are shown in Table 4-1. The shape of these swirls varies between diffuse patches and sinuous curves, and some of them (e.g., Reiner Gamma and Airy) exhibit 'dark lanes' which are low albedo regions that interweave with brighter features of swirls. The estimated magnetic field strength at 30-km altitude for these swirls ranges from 6 nT (weak) to 22 nT (strong) (*Blewette et al*., 2011). The datasets used in this study were M^3 L2 (lever 2) reflectance images acquired in the global mode at a spatial resolution of 140 m and spectral resolutions 20-40 nm. These reflectance data covering the central portion of these five swirl regions were first smoothed

using a moving window average for noise reduction (*Sun and Li*, 2014), and spectral bands between 540 nm and 2497 nm were retained to avoid thermal effects and preserve diagnostic absorptions of mafic minerals for further analysis. These bands were then corrected by multiplying the spectral bands with the coefficients, which were derived through dividing the lab measured reflectance spectrum of lunar sample 62231 by corresponding image spectrum in M^3 data at each wavelength.

[Insert Table 4-1 here]

3. Method

3.1. Hapke's Radiative Transfer Model

In order to explore the formation of lunar swirls, we applied a radiative transfer model to the remotely obtained M^3 image spectra of both on- and off-swirl surfaces. The RTM used here is based on the work of *Hapke* (1981, 2001, 2005), which can reproduce measured reflectance spectra of lunar soils by incorporating the abundance, refractive index and PS of end-member components that make up lunar soils, and the degree of space weathering (SMFe) as factors. In general, Hapke's RTM uses the real (*n*) and (*k*) imaginary parts of refractive index of each end-member component to calculate its single scattering albedo (SSA) (the probability of a photon survives an encounter with a material) at a specified PS and a desired level of maturity (express as mass fraction of SMFe). Once the SSA of each end-member component is determined, the average SSA of mineral mixtures can be evaluated by adding SSA of end-member components linearly in proportion to their abundances. This average SSA is then used in conjunction with phase function and backscattering function to calculate reflectance spectra of lunar soils at specified incidence and emission angles. A simplified description of Hapke's RTM can be found in *Lucey*

(1998) and *Li and Li* (2011). One important step in computing reflectance spectra of lunar soils with Hapke's RTM is incorporating the effect of space weathering. *Hapke* (2001) described the optical effect of SMFe which plays an important role in lunar space weathering using the following equation:

$$\alpha = \frac{4\pi n_h k_h}{\lambda} + \frac{36\pi z M_c \rho_h}{\lambda \rho_{Fe}}. \quad (1)$$

Here, α is the absorption coefficient of an end-member component. n and k are real and imaginary parts of the refractive index respectively and ρ is solid density. These three parameters are associated with the host mineral and SMFe by the suffixes h and Fe, respectively. M_c is the mass fraction of SMFe residing in the rim of a soil grain and λ is wavelength. z is a parameter defined by the refractive index of host mineral and *Fe*. The first term on the right side of Eq. 1 represents absorption by a host end-member component and the second term describes the amount of light absorbed by SMFe imbedded within the rims of the host end-member component.

3.2. Testing the Solar Wind Deflection Model

The basic assumption of the solar wind deflection model is that off-swirl surfaces should possess higher mass fractions of both smaller and larger size SMFe than on-swirl surfaces because the deflection of enhanced solar wind flux from on-swirl to off-swirl surfaces accelerates the reduction of Fe^{2+} in lunar soils. The observed spectral difference between on- and off-swirl surfaces should be driven by mass fractions of smaller and larger size SMFe rather than the abundance of plagioclase or PS of lunar soil grains. Therefore, in this study, Hapke's RTM was used to test whether the measured on- and off-swirl spectra can be fitted by changing the mass fraction of both smaller and larger size SMFe and

whether off-swirl surfaces are indeed enriched in smaller and larger size SMFe as the solar wind deflection model assumed.

The original equation (Eq. 1) in Hapke's RTM describing space weathering effects can be only used to estimate the mass fraction of smaller size SMFe in lunar soil grains that redden and darken reflectance spectra of lunar soils. It cannot be used to estimate the mass fraction of larger size SMFe in the interior of soil grains that mainly darken the host materials (*Nobel et al*., 2007; *Lucey*, 2008; *Liu et al*., 2015). Estimating the mass fractions of smaller and larger size SMFe requires a model that is capable of accommodating both smaller and larger size SMFe effects. *Lucey and Riner* (2011) proposed a new model to account for the reddening and darkening effects of smaller size SMFe and the darkening effect of larger size SMFe on the absorption of lunar soils. The model is shown in Eq. 2:

$$\alpha = \frac{4\pi n_h k_h}{\lambda} + \frac{36\pi z M_c \rho_h}{\lambda \rho_{Fe}} + \frac{3 q_a M_{in} \rho_h}{d_{Fe} \rho_{Fe}}, \quad (2)$$

where M_c and M_i are the mass fraction of smaller and larger size SMFe in lunar soils, respectively. q_a is the absorption efficiency of an SMFe particle, which can be calculated through Mie theory. d_{Fe} is particle size of larger size SMFe. The first two terms on the right side of Eq. 2 are the same as those in the original Hapke's RTM representing the absorption of light due to host soil particles and smaller size SMFe in the rims of soil grains. The new modification is the third term on the right side of Eq. 2 for accounting for the absorption of light due to larger size SMFe in the interior of soil grains. Combining Eq. 2 with other equations in Hapke's model, *Liu et al*. (2015) demonstrated the effectiveness of this new model in accommodating space weathering effects. Thus, Eq. 2 instead of Eq. 1 was used to test the solar wind deflection model in this study.

The solar wind deflection model assumes that there is no difference between on- and off-swirl surfaces in major mineralogy and composition. Therefore, the abundance of end-member components is not required in the modeling process when testing the solar wind deflection model because the mixture of different minerals making up the lunar soils was treated as an average bulk lunar soil. In addition, because refractive index (n_h and k_h) of host lunar soils are only determined by their composition and mineralogy and the host lunar soils was assumed to be as a bulk, only one set of refractive index was used in the modeling process for the bulk host soils of both on- and off-swirl surfaces. Refractive indices for end-member components making up the host lunar soils are not required. The reflectance spectra for on- and off-swirl regions are controlled by this set of refractive index of bulk host soils, PS of soil grains, and the mass fraction of smaller and larger size SMFe.

Estimating the mass fraction of smaller and larger size SMFe for on- and off-swirl regions requires calculating particle size of soil grains, n_h and k_h of host bulk soils in Eq. 2. In this study, n_h was assumed to be 1.6 for all the wavelength (*Shkuratov et al.*, 1999), and PS of soil grains was assigned as 15 μm for both on- and off-swirl surfaces which is the mean value for the size range 10 μm – 20 μm that dominants the spectral characteristics of bulk lunar soils (*Pieters et al*., 1993). The only parameter requires calculation is k_h of host bulk soil. According to the solar wind deflection model, k_h should be the same for both on- and off-swirl host bulk soils because of their similar mineralogy and composition. The spectral difference between on- and off-swirl regions is mainly controlled by varying mass fraction of SMFe rather than compositional difference of host bulk soils. To derive k_h of host bulk soils, the spectra of fresh craters shown in Fig. 4-1a to Fig. 4-4a and Fig. 4-5b to 4-5d were extracted following the method of *Kramer et al*. (2011b). These fresh

crater spectra possibly represent newly exposed materials containing little or no SMFe, and their spectra are mainly controlled by k_h of host bulk soils. The averaged spectrum of the selected fresh craters was fitted with Hapke's model (using Eq. 2 in this work and Eqs. 1-7 in *Li and Li*, 2011) by adjusting k_h only and assuming the mass fraction of both smaller and larger SMFe to be zero. The k_h spectrum was derived when the difference between the original average image spectrum and the optimal fitting spectrum was minimized. After this step, a similar procedure was repeated to fit the spectrum of each pixel in the image by varying the mass fraction of smaller and larger SMFe and applying derived k_h for host bulk lunar soils. The solar wind deflection model was tested for all the five swirl regions listed in Table 4-1.

3.3. Testing the Cometary Impact Model

The basic assumption of the cometary impact model is that lunar soil composition is similar between on- and off-swirl regions, but the spectral difference between on- and off-swirl surfaces is attributed to the variation of PS of soil grains and mass fraction of SMFe (*Schultz and Srnka,* 1980; *Pinet et al.,* 2000). This model does not distinguish the smaller and larger size SMFe in lunar soils. The observed higher optical maturity of off-swirl regions relative to on-swirl regions is primarily due to higher mass fractions of smaller size SMFe, and larger size SMFe is not considered in this model (*Pinet et al*., 2000). Furthermore, on-swirl surfaces should have a larger PS and a lesser amount of smaller size SMFe than off-swirl surfaces because of shorter period exposure of underlying large size lunar soils. In this study, the cometary impact model was mainly tested for the swirl in Reiner Gamma. Plagioclase and pyroxene were considered to be the major minerals making up the soils of this region according to previous work by *Bell and Hawke*, (1987).

To evaluate the PS of soil grains and mass fraction of SMFe in on- and off-swirl regions using Hapke's RTM, refractive indices of plagioclase and pyroxene were first obtained following the method of *Li and Li* (2011) on the basis of the selected spectra of plagioclase and pyroxene from RELAB. Then, an averaged spectrum (Fig. 4-6a) was calculated separately for the selected areas corresponding to on- and off-swirl regions (red and green boxes in Fig. 4-6b). Next, we derived mass fractions of SMFe, PS of soil grains, and abundances of plagioclase and pyroxene through fitting the averaged on-swirl spectrum (red box in Fig. 4-6b) using Hapke's model. In this process, Eq. 1 was used to describe effects of smaller size SMFe without consideration of larger size SMFe. Using derived PS and SMFe for the averaged on-swirl spectrum, we investigated whether the averaged off-swirl spectrum (green box in Fig. 4-6b) could be fitted by decreasing PS and increasing SMFe. In addition, Hapke's model was also employed to fit each spectrum of the image by adjusting SMFe and PS but using the abundance of plagioclase and pyroxene that were obtained from fitting the averaged on-swirl spectrum. We aimed at exploring whether the measured spectra for on- and off-swirl regions could be fitted by changing PS of soil grains and mass fraction of smaller size SMFe, and whether off-swirl regions have soil grains of a smaller PS but more enriched in SMFe than on-swirl regions.

3.4. Testing the Dust Transport Model

The basic assumption of this model is that on-swirl surfaces should have soil grains of smaller PS but higher abundance of plagioclase than off-swirl surfaces as a result of the accumulation of fine dust grains enriched in plagioclase. There is no variation in the mass fraction of SMFe between on- and off-swirl lunar soils. The spectral difference between on- and off-swirl regions should be accounted for by different abundance of plagioclase

and PS of soil grains rather than the variation of lunar soil maturity (mass fraction of SMFe). Because larger size SMFe was not taken into account in the dust transport model, only the space weathering effect by smaller size SMFe needs to be considered and Eq. 1 was used in Hapke's model.

The fitting process for testing the cometary impact model was repeated to test the dust transport model for the Reiner Gamma Swirl. However, PS of soil grains and the abundance of plagioclase were allowed to float to fit the averaged off-swirl spectrum this time, but the mass fraction of SMFe was derived from fitting the averaged on-swirl spectrum and fixed for this model test process. Again, each spectrum of the image was fitted by varying the abundance of plagioclase and PS of soil grains, but fixing the mass fraction of SMFe. We aimed at examining whether the averaged off-swirl spectrum can be reproduced by increasing PS of soil grains and decreasing the abundance of plagioclase, and whether off-swirl regions have a larger PS of soil grains but a less amount of plagioclase than on-swirl regions.

[Insert Figure 4-1 here]

[Insert Figure 4-2 here]

[Insert Figure 4-3 here]

[Insert Figure 4-4 here]

[Insert Figure 4-5 here]

4. Results and Discussion

4.1. The Solar Wind Deflection Model

Shown in Fig. 4-1b to Fig. 4-4b, Fig. 4-5e to 4-5g and Fig. 4-1c to Fig. 4-4c, Fig. 4-5h to 4-5j are the mass fraction of smaller and larger size SMFe derived respectively for the

five investigated swirl regions with Hapke's model. All these maps show that the off-swirl surfaces evidently possess higher mass fraction of both smaller and larger size SMFe than the on-swirl surfaces. The dark lanes (Fig. 4-1b, c and Fig. 4-2b, c) that wind within the on-swirls are clearly delineated with abundant SMFe. Hapke's model parameterized in the context of the solar wind deflection model yielded a good fit to image spectra for the on- and off-swirl soils and fresh craters in all the five swirl regions (Fig. 4-1d to Fig. 4-4d and Fig. 4-5k to 4-5m). The root mean square error (RMSE) between measured and fitting spectra, when averaged for the whole scene is 0.007, 0.004, 0.007, 0.005 and 0.005 respectively for Reiner Gamma, Airy, Firsov, Marginis, and Ingenii. These results suggest that the spectral difference between on- and off-swirl regions could be ascribed to a less amount of smaller and larger size SMFe in on-swirl regions than off-swirl regions. Off-swirl regions are indeed enriched in both smaller and larger size SMFe as postulated by *Kramer et al*. (2011a, b) and *Blewett et al*. (2011). This SMFe enrichment in off-swirl regions can be explained by the interaction of the solar wind with the magnetic anomaly in lunar swirl regions.

Magnetohydrodynamic simulation has indicated that the interaction of the solar wind with lunar magnetic anomalies can generate a mini-magnetosphere above these strong magnetic anomalies which significantly deflects the incoming solar wind ions and produces local shield areas at the lunar surface (*Harnett and Winglee,* 2002). The shielding effect of magnetic anomalies, causes fewer solar wind ions, especially H^+ to penetrate into on-swirl regions and less Fe^{2+} to be reduced and sputtered to form smaller size SMFe. Although the necessity of implanted H^+ for reduction of Fe^{2+} remains debated, a number of studies have shown an correlation between the mass fraction of SMFe and hydrogen content (*Clark*,

2009; *Pieters et al*., 2009; *Wieser et al*., 2010), indicating this correlation could be a causal process (*Kramer et al*., 2011a, b). A less amount of smaller size SMFe in lunar soils in the shielded on-swirl surfaces also limits the formation of larger size SMFe via impact melting (*Blewett et al*., 2011). In contrast, the deflection of implanted H^+ onto off-swirl surfaces by magnetic anomalies can result in H^+ saturated off-swirl soils, which facilitate the reduction of Fe^{2+} in micrometeoroid impact events, and promote generation of smaller size SMFe and OH^- (*Kramer et al*., 2011a, b). A higher amount of smaller size SMFe also enhances the possibility of building up of larger size SMFe via the impact coalescence. Examining the 2.82 μm absorption of M^3 data for lunar swirl regions has demonstrated the enrichment of OH^- in off-swirl regions (*Kramer et al*., 2011b; *Pieters et al*., 2015).

The solar wind deflection model for the formation of lunar swirls has gained evidence from the observations made using Lunar Prospector magnetometer data and Clementine reflectance mosaics (*Hemingway and Garrick-Bethell*, 2012), and can be used to explain lunar swirl appearance. *Hemingway and Garrick-Bethell* (2012) interpreted that the bright regions at Reiner Gamma correlated with dominantly a horizontal magnetic field, and that the intra-swirl dark lanes at Airy were associated with a vertical magnetic field. On one hand, the dark lanes in Airy corresponding to the vertical dipole field would experience a weak deflection to implanted solar wind ions, but an enhanced solar wind flux. As a result, the dark lanes would have an increased amount of SMFe but show substantially low reflectance. The same interpretation is applicable to the observed dark lanes in Reiner Gamma. Their Lunar Prospector – and Clementine - based findings are consistent with our modeling results showing an increased amount of SMFe in both the dark lanes and off-swirl regions for Reiner Gamma and Airy (Fig. 4-1c and 4-2c). As seen from the Fig. 4-1

to Fig. 4-5, Reiner Gamma and Ingenii not only demonstrate higher mass fraction of both smaller and larger size SMFe but also have stronger magnetic field than other three swirls (Table 4-1) (*Blewett et al.*, 2011). Analysis of the returned lunar samples confirmed that SMFe is the main ferromagnetic carrier in lunar materials (*Fuller and Cisowski*, 1987; *Richmond et al*., 2003). Therefore, it is plausible that higher mass fraction of SMFe in lunar soils can explain why some swirl regions are more magnetic than others (*Richmond et al*., 2003).

4.2. The Cometary Impact Model

Shown in Fig. 4-6a are the fitting results for the averaged on- and off-swirl spectra of Reiner Gamma. We can see that the averaged off-swirl spectrum cannot be accurately fitted by decreasing PS and increasing mass fraction of SMFe. An apparent misfit was present between the fitting and the original on-swirl spectrum even when setting SMFe, PS, and abundance of plagioclase as free parameters in Hapke's modeling process (Dashed and dotted white lines in Fig. 4-6a). The off-swirl surface shows no evident enrichment in SMFe and was determined to have an apparently larger PS than the on-swirl surface (Fig. 4-7a, b), which contradicts to the assumptions for the cometary impact model.

Starukhina and Shkuratov (2004) proposed a meteoroid swarm model alternative to the cometary impact model to explain the swirl formation. This model states that meteoroid swarms made of compact cometary nucleus can plow lunar soils and generate projectiles to bring immature materials from depth to top lunar surface. The collisions between regolith particles in ejecta produced by projectiles may reduce the average PS and yield a dust component that subsequently accumulates onto on-swirl surfaces (*Shkuratov et al*., 2010). Although our result showing a smaller PS and a slightly lower mass fraction of

SMFe in on-swirl regions is consistent with the assumption for meteoroid swarms model, the poor model fit to measured image spectra for on- and off-swirl soils (Fig. 4-7c) reflects that the spectral difference between on- and off-swirl surfaces cannot be ascribed to the variation in PS and mass fraction SMFe in lunar soils. Based on the derived spatial distribution of mass fractions of SMFe, soil grain PS, and the poor agreement between the fitting and measured image spectra, neither the cometary impact nor the meteoroid swarm model seems to be a valid hypothesis for the formation of lunar swirls.

Other studies also indicate difficulties of using the cometary impact model to account for the formation of lunar swirls. On the basis of OMAT values derived from Clementine data, *Kramer et al*. (2011a) counted the number of small fresh craters that are younger than the swirl surfaces for both on- and off-swirl regions, and found that the crater density in off-swirl regions is less than that in on-swirl regions. This observation rules out the plausibility of recent cometary impact model in explaining the formation of lunar swirls. If lunar swirls are generated through a recent cometary impact, then the subsequently small immature craters would be randomly distributed and there should be approximately equal crater densities for on- and off-swirl surfaces. However, the different crater densities between on- and off-swirl regions can be explained using the solar wind deflection model because the small fresh craters in off-swirl regions could fade away without implanting solar wind being blocked. In addition, the surface of Mercury is predicted to be more frequently impacted by comets than the surface of the Moon (*Gold and Soter*, 1976). A greater number of swirls should be observed on the Mercury than on the Moon if swirls are formed by comet impacts. However, images from MESSENGER spacecraft show no

examples of lunar-like swirls on the surface of the Mercury (*Blewett et al*., 2010). Therefore, the cometary impact model for the formation of lunar swirls is not preferred.

[Insert Figure 4-6 here]

[Insert Figure 4-7 here]

4.3. The Dust Transport Model

Fig. 4-8a clearly reveals that the averaged off-swirl spectrum cannot be reproduced by increasing PS and decreasing abundance of plagioclase as the dust transport model assumed. Although the off-swirl surface shows larger PS than the on-swirl surface (Fig. 4-9a), a less amount of plagioclase is not required for fitting the spectra of the off-swirl surface. Instead, an opposite trend was obtained (Fig. 4-9b) and violates the basic assumptions of the dust transport model. The measured image spectra do not correlate well with the fitting spectra (Fig. 4-9c) and the spectral differences between on- and off-swirl surfaces are not due to varying PS and plagioclase abundance across the lunar surface. Our modeling results indicate that the dust transport model is not favorable to explain the formation of lunar swirls.

Moreover, the dust transport model attributes the brightness of on-swirl soils to the accumulation of fine lunar soils enriched in plagioclase. However, the finest fraction of lunar soils is not only dominated by higher abundance of plagioclase but also contains high mass fractions of SMFe. Many investigations have demonstrated that the mass fraction of SMFe increases substantially with decreasing PS of lunar soil grains (*Pieters et al*., 2000; *Taylor et al*., 2001, 2010; *Liu et al*., 2015). The spectral characteristics we identified as maturity (reddening, darkening, and subdued spectral contrast) are mainly due to the generation of SMFe. The more SMFe present in a lunar soil, the more spectrally mature it

appears (*Pieters et al*., 1993; *Taylor et al*., 2001; *Kramer et al*., 2011b). Accumulation of the finest fraction of lunar soils onto on-swirl surfaces would be inevitably accompanied by a larger amount of SMFe involved in lunar soils. This could make the swirl look mature, contradicting to the observed immature nature of on-swirl lunar soils. Another line of evidence being opposed to the dust transport model is that the Christiansen Feature (CF) position recently derived from the Diviner data for Reiner Gamma is found to shift slightly toward a shorter wavelength (*Glotch et al*., 2012). This was interpreted as the retarded space weathering rather than changing abundance of plagioclase (*Lucey et al.*, 2010, 2013; *Glotch et al*., 2012).

[Insert Figure 4-8 here]

[Insert Figure 4-9 here]

4.4. Other Evidence Supporting the Solar Wind Deflection Model

In addition to the results described in sections 4.1 – 4.3, several other lines of evidence resulting from other studies also support the solar wind deflection model. *Glotch et al*. (2012) created a temperature image for Reiner Gamma using Diviner night-time data. If the PS of on-swirl regions shows a larger deviation from the PS of surrounding off-swirl regions, a significant night-time temperature anomaly would be expected. However, their result shows that no temperature anomaly is associated with on-swirl surfaces. This contradicts to the assumptions of both the cometary impact model and the dust transport model, which associate the albedo difference between on- and off-swirl surfaces with changing PS of soil grains. *Hemingway and Garrick-Bethell*. (2014) explored how space weathering effects vary from low to high lunar latitudes and from off-swirl to on-swirl surfaces. They found that the trend of spectral variation from low to high lunar latitude,

where both solar wind and micrometeoroid flux are reduced, is consistent with the spectral trend from off-swirl surfaces to on-swirl surfaces, where micrometeoroid flux is unaffected, but solar wind flux is likely reduced. These two trends are related to a reduction of solar wind flux, indicating the formation of lunar swirls should be associated with shielding by magnetic anomalies. Variations in PS of lunar soil grains and abundance of plagioclase cannot yield such a trend, and thus lunar swirls are not expected to be formed by the cometary impact or dust transport process. By examining the data obtained from the Sub-keV Atom Reflecting Analyzer (SARA) instrument on the Chandrayaan-1, *Wieser et al.* (2010) found that there is a reduced neutral hydrogen emission from on-swirl regions and an enhanced emission of hydrogen from off-swirl regions. Since the backscattered hydrogen flux is proportional to the implanting proton flux, the reduced hydrogen emission detected for on-swirl surfaces should be attributed to the magnetic fields above swirl surfaces which shield the surface from impinging of solar wind (*Futaana et al*., 2006).

4.5. Solar Wind Implantation versus Micrometeorite Bombardment

Elucidating the formation of lunar swirls is critical for understanding dominant mechanism of space weathering (*Blewette et al*., 2011; *Pieters and Garrick-Bethell*, 2015; *Garrick-Bethell et al*., 2015). Both solar wind ion implantation and micrometeoroid bombardment can produce SMFe that leads to optically maturation of lunar surface materials. It is still widely debated on which process is the dominant mechanism of space weathering (*Pieters et al*., 2000; *Hapke, 2001*; *Hiroi et al*., 2006; *Vernazza et al*., 2009). Our results from Hapke's radiative transfer modeling strongly support the solar wind deflection model to be responsible for the swirl formation. The on-swirl regions in reality have lower mass fractions of both smaller and larger size SMFe than off-swirl regions due

to the shielding effect of the swirl magnetic field. The difference between on- and off-swirl surfaces in the mass fraction of SMFe accounting for the spectral differences does suggest that solar wind ion implantation should be the major mechanism of space weathering because micrometeoroids, even if acquiring significant charges, would have too small charge-to-mass ratios to be deflected by the magnetic field (*Fechtig et al*., 1979). The micrometeoroid impact would be evenly distributed on the lunar surface and the same amount of Fe^{2+} would be reduced in on- and off-swirl regions. Therefore, the difference between on- and off-swirl regions in larger and smaller SMFe mass fractions would not exist.

4.6. Relations of Lunar Swirls to Magnetics Field and Volatiles

The results from this study have important implications for the origin of lunar surface magnetic fields. One argument states that the origin of lunar surface magnetic anomalies relates to the formation of large impact basins (*Hood and Huang*, 1991; *Hood and Artemieva*, 2008), which is based on the observation that many magnetic anomalies are found antipodal to major impact basins (*Lin et al*., 1988; *Hood et al*., 2001; *Richmond et al*., 2005). An alternative explanation is that the magnetic fields on the lunar surface result from recent cometary impacts (*Schultz and Srnka*, 1980). All the observed lunar swirls are coincident with magnetic anomalies. The validity of the cometary impact model would argue for a cometary impact origin for the lunar surface magnetic field rather than the basin formation events (*Schultz and Srnka*, 1980). The lunar swirls that are found antipodal to the large impact basin could just be due to incomplete mapping of swirl locations (*Kramer et al*., 2011a, b). However, our results demonstrate the feasibility of the solar wind deflection model rather than the cometary impact model for explaining the formation of

lunar swirls, which rules out the plausibility that lunar surface magnetic fields are produced by recent cometary impact.

The abundant SMFe in off-swirl regions has been confirmed by this study. The association of these regions to the observed enrichment of OH^-/H_2O in off-swirl regions from M^3 data (*Kramer et al*., 2011b; *Pieters et al*., 2015) indicates the plausibility of this chemical reduction process in which the incident H^+ can break Fe-O bond and react with O forming OH and reducing Fe (*Kramer et al*., 2011a). Moreover, the correlation between SMFe and OH^-/H_2O might give rise to the possibility of using higher mass fraction of SMFe to locate lunar surface areas with OH^-/H_2O.

4.7. Limitations of Hapke's RTM in Exploring the Formation of Lunar swirls

One limitation of the solar wind deflection model is that it cannot explain the anomalous photometric properties of lunar swirls (*Kreslavsky and Shkuratov*, 2003; *Chevrel et al*., 2006; *Kaydash et al*., 2009; *Shkuratove et al*., 2010). The photometric properties of a regolith have generally been linked to the properties of a surface's microtexture such as porosity and roughness (*Hapke*, 1993). For example, a greater degree of sub-resolution roughness than the surroundings has been invoked to interpret the photometric anomaly of Reiner Gamma (*Shkuratove et al*., 2010). However, these physical properties of regolith (e.g. porosity and roughness) have not been accommodated in Hapke's RTM. Incorporating the physical properties of regolith into Hapke's RTM is necessary in future studies on the formation of lunar swirls. While the results from Hapke's RTM support for the solar wind implantation hypothesis, it cannot be used to address the questions such as whether the intensity of magnetic field is strong enough to deflect the implanted solar wind flux entirely from swirl surfaces (*Starukhina and Shkuratov*, 2004)

or whether sufficient recent refreshing ejecta deposition is required to protect lunar swirls from fading away after billions years' exposure to space environment (*Blewett et al*., 2011, *Garrick-Bethell et al*., 2011). To ultimately confirm the validity of solar wind deflection model in accounting for the formation of lunar swirls, investigations including development of accurate model for calculating lunar surface magnetic field from orbital measurement, lab experiment on the efficiency of solar wind ions deflection by magnetic field, and the rate of maturation of lunar soils versus input of fresh ejecta by lateral transport should be conducted in conjunction with Hapek's RTM.

5. Conclusions and Future Work

Through fitting measured reflectance spectra of lunar swirls via Hapke's RTM, we have shown that the spectral difference between on- and off-swirl surfaces are fully explained by changing the mass fraction of both smaller and larger size SMFe in lunar soils rather than the variation in PS of soil grains and mineral abundance of plagioclase. On-swirl surfaces are indeed deficient in smaller and larger size SMFe relative to off-swirl surfaces because of protection from impinging solar wind ions. Therefore, the solar wind deflection model is appropriate to explain the formation of lunar swirls, while the cometary impact and dust transport model are not supported by our results. In addition, this study indicates that solar wind ions implantation is the major mechanism of space weathering instead of micrometeoroid impacts.

Currently, only variation in mass fraction of SMFe, abundance of plagioclase, and PS of soil grains were considered in Hapke's RTM to explain the spectral differences between on- and off-swirl surfaces. However, the anomalous photometric properties of on-swirl regions have also been shown to be related to the surface's physical properties such as

porosity and sub-resolution roughness (*Kreslavsky and Shkuratov,* 2003*; Kaydash et al.*, 2009), which were not taken into account in this study. These factors can be considered in future studies and incorporated into Hapke's RTM to further refine our understanding of the formation of lunar swirls.

Acknowledgements

We would like to thank Ying Sun for her comments and suggestions. The patience and assistance of Jia Du and Igor Ogashawara in the preparation of the figures are also greatly appreciated.

Table Captions

Table 1. Lunar swirls investigated in this study.

Tables

Table 4-1

Swirls	Locations	Geological Setting	Magnetic Anomaly Strength (nT)
Reiner Gamma	7.5^{o}N, 302.5^{o}E	Mare	22 - Strong
Ingenii	33.5^{o}S, 160^{o}E	Mare	20 - Strong
Marginis	16^{o}N, 88^{o}E	Mare	6 – Weak
Airy	18^{o}S, 3.25^{o}E	Highland	13 - Moderate
Firsov	10.5^{o}S, 16.5^{o}E	Highland	11 - Moderate

Figure Captions

Figure 4-1. (a) M^3 false color composite (R = 950 nm, G = 750 nm, B = 540 nm) for swirl Reiner Gamma. (b) Mass fraction of smaller size SMFe. (c) Mass fraction of larger size SMFe. (d) Comparison between modeled and measured image spectra for Reiner Gamma.

Figure 4-2. (a) M^3 false color composite for Airy swirl. Color assignments are the same as Figure 4-1. (b) Mass fraction of smaller size SMFe. (c) Mass fraction of larger size SMFe. (d) Comparison between modeled and measured image spectra for Airy.

Figure 4-3. (a) M^3 false color composite for Firsov swirl. Color assignments are the same as in Figure 4-1. (b) Mass fraction of smaller size SMFe. (c) Mass fraction of larger size SMFe. (d) Comparison between modeled and measured image spectra for Firsov.

Figure 4-4. (a) M^3 false color composite for Marginis swirl. Color assignments are the same as in Figure 4-1. (b) Mass fraction of smaller size SMFe. (c) Mass fraction of larger size SMFe. (d) Comparison between modeled and measured image spectra for Marginis. Black color in (b) and (c) is used to mask highland materials in Mare Marginis.

Figure 4-5. (a) M^3 false color mosaic image for mare Ingenii. Color assignments are the same as in Figure 4-1. (b-d) M^3 false color images for three locations investigated in this region. (e-g) Mass fraction of smaller size SMFe. (h-j) Mass fraction of larger size SMFe. (k-m) Comparison between modeled and measured image spectra for these three locations in Mare Ingenii.

Figure 4-6. (a) Changing PS and SMFe for fitting averaged on- and off- swirl spectra. (b) M^3 false color composite of Reiner Gamma (R = 950 nm, G = 750 nm, B = 540 nm), red and green rectangles represent locations where averaged on- and off-swirl spectra were selected.

Figure 4-7. (a) Derived PS of on- and off-swirl soils for the cometary impact model. (b) Derived mass fraction of SMFe in on- and off-swirl soils for the cometary impact model. (c) Comparison between modeled and measured image spectra.

Figure 4-8. (a) Changing abundance of plagioclase and PS for fitting averaged on- and off-swirl spectra. (b) M^3 false color composite of Reiner Gamma (R = 950 nm, G = 750 nm, B = 540 nm), red and green rectangles represent locations where averaged on- and off-swirl spectra were selected.

Figure 4-9. (a) Derived PS of on- and off-swirl soils for the dust transport model. (b) Derived abundance of plagioclase in on- and off-swirl soils for the dust transport model. (c) Comparison between modeled and measured image spectra.

Figures

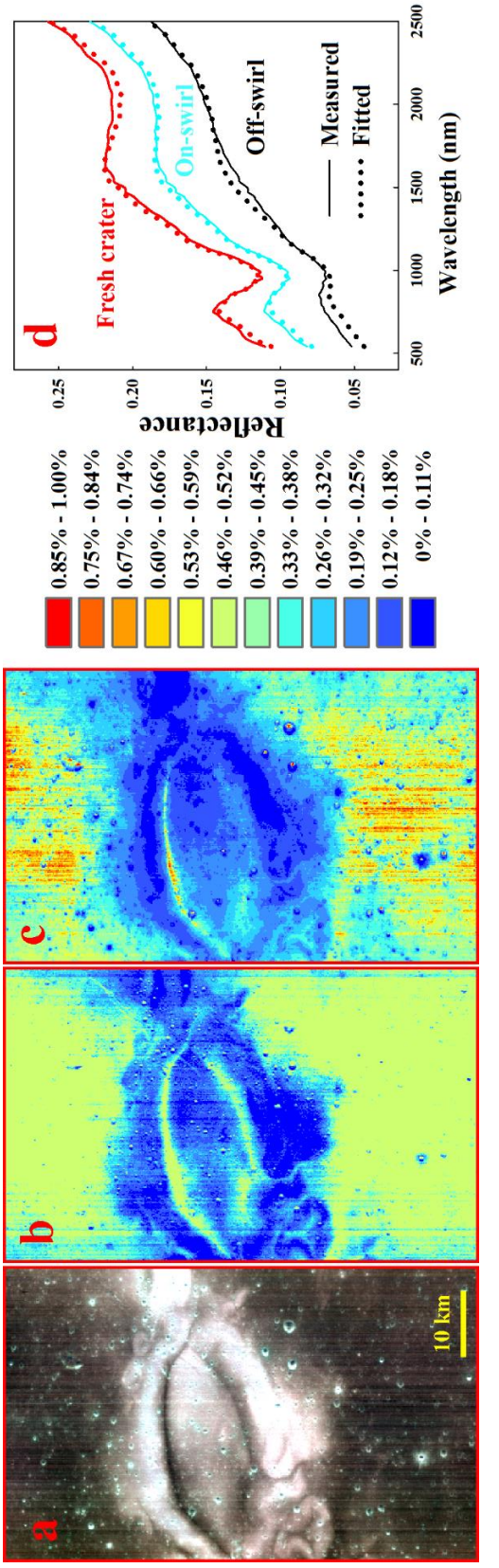

Figure 4-1

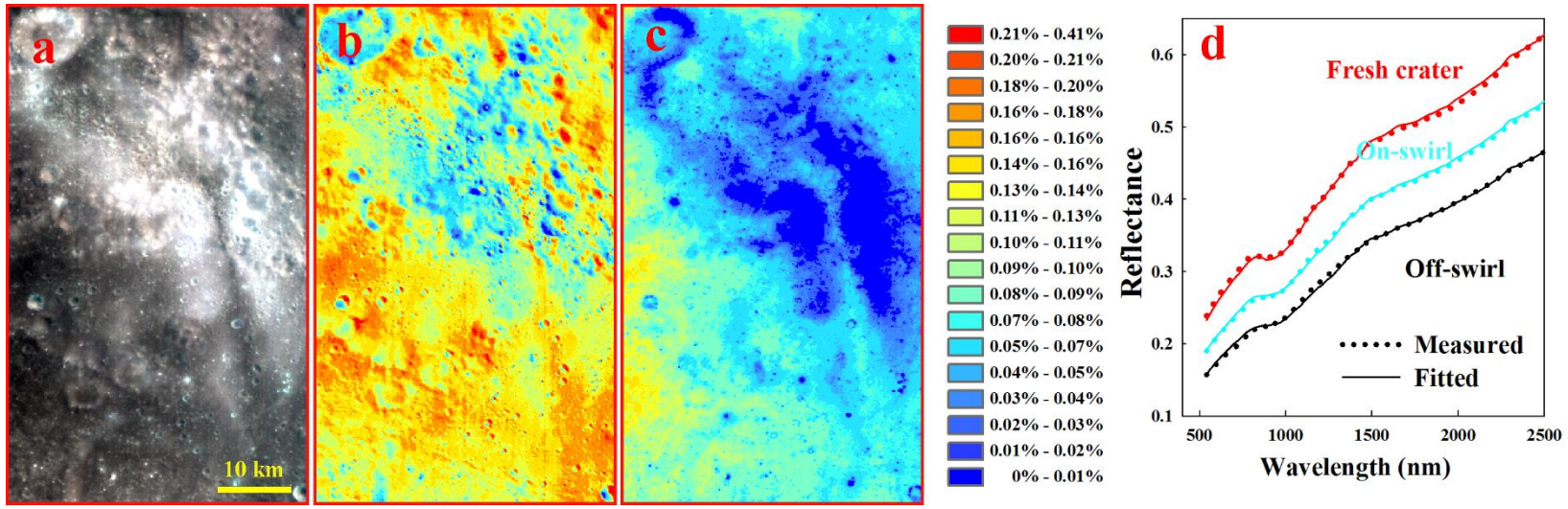
a
10 km
b
c
0.21% - 0.41%
0.20% - 0.21%
0.18% - 0.20%
0.16% - 0.18%
0.16% - 0.16%
0.14% - 0.16%
0.13% - 0.14%
0.11% - 0.13%
0.10% - 0.11%
0.09% - 0.10%
0.08% - 0.09%
0.07% - 0.08%
0.05% - 0.07%
0.04% - 0.05%
0.03% - 0.04%
0.02% - 0.03%
0.01% - 0.02%
0% - 0.01%
d
Fresh crater
On-swirl
Off-swirl
Measured
Fitted
Reflectance
Wavelength (nm)
0.1
0.2
0.3
0.4
0.5
0.6
500
1000
1500
2000
2500

Figure 4-2

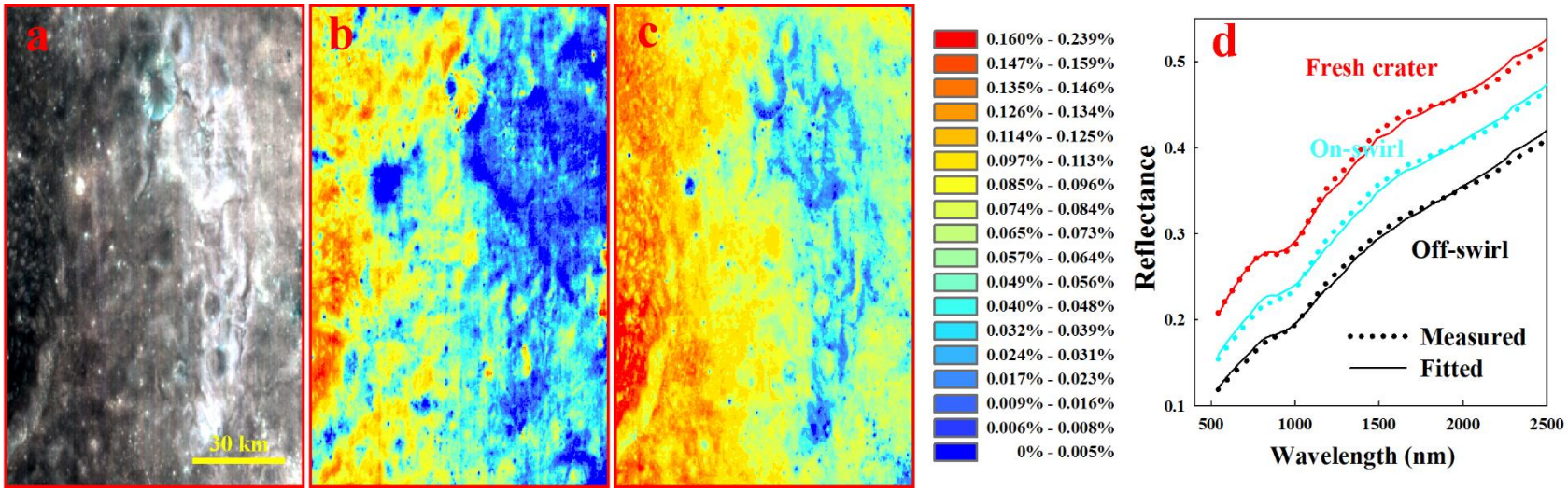
a
b
c
30 km
0.160% - 0.239%
0.147% - 0.159%
0.135% - 0.146%
0.126% - 0.134%
0.114% - 0.125%
0.097% - 0.113%
0.085% - 0.096%
0.074% - 0.084%
0.065% - 0.073%
0.057% - 0.064%
0.049% - 0.056%
0.040% - 0.048%
0.032% - 0.039%
0.024% - 0.031%
0.017% - 0.023%
0.009% - 0.016%
0.006% - 0.008%
0% - 0.005%
d
Fresh crater
On-swirl
Off-swirl
Measured
Fitted
Reflectance
Wavelength (nm)
0.1
0.2
0.3
0.4
0.5
500
1000
1500
2000
2500

Figure 4-3

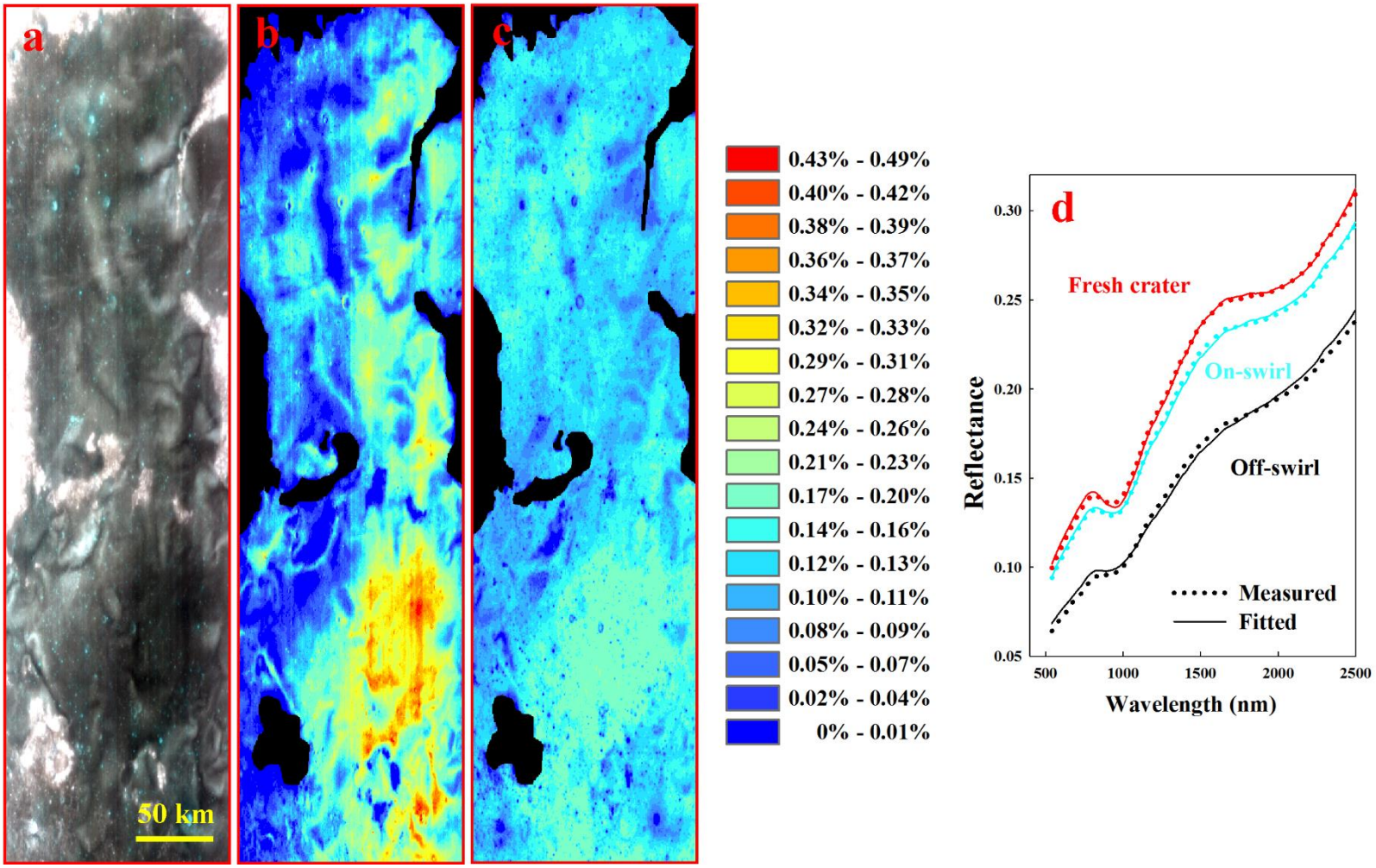
a
b
c
50 km
0.43% - 0.49%
0.40% - 0.42%
0.38% - 0.39%
0.36% - 0.37%
0.34% - 0.35%
0.32% - 0.33%
0.29% - 0.31%
0.27% - 0.28%
0.24% - 0.26%
0.21% - 0.23%
0.17% - 0.20%
0.14% - 0.16%
0.12% - 0.13%
0.10% - 0.11%
0.08% - 0.09%
0.05% - 0.07%
0.02% - 0.04%
0% - 0.01%
d
Fresh crater
On-swirl
Off-swirl
Measured
Fitted
Reflectance
Wavelength (nm)
0.30
0.25
0.20
0.15
0.10
0.05
500
1000
1500
2000
2500

Figure 4-4

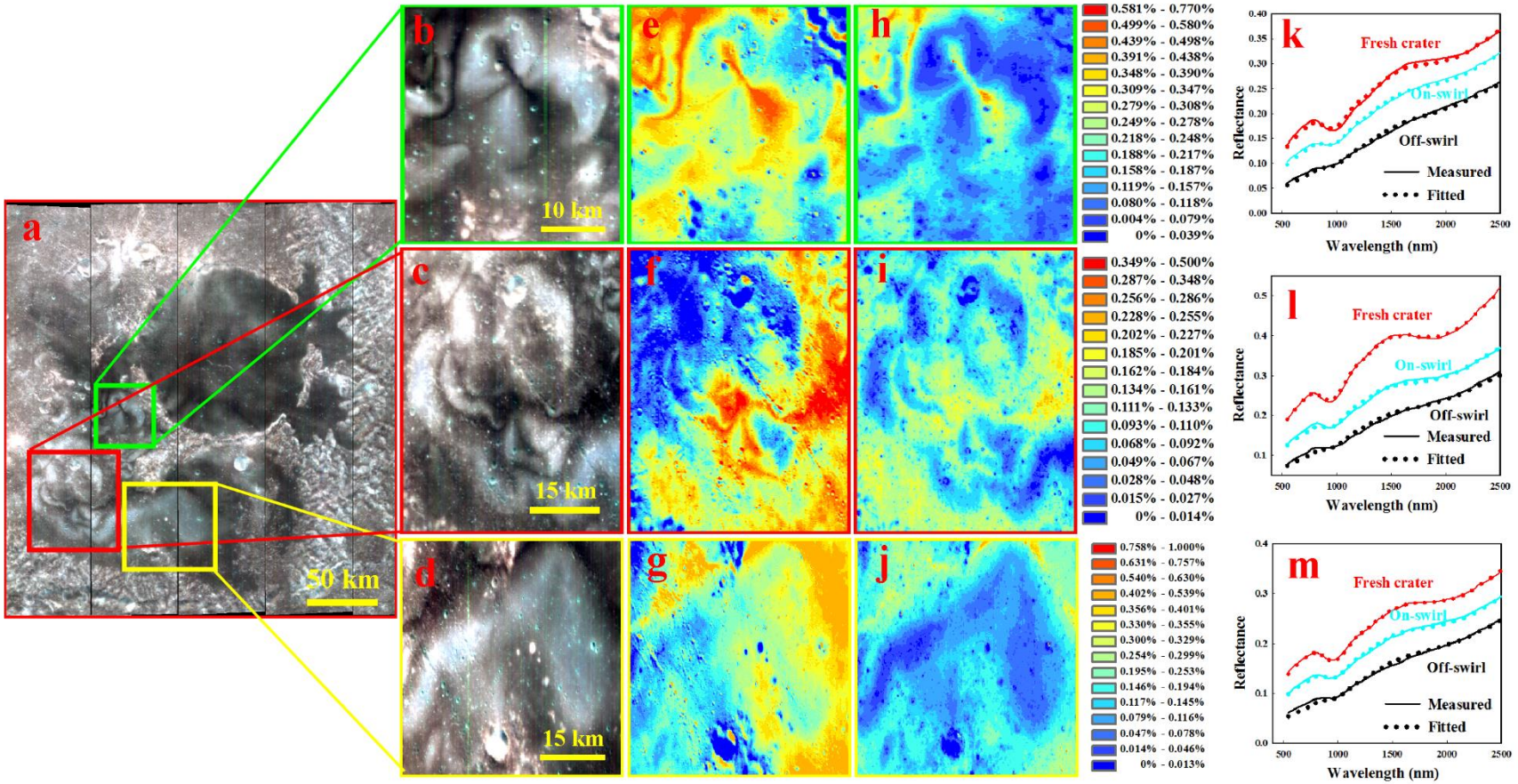
a
b
c
d
e
f
g
h
i
j
k
l
m
50 km
10 km
15 km
15 km
0.581% - 0.770%
0.499% - 0.580%
0.439% - 0.498%
0.391% - 0.438%
0.348% - 0.390%
0.309% - 0.347%
0.279% - 0.308%
0.249% - 0.278%
0.218% - 0.248%
0.188% - 0.217%
0.158% - 0.187%
0.119% - 0.157%
0.080% - 0.118%
0.004% - 0.079%
0% - 0.039%
0.349% - 0.500%
0.287% - 0.348%
0.256% - 0.286%
0.228% - 0.255%
0.202% - 0.227%
0.185% - 0.201%
0.162% - 0.184%
0.134% - 0.161%
0.111% - 0.133%
0.093% - 0.110%
0.068% - 0.092%
0.049% - 0.067%
0.028% - 0.048%
0.015% - 0.027%
0% - 0.014%
0.758% - 1.000%
0.631% - 0.757%
0.540% - 0.630%
0.402% - 0.539%
0.356% - 0.401%
0.330% - 0.355%
0.300% - 0.329%
0.254% - 0.299%
0.195% - 0.253%
0.146% - 0.194%
0.117% - 0.145%
0.079% - 0.116%
0.047% - 0.078%
0.014% - 0.046%
0% - 0.013%
Fresh crater
On-swirl
Off-swirl
Measured
Fitted
Reflectance
Wavelength (nm)

Figure 4-5

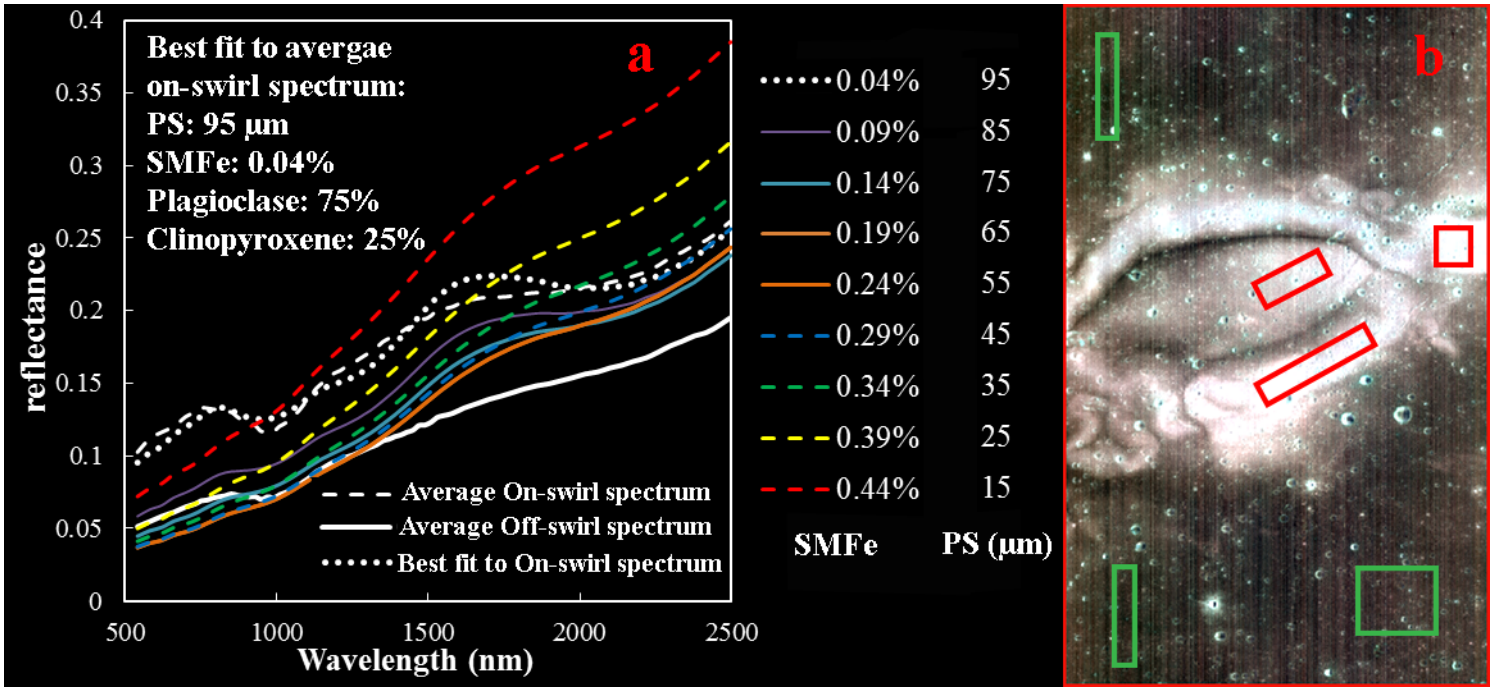
Best fit to avergae
on-swirl spectrum:
PS: 95 µm
SMFe: 0.04%
Plagioclase: 75%
Clinopyroxene: 25%
a
b
reflectance
Wavelength (nm)
0.4
0.35
0.3
0.25
0.2
0.15
0.1
0.05
0
500
1000
1500
2000
2500
Average On-swirl spectrum
Average Off-swirl spectrum
Best fit to On-swirl spectrum
0.04% 95
0.09% 85
0.14% 75
0.19% 65
0.24% 55
0.29% 45
0.34% 35
0.39% 25
0.44% 15
SMFe
PS (µm)

Figure 4-6

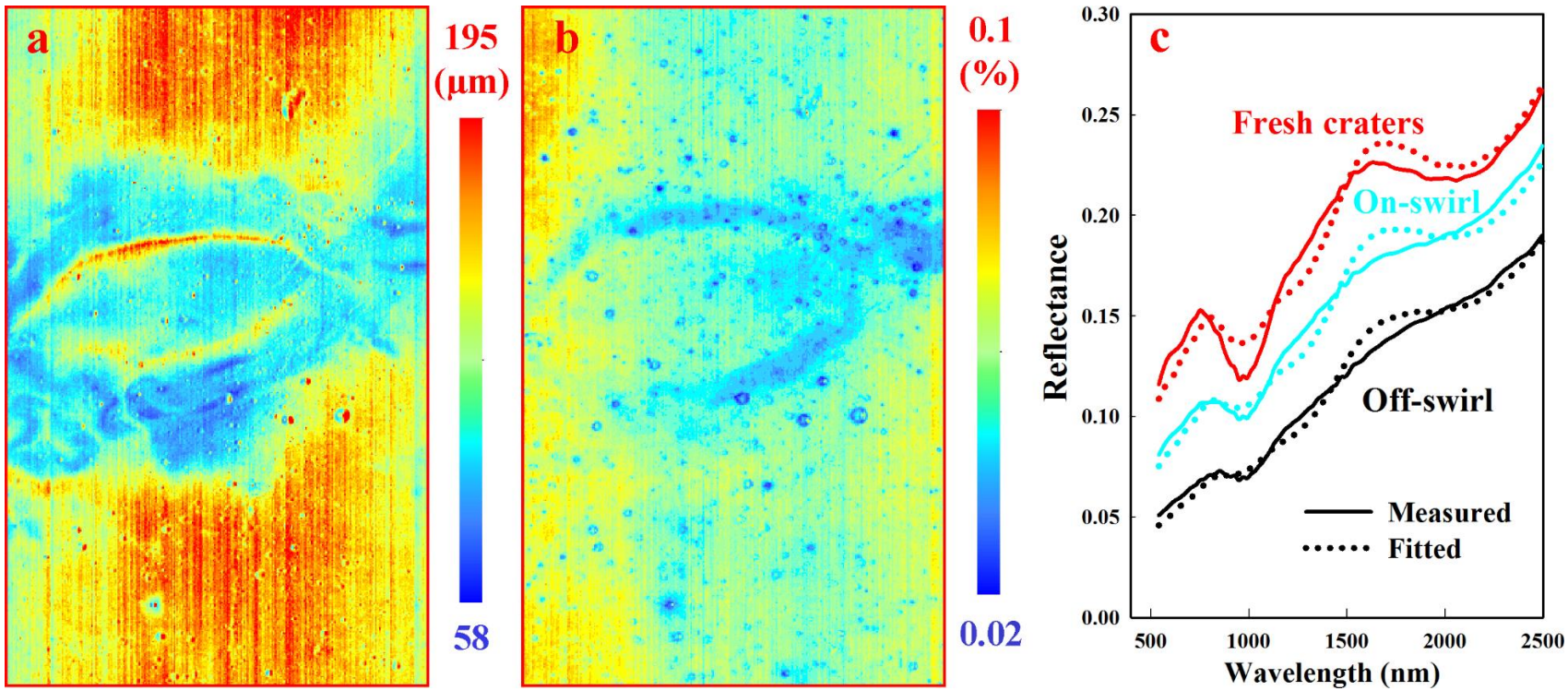
a
195
(μm)
58
b
0.1
(%)
0.02
c
Fresh craters
On-swirl
Off-swirl
Measured
Fitted
Reflectance
Wavelength (nm)
0.00
0.05
0.10
0.15
0.20
0.25
0.30
500
1000
1500
2000
2500

Figure 4-7

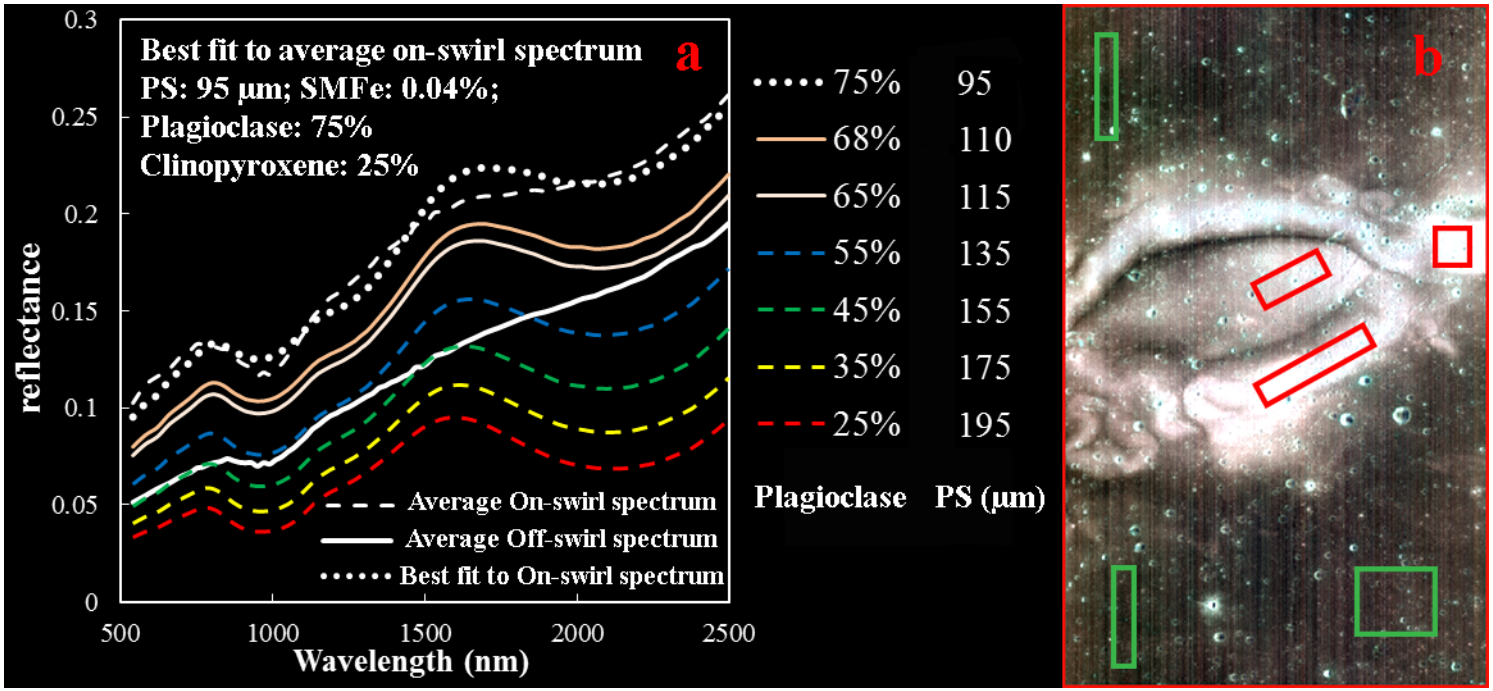
Best fit to average on-swirl spectrum
PS: 95 µm; SMFe: 0.04%;
Plagioclase: 75%
Clinopyroxene: 25%
a
b
reflectance
Wavelength (nm)
0.3
0.25
0.2
0.15
0.1
0.05
0
500
1000
1500
2000
2500
Average On-swirl spectrum
Average Off-swirl spectrum
Best fit to On-swirl spectrum
75% 95
68% 110
65% 115
55% 135
45% 155
35% 175
25% 195
Plagioclase PS (µm)

Figure 4-8

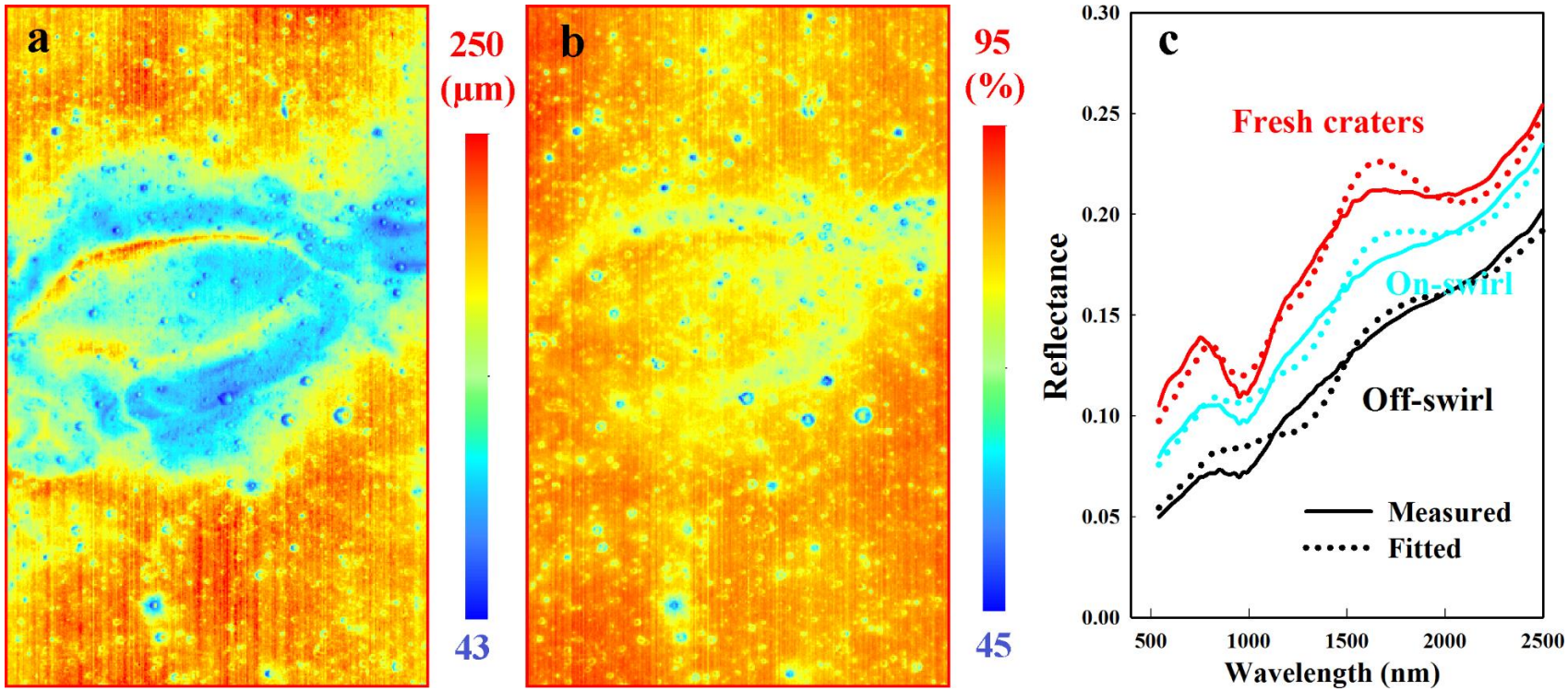
a
250
(μm)
43
b
95
(%)
45
c
Fresh craters
On-swirl
Off-swirl
Measured
Fitted
Reflectance
Wavelength (nm)
0.00
0.05
0.10
0.15
0.20
0.25
0.30
500
1000
1500
2000
2500

Figure 4-9

References

Bell, J. F., and B. R. Hawke (1981), The Reiner Gamma formation: Composition and origin as derived from remote sensing observations, *Proc. Lunar Planet. Sci. Conf.* 12, 679–694.

Bell, J. F., and B. R. Hawke (1987), Recent comet impacts on the moon: The evidence from remote sensing studies, *Publ. Astron. Soc. Pacific*. 99, 862–867.

Blewett, D. T., E. I. Coman, B. R. Hawke, J. J. Gillis-Davis, M. E. Purucker, and C. G. Hughes (2011), Lunar swirls: Examining crustal magnetic anomalies and space weathering trends, *J. Geophys. Res. - Planets* 116, E02002.

Cassidy, W., and B. Hapke (1975), Effects of darkening processes on surfaces of airless bodies, *Icarus* 25, 371-383.

Cahill, J. T. S., and P. G. Lucey (2007), Radiative transfer modeling of lunar highlands spectral classes and relationship to lunar samples, *J. Geophys. Res. - Planets* 112, E10007.

Cahill, J. T. S., P. G. Lucey, and M. A. Wieczorek (2009), Compositional variations of the lunar crust: Results from radiative transfer modeling of central peak spectra, *J. Geophys. Res. - Planets* 114, E09001.

Cahill, J. T. S., P. G. Lucey, K. R. Stockstill-Cahill, and B. R. Hawke (2010), Radiative transfer modeling of near-infrared reflectance of lunar highland and mare soils, *J. Geophys. Res. - Planets* 115, E12013.

Criswell, D. R. (1972), Lunar dust motion, *Proc. Lunar Planet. Sci. Conf.* 3, 2671–2680.

Clark, R. N. (2009), Detection of adsorbed water and hydroxyl on the Moon, *Science* 326, 562–568.

Chevrel, S. P. et al. (2006), Surface physical properties of the lunar regolith at Reiner Gamma: Characterization and distribution using Hapke model inversion, *Lunar Planet. Sci*. 37, 1173.

Denevi, B. W., P. G. Lucey, and S. B. Sherman (2008), Radiative transfer modeling of near-infrared spectra of lunar mare soils: Theory and measurement, *J. Geophys. Res.-Planets* 113, E02003.

Fechtig, H., E. Grün, and G. Morfill (1979), Micrometeoroids within ten Earth radii, *Planet. Space Sci*. 27, 511 – 531.

Fischer, E. M., and C. M., Pieters (1994), Remote determination of exposure degree and iron concentration of lunar soils using VIS-NIR spectroscopic methods, *Icarus* 111, 475-488.

Fuller, M., and S. Cisowski (1987), Lunar paleomagnetism, in Geomagnetism, edited by J. Jacobs, Academic Press, San Diego, CA, pp. 307– 456.

Futaana, Y., S. Barabash, M. Holmström, and A. Bhardwaj (2006), Low energy neutral atoms imaging of the Moon. *Planet. Space Sci.*, 54, 132–143.

Garrick-Bethell, I., J. W. Head, and C. M. Pieters (2011), Spectral properties, magnetic fields, and dust transport at lunar swirls, *Icarus* 212, 480–492.

Garrick-Bethell, I. et al. (2015), Nanowarm: a cubesat discovery mission to study space weathering, lunar magnetism, lunar water, and small-scale magnetospheres, *Lunar Planet. Sci. Conf.* 46, 3000.

Glotch et al. (2012), Observations of luanr swirls by the Diviner Lunar Radiometer Experiment. *Lunar Planet. Sci. Conf.* 43, 1951.

Gold, T., and S. Soter (1976), Cometary impact and the magnetization of the Moon, *Planet. Space Sci*. 24, 45–54.

Hapke, B. (1965), Effects of a simulated solar wind on the photometric properties of rocks and powders. *Ann. N. Y. Acad. Sci.* 123, 711-721.

Hapke, B. (1970), Inferences from the optical properties of the moon concerning the nature and evolution of the lunar surface, *Radio Sci.* 5, 293-299.

Hapke, B. (1973), Darkening of silicate rock powders by solar wind sputtering, *The moon* 7, 342-355.

Hapke, B., W. Cassidy, and E. Well (1975), Effects of vapor-phase deposition processes on the optical, chemical, and magnetic properties of the lunar regolith, *The moon* 13, 339-353.

Hapke, B. (1981), Bidirectional reflectance spectroscopy: 1. Theory, *J. Geophys. Res.-Solid Earth* 86, 3039-3054.

Hapke, B. (1993), Theory of Reflectance and Emittance Spectroscopy, 450 pp., Cambridge Univ. Press, Cambridge, U. K.

Hapke, B. (2001), Space weathering from Mercury to the asteroid belt, *J. Geophys. Res.-Planets* 106, 10039-10073.

Hapke, B. (2005), Theory of reflectance and emittance spectroscopy. Cambridge Univ. Press, New York.

Harnett, E. M., and R. M. Winglee (2002), 2.5D particle and MHD simulations of mini-magnetospheres at the Moon, *J. Geophys. Res.* 107, 1421.

Hemingway, D., and I. Garrick-Bethell (2012), Magnetic field direction and lunar swirl morphology: Insights from Airy and Reiner Gamma, *J. Geophys. Res.* 117, E100012.

Hemingway, D., and I. Garrick-Bethell (2014), Space weathering at lunar swirls and at high lunar lattitudes, *Lunar Planet.Sci. Conf.* 45, 1979.

Hiroi, T., M. Abe, K. Kitazato, S. Abe, B. E. Clark, S. Sasaki, M. Ishiguro, and O. S. Barnouin-Jha (2006), Developing space weathering on the asteroid 25143 Itokawa, *Nature* 443.

Hood, L. L., and G. Schubert (1980), Lunar magnetic anomalies and surface optical properties, *Science* 208, 49 – 51.

Hood, L. L., and C. R. Williams (1989), The lunar swirls: Distribution and possible origins, *Proc. Lunar Planet. Sci. Conf.* 19, 99 – 113.

Hood, L. L., and Z. Huang (1991), Formation of magnetic anomalies antipodal to lunar impact basins: Two dimensional model calculations,. *J. Geophys. Res*. - *Planets* 96, 9837–9846.

Hood, L. L., A. Zakharian, J. Halekas, D. L. Mitchell, R. P. Lin, M. H. Acuna, and A. B. Binder (2001), Initial mapping and interpretation of lunar crustal magnetic anomalies using Lunar Prospector magnetometer data, *J. Geophys. Res.* - *Planets* 106, 27,825–27,839.

Hood, L. L., and A. Artemieva (2008), Antipodal effects of lunar basin!forming impacts: Initial 3D simulations and comparisons with observations, *Icarus* 193, 485–502.

Kaydash, V., M. Kreslavsky, Y. Shkuratov, S. Gerasimenko, P. Pinet, J. L. Josset, S. Beauvivre, B. Foing, and the AMIE SMART-1 Team (2009), Photometric anomalies of the lunar surface studied with SMART-1 AMIE data, *Icarus* 202, 393–413.

Keller, L. P., and D. S. Mckay (1993), Discovery of vapor deposits in the Lunar Regolith, *Science* 261, 1305-1307.

Keller, L. P., and D. S. McKay (1997), The nature and origin of rims on lunar soil grains, *Geochim. Cosmochim. Acta* 61, 2331-2341.

Kramer, G. Y. et al. (2011a), Characterization of lunar swirls at Mare Ingenii: A model for space weathering at magnetic anomalies, *J. Geophys. Res. - Planet* 16. E04008.

Kramer, G. Y. et al. (2011b), M^3 spectral analysis of lunar swirls and the link between optical maturation and surface hydroxyl formation at magnetic anomalies, *J. Geophys. Res.- Planet* 116. E9.

Kreslavsky, M. A., and Y. G. Shkuratov (2003), Photometric anomalies of the lunar surface: Results from Clementine data, *J. Geophys. Res. - Planet* 108, 5015.

Li, S., and L. Li (2011), Radiative transfer modeling for quantifying lunar surface minerals, particle size, and submicroscopic metallic Fe, *J. Geophys. Res. - Planets* 116, E09001.

Lin, R. P., K. A. Anderson, and L. L. Hood (1988), Lunar surface magneticfield concentrations antipodal to young large impact basins, *Icarus* 74, 529–541.

Liu, D., L, Li and Y, Sun (2015), An improved Hapke's radiative transfer model for estimating mineral abundance of immature and mature lunar soils, *Icarus* 253, 40-50.

Lucey, P. G. (1998), Model near-infrared optical constants of olivine and pyroxene as a function of iron content, *J. Geophys. Res. - Planets* 103, 1703-1713.

Lucey, P. G. (2004), Mineral maps of the Moon, *Geophys. Res. Lett*. 31, L08701.

Lucey, P. G., and S. K. Noble (2008), Experimental test of a radiative transfer model of the optical effects of space weathering, *Icarus* 197, 348-353.

Lucey, P. G., D. A. Paige, B. T. Greenhagen, J. L. Bandfield and T. D. Glotch (2010), Composition of Diviner Charistiansen Feature position and visible albedo: Composition and space weathering implications, *Lunar Planet. Sci. Conf.* 41, 1600.

Lucey, P. G., and M. A. Riner (2011), The optical effects of small iron particles that darken but do not redden: Evidence of intense space weathering on Mercury, *Icarus* 212, 451-462.

Lucey, P. G., E. Song, B. T. Greenhagen, J. Gillis-Davis, I. Thomas, N. Bowles, L. F. Millan, K. L. Donaldson Hanna and D. A. Paige (2013), Global Diviner Charistiansen feature space weathering effects: hypotheses, experiment and mitigation, *Lunar Planet. Sci. Conf.* 44, 2890.

McCord, T. B., and J. B. Adams (1973), Progress in remote optical analysis of lunar surface composition, *The Moon* 7, 453-474.

Mustard, J. F., and C. M., Pieters (1987), Quantitative abundance estimates from bidirectional reflectance measurements, *J. Geophys. Res. - Solid Earth* 92, E617-E626.

Mustard, J. F., and C. M. Pieters (1989), Photometric phase functions of common geologic minerals and applications to quantitative analysis of mineral mixture reflectance spectra, *J. Geophys. Res. - Solid Earth* 94, 13619-13634.

Neish, C. D., D. T. Blewett, D. B. J. Bussey, S. J. Lawrence, M. Mechtley, and B. J. Thomson (2011), The surficial nature of lunar swirls as revealed by the Mini-RF instrument, *Icarus* 215, 186–196.

Noble, S. K., C. M. Pieters, and L. P. Keller (2007), An experimental approach to understanding the optical effects of space weathering, *Icarus* 192, 629-642.

Noble, S. K., C. M. Pieters, L. A. Taylor, R. V. Morris, C. C. Allen, D. S. McKay, and L. P. Keller (2001), The optical properties of the finest fraction of lunar soil: Implications for space weathering, *Meteorit. Planet. Sci.* 36, 31-42.

Pieters, C. M., E. M. Fischer, O. Rode, and A. Basu (1993), Optical effects of space weathering: The role of the finest fraction, *J. Geophys. Res. - Planets* 98, 20817-20824.

Pieters, C. M., L. A. Taylor, S. K. Noble, L. P. Keller, B. Hapke, R. V. Morris, C. C. Allen, D. S. McKay, and S. Wentworth (2000), Space weathering on airless bodies: Resolving a mystery with lunar samples, *Meteorit. Planet. Sci*. 35, 1101-1107.

Pieters, C. M., and I. Garrick-Bethell (2015), Hydration variations at lunar swirls, *Lunar Planet. Sci. Conf.* 46, 2120.

Pieters, C. M. et al. (2009), Character and spatial distribution of OH^{-}/H_2O on the surface of the Moon seen by M3 on Chandrayaan-1, *Science* 326, 568–572.

Pinet, P. C., V. V. Shevchenko, S. D. Chevrel, Y. Daydou, and C. Rosemberg (2000), Local and regional lunar regolith characteristics at Reiner Gamma formation: Optical and spectroscopic properties from Clementine and Earth-based data, *J. Geophys. Res. – Planets* 105, 9457-9476.

Richmond, N. C., L. L. Hood, J. S. Halekas, D. L. Mitchell, R. P. Lin, M. Acuna, and A. B. Binder (2003), Correlation of a strong lunar magnetic anomaly with a high-albedo region of the Descartes mountains, *Geophys. Res. Lett.* 30, 1395.

Richmond, N. C., L. L. Hood, D. L. Mitchell, R. P. Lin, M. H. Acuna, and A. B. Binder (2005), Correlations between magnetic anomalies and surface geology antipodal to lunar impact basins, *J. Geophys. Res*.110, E05011.

Schultz, P. H., and L. J. Srnka (1980), Cometary collisions on the Moon and Mercury, *Nature* 284, 22–26.

Shkuratov Y., L. Starukhina, H. Hoffmann, and G. Arnold (1999), A model of spectral albedo of particulate surfaces: implication to optical properties of the Moon, *Icarus* 137, 2, 235-246

Shkuratov, Y., V. Kaydash, S. Gerasimenko, N. Opanasenko, Y. Velikodsky, V. Korokhin, and C. Pieters (2010), Probable swirls detected as photometric anomalies in Oceanus Procellarum, *Icarus* 208, 20-30.

Starukhina, L. V., and Y. G. Shkuratov (2004), Swirls on the Moon and Mercury: Meteroid swarm encounters as a formation mechanism, *Icarus* 167, 136-147.

Sun, Y., and L. Li (2014), Global investigation of olivine bearing crater central peaks with M^3 images, *Lunar Planet. Sci. Conf.* 45, 1653.

Taylor, L. A., C. M. Pieters, L. P. Keller, R. V. Morris, and D. S. McKay (2001), Lunar mare soils: Space weathering and the major effects of surface-correlated nanophase Fe. *J. Geophys. Res. - Planets* 106, 27985-27999.

Taylor, L. A., C. M. Pieters, A. Patchen, D. S. Taylor, R. V. Morris, L. P. Keller, and D. S. Mckay (2010), Mineralogical and chemical characterization of lunar highland soils: Insights into the space weathering of soils on airless bodies, *J. Geophys. Res. - Planets* 115, E02002.

Vernazza, P., R. P. Binzel, A. Rossi, M. Fulchignoni, and M. Birlan (2009), Solar wind as the origin of rapid reddening of asteroid surfaces, *Nature* 458.

Wieser, M., S. Barabash, Y. Futaana, M. Holmström, A. Bhardwaj, R. Sridharan, M. B. Dhanya, A. Schaufelberger, P. Wurz, and K. Asamura (2010), First observation of a mini-magnetosphere above a lunar magnetic anomaly using energetic neutral atoms, *Geophys. Res. Lett.* 37, L05103.

Zook, H. A., and J. E. McCoy (1991), Large scale lunar horizon glow and a high altitude lunar dust exosphere, *Geophys. Res. Lett.* 18, 2117–2120.

CHAPTER 5

CONCLUSIONS AND FUTURE WORK

1. Conclusions

This work has demonstrated the strong effects of space weathering on the reflectance spectra of lunar soils. Space weathering greatly changes the PS of soil grains and results in the formation of SMFe. Both SMFe and PS have the strongest impact across the whole wavelength regions and they are the two most important factors that control the variance of reflectance spectra of lunar soils. The contribution of mineral abundance to the lunar soil reflectance is much less significant than that of PS and SMFe. Reflectance spectra of lunar soils are sensitive to palgioclase abundance across the whole wavelength regions because of the significant effecct of plagioclase in regulating the magnitude of reflectance. 1000 nm and 2000 nm absorptions of lunar soil reflectance spectra are mainly dominated by pyroxene abundance, and spectral regions between 1200 nm and 1400 rather than assumed 1050 nm are more sensitive to the variation of olivine abundance. When Hapke's RTM is applied to estimate mineral abundance on the lunar surface, the estimation accuracy could be potentially improved by choosing specific spectral regions where minerals contribute more to the variation of reflectance spectra, such as 1000 nm and 2000 nm for pyroxene and 1100 nm to 1400 nm for olivine.

In addition, I demonstrated that the improved Hapke's RTM with the incorporation of larger size SMFe effect in the modeling process has a better description of space weathering effects. The measured LSCC spectra of lunar soil samples can be accurately fitted by this improved Hapke's RTM and the average mass fraction of smaller and larger size SMFe in lunar soils was estimated to be 0.30 and 0.31 respectively. This improved Hapke's RTM enables more accurate prediction on abundance of agglutinitic glass, pyroxenen, and plagioclase for both immature and mature lunar soils, though there is poor

agreement between measured and estimated mineral abundance for ilemnite, olivine and volcanic glass.

In this work, I have shown that the spectral difference between on- and off-swirl surfaces can be fully explained by changing the mass fraction of both smaller and larger size SMFe in lunar soils rather than the variation in PS of soil grains and abundance of plagioclase. Off-swirl surfaces are indeed enriched smaller and larger size SMFe than on-swirl surfaces because of enhanced solar wind flux deflected from on-swirl surfaces. The solar deflection model is a valid hypothesis for the formation of lunar swirls, while the cometary impact model and the dust transport model are not prefered. These results strongly support the solar wind implantation rather than micrometeorite bombardment as the dominant mechanism of space weathering process.

2. Future Directions

There are several questions that need to be addressed in the future. First, although the improved Hapke's RTM presented in Chapter 3 can be used to describe the spectral effects of space weathering and improve the estimation of mineral abundances for agglutinitic glass, plagioclase, and pyroxene, there is a large discrepancy between modeled and measured abundances for olivine, volcanic glass and ilmenite. This can be attributed to the interference of chemical composition (e.g., Mg and An number) of lunar soils in the modeling process. The refractive index (*n* and *k*) of minerals strongly depend on their chemical composition (*Lucey*, 1998; *Wilcox et al.*, 2006; *Denevi et al*., 2007). Variation of the refractive index leads to changes in the magnitude, absorption position and depth of reflectance spectra. Future work should focus on accommodating the spectral effect of the chemical composition of each mineral in order to further improve Hapke's RTM.

Second, some physical properties of lunar soils such as porosity and roughness were not taken into account in the improved Hapke's RTM, which would interfere with spectral estimation of mineral abundance of lunar soils. In addition, the observed photometric anomalies of lunar swirls could result from such variation of physical properties of lunar soils (*Kreslavsky and Shkuratov*, 2003; *Kaydash et al*., 2009; *Shkuratove et al*., 2010). Future study requires the physical properties of lunar soils to be accommodated in Hapke's RTM.

In this PhD work, all the minerals of lunar soils were assumed to possess equal amounts of SMFe when the improved Hapke's RTM was used to predict mineral abundance of lunar soils. However, this might not be consistent with what occurs on the lunar surface. *Yamada et al*. (1999) and *Sasaki et al*. (2002) applied Laser-irradation on olivine and pyroxene samples to simulate the effects of space weathering and results showed that olivine was weathered more rapidly than pyroxene. This suggests the generation rate of SMFe in different minerals might vary. More SMFe could be generated in olivine than pyroxene under the same strength of laser irradiation, which results in a rapid loss of spectral contrast. Each mineral might show different resistance to space weathering. The enhanced production of SMFe in olivine than pyroxene is likely due to faster diffusion of iron in olivine (*Moroz et al*., 2014). On the other hand, the production of SMFe as a result of space weathering is also limited by the availability of the initial FeO content of the mineral (*Moroz et al*., 2014). Therefore, each mineral of lunar soils should be assigned a different mass fraction of SMFe in the improved Hapke's RTM.

Finally, as aforementioned, implanted H^+ might interact with Fe^{2+} producing SMFe with release of OH^-/H_2O when lunar soils are exposed to space environment. The

correlation between enhanced the mass fraction of SMFe and observed OH^-/H_2O signatures in off-swirl regions supported this reduction process. This gives rise to the possibility of using high mass fraction of SMFe to locate lunar surface areas with OH^-/H_2O. It is worth to obtain the global distribution of SMFe on the lunar surface, and test whether there is good correlation between the locations with high mass fractions of SMFe and surface areas with detected OH^-/H_2O. If this correlation is confirmed, the distribution of the mass fraction of SMFe on the lunar surface can serve as a tool for locating the target area with higher possibility of the OH^-/H_2O presence.

References

Denevi, B. W., P. G. Lucey, E. J. Hochberg, and D. Steutel (2007), Near-infrared optical constants of pyroxene as a function of iron and calcium content, *J. Geophys. Res. - Planets* 112, E05009.

Kaydash, V., M. Kreslavsky, Y. Shkuratov, S. Gerasimenko, P. Pinet, J. L. Josset, S. Beauvivre, B. Foing, and the AMIE SMART-1 Team (2009), Photometric anomalies of the lunar surface studied with SMART-1 AMIE data, *Icarus* 202, 393–413.

Kreslavsky, M. A., and Y. G. Shkuratov (2003), Photometric anomalies of the lunar surface: Results from Clementine data, *J. Geophys. Res. - Planets* 108, 5015.

Lucey, P. G., D. T. Blewett, and B. R. Hawke (1998), Mapping the FeO and TiO_2 content of the lunar surface with multispectral imagery, *J. Geophys. Res. - Planets* 103, 3679-3699.

Moroz, L. V., et al. (2014), Space weathering of silicate regoliths with various FeO contents: New insights from laser irradiation experiments and theoretical spectral simulations, *Icarus* 235, 187-206.

Sasaki, S., T. Hiroi, K. Nakamura, Y. Hamabe, E. Kurahashi, and M. Yamada (2002), Simulation of space weathering by nanosecond pulse laser heating: Dependence on mineral composition, weathering trend of asteroids and discovery of nanophase iron particles, *Adv. Space Res.* 29, 783-788.

Shkuratov, Y., V. Kaydash, S. Gerasimenko, N. Opanasenko, Y. Velikodsky, V. Korokhin, and C. Pieters (2010), Probable swirls detected as photometric anomalies in Oceanus Procellarum, *Icarus* 208, 20-30.

Wilcox, B. B., P. G. Lucey, and B. R. Hawke (2006), Radiative transfer modeling of compositions of lunar pyroclastic deposits, *J. Geophys. Res. - Planets* 111, E9.

Yamada, M., S. Sasaki, H. Nagahara, A. Fujiware, S. Hasegawa, H. Yano, T. Hiroi, H. Ohashi, and H. Otake (1999), simulation of space weathering of planet-forming materials: Nanophase pulse laser irradiation and protion implantation on olivine and pyroxene samples, *Earth Planets Sp.* 51, 1255-1265.

CURRICULUM VITAE

Dawei Liu

Education

Ph. D. Applied Earth Sciences, IUPUI, Aug. 2015.
B. Sc. Applied Geophysics, Jilin University, China, Jul. 2009.

Honors

- Arthur Mirsky Geology Graduate Scholarship, IUPUI, 2015.
- Earth Science Scholarship, IUPUI, 2014.

Professional Experience

Department of Earth Sciences, IUPUI, Graduate Research Assistant, 2010 – date

- Improved Hapke's radiative transfer model to estimate mineral abundance for both immature and mature lunar soils.
- Explored the formation of lunar swirls and investigated the relative importance of solar wind ions implantation versus micrometeorite bombardment in space weathering process.

Publications

- Liu, D., Li, L., Sun, Y., (2015). An improved radiative transfer model for estimating mineral abundance of immature and mature lunar soils. ***Icarus***, 253, 40-50, DOI:10.1016/j.icarus.2015.02.013.
- Liu, D., Li, L., Zhang, Y. Z., (2015). The formation of lunar swirls: Results from Hapke's radiative transfer modeling. ***Journal of Geophysical Research-Planet***, (to be submitted).
- Liu, D., Li, L., (2015). Sensitivity analysis for Hapke'sradiative transfer model and its implication in estimation of mass fraction of submicroscopic iron in lunar soils. ***Icarus***, (to be submitted).

Abstract

- Liu, D., Li, L., (2015). An empirical approach to estimating mass fraction of submicroscopic iron in lunar soils. ***46th Lunar and Planetary Science Conference***, #2560, Houston, USA.

- Liu, D., Li, Li., (2014). The formation of lunar swirls: results from Hapke's radiative transfer modeling. ***45th Lunar and Planetary Science Conference***, # 1654, Houston, USA.

- Liu, D., Li, L., Zhang, Y. Z., (2013). Sensitivity analysis for Hapke's radiative transfer model. ***44th Lunar and Planetary Science Conference***, #1290, Houston，USA.

- Liu, D., Li, L., (2012). An improved radiative transfer model for estimating mineral abundance of immature and mature lunar soils. ***43rd Lunar and Planetary Science Conference***, #2011, Houston，USA.